Sampling Digital Coherent Receiver for Demultiplexing and Processing of OTDM Signals Employing High-Order Modulation

Francesco Patarnello

Danmarks Tekniske Universitet - Fotonik

Università degli Studi di Padova - Dipartimento di Ingegneria dell'Informazione

A thesis submitted for the double degree of:

Master of Science (MSc) in Telecommunication

Laurea Specialistica in Ingegneria Elettronica

2010 August

Supervised by:

C. Peucheret, L. Oxenløwe, D. Zibar, and M.E. Valcher

Abstract

In this thesis, we present a study of optical communication systems that make use of multilevel modulations and exploits coherent detection with digital signal processing (DSP) and optical time division multiplexing (OTDM). The Matlab® modeling of an optical communication system if shown and the different elements of a DSP unit are analyzed. In particular we studied the Chromatic Dispersion (CD) compensation with Time Domain Equalizer (TDE), the Polarization Mode Dispersion (PMD) and polarization rotation compensation with adaptive equalizer, the digital phase estimation with Feed Forward (FF) algorithms and the frequency offset compensation. Next, we present the OTD demultiplexing for optical systems that utilize coherent receivers. A set of numerical simulation has been done for the study of the performance of the model implemented. At last we show the results obtained during a laboratory experiment. A back-to-back transmission of a 4-Channels OTDM QPSK system at 160 Gb/s with coherent detection and digital signal processing has been successfully performed and the results are presented and commented.

Ai miei genitori..

Acknowledgements

First of all, I would like to thank my friend Luca. He shared with me these ten months of work and he motivated me during the difficult moments encountered. He always backed me up and I am sure that this thesis would have been different without him.

I want also to thank all my supervisors and the professors that gave me great support. Thanks to Christophe that dedicated a lot of his time to answer my many question, being always very nice and friendly and showing an immense interest in what I was doing. Thanks also to Leif, Michael and Darko for all the help and the support during the many hours in the laboratory.

Then, I am also very grateful to all my house mates that stood me all day long. Thanks to Matteo for always being available to help me when I needed it. Thanks to Francesco for the uncountable times you cooked for all of us leaving the frying pan impossible to clean. And thanks to Davide for providing me with your computer, indispensable for terminating all the Matlab® simulations we needed to run.

Thanks also to Matteo and Andrea, my great and old friends lost somewhere in Italy and Scotland.

Infine un gigantesco grazie ai miei genitori che mi hanno sempre voluto bene e mi hanno appoggiato durante questa mia scelta di vivere lontano da casa.

Contents

List of Figures

List of Tables

1

Introduction

The download of data from the Internet increases constantly and fast. Every year the Internet traffic intensify by more than 50% and this pushes toward faster and faster communication connections. This trend is particularly affecting optical communication systems, that represent the skeleton of moder telecommunication networks.

Unlike traditional telecommunication systems, commercial optical systems have always been limited to intensity modulation with direct detection (IM-DD). However, nowadays the request for higher capacity connections is moving the interest toward new techniques to transmit optical signals.

The two major directions taken to support this evolution are the employment of *advanced optical modulations* and the use of *coherent receivers*. Particularly, the latter has been made possible by the advent of fast digital signal processing (DSP) circuits, that allow for decreasing the complexity and increasing the feasibility of traditional coherent receivers. A third technique employed to increase the capacity of optical communication systems is the use of Optical Time Division Multiplexing (OTDM) that allows for the multiplexing many optical channels in the time domain using Return-to-Zero (RZ) pulses.

In this thesis we are going to investigate on the use of high order modulation formats with OTDM in optical communication systems that employ coherent receivers with DSP unit. This study is part of a bigger project, in collaboration with my fried and colleague Luca Ferrari. The work consisted in the development and study of a numerical model (implemented in Matlab®) for the simulation of such an optical communication systems. After a few months working together we then took to different directions

and I delved into the detail of the modeling and analysis of a coherent receiver with DSP. The work done is described and collected in this thesis. After a first theoretical background given in Chapter 2, we describe the different elements present in an optical communication system with high order modulations in Chapter 3. Then, an analysis of the implementation of the numerical model is presented in Chapter 4. The theory and the modeling of the coherent receiver with DSP are described separately in Chapter 5. The last section of the thesis collect both the numerical results obtained through the model we developed (Chapter 6) and the practical experiment carried out in the laboratory (Chapter 7).

1.1 State of the Art and Future Goals

Even if commercial systems utilize almost only intensity modulation with direct detection, the research on the employment of high order modulation formats in optical communication systems started already years ago in combination with simple direct detection receivers. Many multilevel modulation transmitters and receivers have been developed for the employment with DD. There are several examples of multilevel (differential) phase and amplitude modulations like 8-DPSK (Differential Phase Shift Keying) or 16-DAPSK (Differential Amplitude Phase Shift Keying) systems with DD [5].

Direct Detection schemes have been preferred for long time to coherent receivers even if the latter allow for the use of much more complex modulation formats and an increase in the receiver sensitivity by up to 20 dB [1]. As a matter of fact, the difficulties in realizing OPLL for recovering the carrier phase, made a practical realization of an optical coherent receiver not feasible. Nevertheless, the advent of high-speed DSP circuits opened the door to a new way of receiving optical signals [6][7][8][9]. With the use of DSP both the employment of new modulation formats and of algorithms for the correction of propagation impairments have been carried out. Among the former great interest has been aroused by Quadrature Amplitude Modulation (QAM) [10][11][12][13]. The latter have been employed mainly to compensate in the electrical domain for chromatic dispersion and polarization mode dispersion impairments [14][8][15][9]. A new step for further improvement in optical communication transmission that attracted many research groups, is the combination of optical time division multiplexing (OTDM) with coherent detection. This is very hot a topic and there are several examples like

[16], [17], and [18] that showed how this technique is promising. In particular, [16] managed to correctly demodulate a 16-QAM signal up to 5.1 Tbit/s.

We believe that the combination of OTDM with the coherent detection of high order modulated signal might be the way to further increase these limits and obtain new records of data transmission on optical communication systems.

2

Theoretical Background

In order to fully understand this thesis it is important to have a good understanding of the basis of optical communication theory and some advanced theory about high order modulation formats. In this first chapter we are going to present the basic concepts that will accompany us for the rest of the study. A more detailed analysis about the different components of an optical communication systems that employs high order modulations and optical time division multiplexing is give in Chapter 3.

2.1 High Order Modulation Formats

The ways of carrying information through an optical signal in a fiber are various. The easiest thing that can pop up in our mind is to modulate the intensity of the optical field and to transmit a "0" with a zero intensity signal and a "1" with a high intensity signal. Indeed, this modulation format, also called On-Off keying (OOK), is the most used in real optical systems and it is surely the easiest to realize. On the other hand, other components of the optical field can be modulated. The use of phase modulation formats is one of the first attempts to move away from OOK. In the case of Phase Shift Keying (PSK), the information is coded on the phase ϕ of the optical signal. If in normal PSK formats coherent detection is needed in order to retrieve the full information of the complex electric field, DPSK had particular success because it allows for the use of a simple Direct Detection. With respect to OOK it showed a high robustness against nonlinear effects without increasing the complexity of the system.

Lately, there have been some examples of modulation formats that exploit also the polarization state $\widehat{\boldsymbol{x}}$ of the field (e.g. Polarization Multiplexing - PolMux). However, despite the increase in the data capacity, systems that exploits both polarizations suffer of Polarization Mode Dispersion (PMD) and polarization rotation. These phenomena, as explained in Chapter 2, impair the transmitted signal and require high complexity receivers (most of the times with coherent detection).

Another way to increase the degrees of freedom available to the designer of an optical communication system is to use multilevel signaling instead of binary modulation. Indeed it is possible to 'pack' many bits in one symbol by using modulations with more than two levels and hence increase the bit rate (with M levels it changes by a factor of $\log_2 M$) without changing the symbol rate. Furthermore, the different kinds of modulations can be used together. The study and development of high order modulation formats, the use of which can be found originally in radio communication, started in the early nineties. However, the necessity of coherent receivers and high speed electronics stopped this investigation. Furthermore, the advent of EDFAs made possible great improvements in optical communication systems performance even without the use of high order modulation formats.

Nowadays, the availability of high-speed electronics made the use of Digital Signal Processing (DPS) feasible at high bit rates and allows for the use of coherent receivers in optical communication systems. This increased the interest in high order modulation formats also in optical communication.

The reasons that push toward multilevel modulation formats are numerous. First, increasing the number of bits encoded on one symbol, it is possible to increase the transmission bit rate maintaining the spectral width almost unchanged (i.e. the spectral efficiency increases) as shown in Figure 2.1. This yields to better chromatic dispersion tolerances.

Second, a better spectral efficiency allows us to pack more signal channels in a single optical fiber by wave division multiplexing.

Third, the equipment used to generate and detect the signals works at the symbol rate and this allows us to increase the bit rate while using a generation and detection frequency lower (according to the number of level used).

In this thesis we will concentrate only on four modulation formats: OOK, DBPSK (or DPSK), DQPSK and Square 16-QAM. Moreover, the system exploits both optical

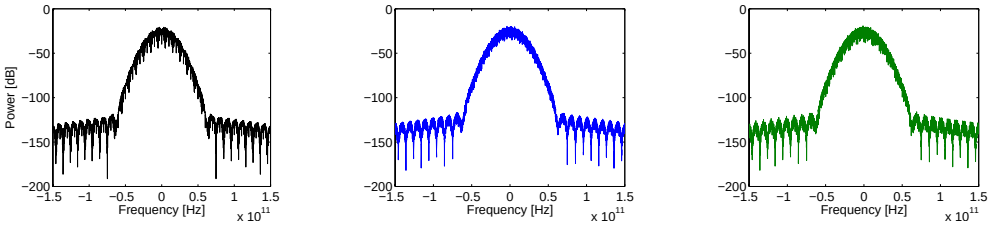

(a) (b) (c)

Figure 2.1: Spectra of (a) 10 GBt/s RZ-DPSK, (b) 10 GBt/s RZ-DQPSK, and (c) 10 GBt/s RZ-16QAM.

polarizations in a PolMux configuration.

2.2 Optical Time Division Multiplexing

There are different ways to increase the capacity of an optical communication system. A first solution consists in using different wavelength to transmit different signal at the same time (Wavelength DIvision Multiplexing - WDM). This technique is wide spread and is an effective way to dramatically increase the amount of data transmitted through one fiber.

Another solution consists in packing many return-to-zero (RZ) signals in one single symbol slot. This technique, called Time Division Multiplexing (TDM) is wide spread in common telecommunication system. In traditional TDM the signals are multiplexed in the electrical domain (ETDM). However, due to the speed limitation of the electronic components, ETDM does not allow to increase a the bit rate above 10 Gb/s. A solution to this is offered by the optical TDM (OTDM), in which the different channels are multiplexed together in the optical domain. With this technique the bit rate of a single carrier can be increased to values above 1 Tb/s [1].

2.3 Noise and Optical Signal to Noise Ration

The noise can be defined as an unwanted perturbation of the wanted signal. The sources of noise that can affect an optical communication system are many (e.g. shot noise, thermal noise, ASE noise, etc ...) and it is important to know how much the signal is affected by noise. An important parameter that describes the relation between

the wanted signal and the noise is the signal-to-noise ratio (SNR). The SNR is defined as the energy per symbol per polarization over the single-sided spectral density per polarization N_0:

$$\mathrm{SNR} = \frac{E_s}{p \cdot N_0}, \tag{2.1}$$

where p is the number of polarizations on which the noise is present. Another important noise parameter in optical communication is the optical signal-to-noise ration (OSNR). It represents the ration between the average optical power and the noise power over a certain reference bandwidth B_{ref} (that in our project is 12.5 GHz as generally found in literature [19]). In the case of a white Gaussian noise, as the ASE noise, the single-sided spectral density N_0 is constant over the reference bandwidth and thus the OSNR can be written as:

$$\mathrm{OSNR} = \frac{\langle P(t) \rangle}{p \cdot N_0 \cdot B_{ref}}. \tag{2.2}$$

As we will see in section 4.6, it is important to relate SNR and OSNR in order to be able to confront the results of our model with the literature (see section 4.8).

2.4 System Performance and BER analysis

As discussed in the previous section real systems are affected by noise. This and other impairments result in the possibility that the received signal is not decoded correctly and that errors arise in the decoded data. The performance of a system are therefore measured according to the number of errors in a sequence of bit. This analysis, also called Bit Error Rate (BER) measurement, provide information on the correctness of the received signal. It is common to call a signal with a BER of 10^{-9} *error-free*. Thus, if the decoded data is not further processed, a BER of 10^{-9} is generally required. However, error correction codes are often used in order to allow for the possibility of correcting errors in the received data [20]. Of course this has a threshold of number of errors per data bits that can be corrected and this is generally around one error every $10^3 \div 10^4$ bits. Hence, if we consider the possibility of using error correcting codes the BER required to obtain an error free sequence is around $10^{-3} \div 10^{-4}$.

In our project we will often refer to the BER of the received signal to have an idea about the performance of the system and compare results obtained with different specifications.

2.5 Optical Signal Representation

From the Maxwell's equations we can describe the propagation of an electromagnetic wave in an isotropic medium (an optical fiber can be considered an isotropic medium for our purposes) as:

$$\mathbf{E}(\mathbf{r},t) = \mathrm{Re}\left\{\mathbf{E}_0(\mathbf{r},t)e^{j(\omega_0 t - \mathbf{k}\cdot\mathbf{r})}\right\}, \tag{2.3}$$

where $\mathbf{E}_0$ is a complex vector and $\mathbf{r}$ and $\mathbf{k}$ are vectors in the orthonormal basis ($\mathbf{x}$,$\mathbf{y}$,$\mathbf{z}$). $\mathbf{E}_0$ represents the slowly varying time and location dependent complex envelope of the monochromatic electrical field. If we now suppose that the direction of propagation is $\mathbf{z}$ we can rewrite (2.3) as:

$$\mathbf{E}(z,t) = \mathrm{Re}\left\{\mathbf{E}_0(z,t)e^{j(\omega_0 t - \beta_0\cdot z)}\right\}, \tag{2.4}$$

where β_0 is called *propagation constant*. Due to the transverse nature of the wave, the complex vector $\mathbf{E}_0$ is on the plane ($\mathbf{x}$,$\mathbf{y}$) and it can be decomposed as:

$$\mathbf{E}_0(z,t) = \kappa[u_x(z,t)\cdot\mathbf{x} + u_y(z,t)\cdot\mathbf{y}] \tag{2.5}$$

where u_x and u_y are the complex components on the $\mathbf{x}$ and $\mathbf{y}$ directions, and κ is an arbitrary normalization constant.

For a monochromatic propagating wave, the relation between the opical power and the magnitude of $\mathbf{E}_0$ is:

$$P = \frac{c\epsilon_0 n}{2}A|\mathbf{E}_0|^2, \tag{2.6}$$

where c is the vacuum speed of light, n is the medium refractive index, ϵ_0 is the dielectric constant, and A is the area over which the electromagnetic wave irradiates. Thus, through (2.5) and (2.6) we can set the arbitrary normalization parameter κ as:

$$\kappa = \left(\frac{2}{\epsilon_0 cnA}\right)^{1/2}, \tag{2.7}$$

in order to be able to write the optical power as:

$$P(z,t) = |u_x(z,t)|^2 + |u_y(z,t)|^2. \tag{2.8}$$

The two complex components along $\mathbf{x}$ and $\mathbf{y}$ in (2.5) can be described in terms of their magnitude $A_{x,y}$ and phase $\phi_{x,y}$:

$$\mathbf{E}_0(z,t) = \kappa[A_x(z,t)e^{-j\phi_x(z,t)}\cdot\mathbf{x} + A_y(z,t)e^{-j\phi_y(z,t)}\cdot\mathbf{y}]. \tag{2.9}$$

From this we can collect the common phase $\phi(z,t) = \frac{\phi_x(z,t)+\phi_y(z,t)}{2}$ and the differential phase $\delta = \phi_x(z,t) - \phi_y(z,t)$. Hence, the complex vector $\mathbf{E}_0(z,t)$ can be rewritten as:

$$\mathbf{E}_0(z,t) = \kappa\, e^{-j\phi(z,t)}[A_x(z,t)e^{-j\delta(z,t)/2}\cdot\mathbf{x} + A_y(z,t)e^{j\delta(z,t)/2}\cdot\mathbf{y}]. \tag{2.10}$$

The information about the state of polarization (SOP) of the electromagnetic field can be reduced to a single vector on the (**x**,**y**) plane , called Jones vector.

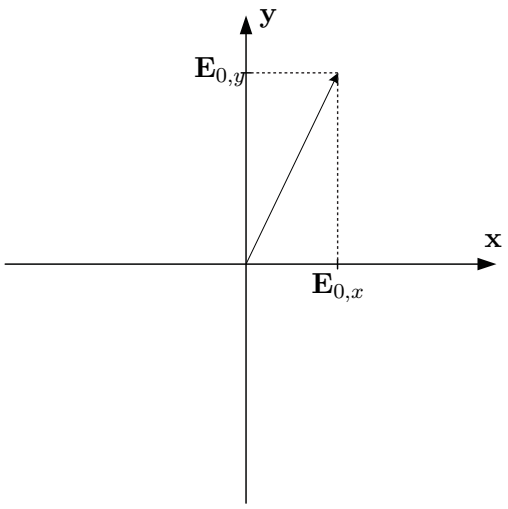

Figure 2.2: Jones vector in the (**x**,**y**) polarization plane.

In Figure 2.2 the Jones vector is shown. By definition it is:

$$\bar{\mathbf{e}}(z,t) = \begin{pmatrix} \mathbf{E}_{0,x}(z,t) \\ \mathbf{E}_{0,y}(z,t) \end{pmatrix}. \tag{2.11}$$

If we now define the normalized Jones vector $\mathbf{e}(z,t)$ as:

$$\mathbf{e}(z,t) = \frac{1}{\sqrt{|\mathbf{E}_{0,x}(z,t)|^2 + |\mathbf{E}_{0,y}(z,t)|^2}}\,\bar{\mathbf{e}}(z,t), \tag{2.12}$$

through (2.12) we can express (2.10) as:

$$\mathbf{E}_0(z,t) = \kappa\, e^{-j\phi(z,t)}\sqrt{A_x^2(z,t) + A_y^2(z,t)}\;\mathbf{e}(z,t) \tag{2.13}$$

and thus:

$$\mathbf{E}_0(z,t) = \kappa\sqrt{P(z,t)}\; e^{-j\phi(z,t)}\;\mathbf{e}(z,t). \tag{2.14}$$

Hence, it is possible to notice how $\mathbf{E}_0(z,t)$ is proportional to the complex envelope of the field multiplied by a unit vector describing the SOP of the electromagnetic field.

For the completeness of our study the explicit spatial dependence of the field is not necessary and thus it is possible to simplify (2.4) as:

$$\mathbf{E}(t) = \mathrm{Re}\left\{\kappa\sqrt{P(t)}\, e^{-j\phi(t)}\, e^{j\omega_0 t}\, \mathbf{e}(t)\right\}. \tag{2.15}$$

It is important to note that the constant κ can be dropped to simplify the notation, but its dimension must be taken into account in order to ensure that $\mathbf{E}$ has the dimension of an electric field (V/m).

Trying to characterize an electromagnetic field described by (2.15) in Matlab® we incur in a major implementation problem. The resolution of our time array cannot be enough to represent a signal oscillating at frequency $f_0 = \omega_0/2\pi$. In fact, if $f_0 = 193.12$ THz (i.e. the optical frequency most often used in optical communication systems), to describe an optical signal with a symbol rate of 10 GBd/s we would need more than 38461 samples per symbol.

Therefore, we downgrade to baseband the field equation (2.15) multiplying it by $e^{-j\omega_{ref}t}$. The frequency $f_{ref} = \omega_{ref}/2\pi$, that we call *reference frequency*, is kept fixed for all the optical signals. This is done in order to be able to discern different optical frequencies. In our model, we chose $f_{ref} = 193.12$ Thz.

2.6 Fourier Transform and Frequency Domain Representation

In telecommunication and signal processing we refer often to the description of a signal in the time domain and in the frequency domain. In order to understand how to move from one domain to the other, it is important to clarify the concept of Fourier and inverse Fourier transform. In this thesis, the definition used of Fourier transform and inverse Fourier transform between the time and frequency domains for a continuous signal are:

$$H(f) = \mathcal{F}(h(t)) = \int_{-\infty}^{+\infty} h(t)e^{-j2\pi ft}dt, \tag{2.16}$$

and

$$h(t) = \mathcal{F}^{-1}(h(t)) = \int_{-\infty}^{+\infty} h(t)e^{-j2\pi ft}dt. \tag{2.17}$$

Conversely, if the signal is discrete the discrete Fourier transform and inverse discrete Fourier transform are defined as:

$$H(k) = \sum_{l=1}^{N} h(l) e^{-j2\pi/N(l-1)(k-1)} \tag{2.18}$$

and

$$h(l) = \frac{1}{N} \sum_{l=1}^{N} H(k) e^{j2\pi/N(l-1)(k-1)} \tag{2.19}$$

2.7 Power Spectral Density

In a signal processing, the Power Spectral Density (PSD) is a positive real function in the frequency domain which has the dimension of power per Hertz. The PSD (often called *spectrum* of the signal) describes how the power of a signal is distributed with frequency.

Due to the fact that the Fourier transform of a squared signal with non-zero mean does not exist, the PSD is defined as the Fourier transform of the autocorrelation function $\mathcal{R}(\tau) = h^*(-\tau) * h(\tau) = \int_{-\infty}^{+\infty} h(t)h(t-\tau)^* dt$:

$$S(f) = \mathcal{F}(\mathcal{R}(\tau)) = \int_{-\infty}^{+\infty} R(\tau) e^{-j2\pi f\tau} dt \tag{2.20}$$

2.8 Gray Coding

The reflected binary code, also called Gray code, consists in a binary numeral system in which two adjacent values differ in only one bit.

When possible, it is preferable to Gray code the transmitted signal. This means that two symbols, adjacent in the complex field constellation, correspond to two binary symbols that differ in only one bit.

The advantage brought by this technique is related to the fact that if an error occurs in the signal detection, it is more likely that a symbol is confused with one of its neighbors than with one of the others. Thus, having Gray coded the symbol sequence the amount of wrong bits in the received symbols sequence is minimized.

3

System Theory

In this chapter we are going to study the different elements present in an optical communication system. In Figure 3.1 the block diagram of a generic multiple channel PolMux system is shown. Here, all the elements present in this diagram will be studied and deeply discussed. Afterwards, in Chapter 4, the Matlab® implementation of such a system will be developed.

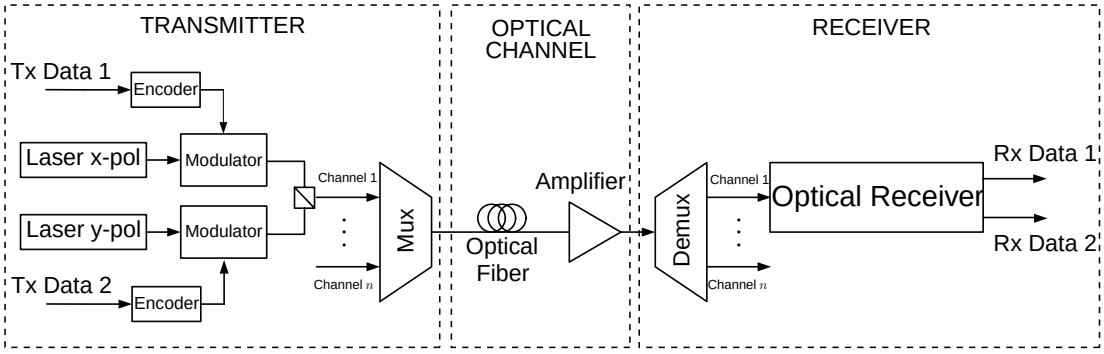

Figure 3.1: Block diagram of a generic multiple channel optical communication system.

3.1 Optical Transmitter

An optical transmitter is needed in order to convert the electrical signal to an optical one. In this section we will present the theory behind the basic elements of an optical transmitter. First, we give the theoretical background needed to understand the functioning of a laser CW (i.e. the most used optical source in high speed opti-

cal communication). Afterwards, we analyze the optical modulators and the different transmitter setups used in this project.

3.1.1 Laser CW

The main component used to generate an optical signal is a laser. Ideally, the perfect optical signal is a lightwave with constant amplitude, constant frequency, and constant phase. In practice, this cannot be obtained, but the lightwave generated by a laser has characteristics very close to the ideal one.

In order to understand how the light is generated in a laser we have to define the possible radiative processes that can occur. Considering the hypothesis of quantized energy, we can simplistically describe the laser system as a set of many atoms with many energy levels $E_1, E_2, \dots$ with $E_i = h\nu_1$. Let us assume that our system consists in atoms with just two levels E_1 and E_2.

In the case a photon with energy $h\nu_p = E_2 - E_1$ is absorbed by the laser system an atom with energy E_1 will be excited to the energy level E_2. This process is called *stimulated absorption*.

If a photon with energy $h\nu_p = E_2 - E_1$ interacts with an atom of the laser system that is already in the excited level E_2, the atom will relax to the energy level E_1 emitting a photon with exactly the same frequency, phase, sense of polarization and direction of the original one. This process is called *stimulated emission*.

The last process, called *spontaneous emission*, occurs when an atom in the excited energy level E_2 spontaneously relaxes to the energy level E_1. Also in this case a photon with energy $h\nu = E_2 - E_1$ is emitted by the system, but it has a random phase and direction [21].

The main phenomenon that occurs during the generation of a lightwave in a laser is stimulated emission. Indeed, the photons trapped in the optical cavity stimulate the emission of other photons with identical characteristics, generating, when an equilibrium is reached, a lightwave that ideally has constant frequency, phase, amplitude, and polarization. As shown in Section 2.5, the electromagnetic field of such a lightwave can be expressed in the complex notation as:

$$\mathbf{E}_s(t) = \sqrt{P_s}\, e^{-j\phi_s} e^{j\omega_s t} \cdot \mathbf{e}_s \tag{3.1}$$

where P_s, ϕ_s, and ω_s are the power, phase and frequency of the lightwave and are considered constant. In the case of a real laser, (3.1) should be modified in order to take into account both *phase noise* and *intensity noise*.

The phase noise is due to the presence of spontaneous emission events in the laser. When a photon is generated by spontaneous emission it has random phase and direction. The small part of these photons that have the same direction of the laser lightwave photons, will contribute in altering the ideal constant phase ϕ_s of (3.1) as:

$$\mathbf{E}_s(t) = \sqrt{P_s}\, e^{-j(\phi_s+\phi_n(t))} e^{j\omega_s t} \cdot \mathbf{e}_s \tag{3.2}$$

The phase noise can be seen as random jumps of the term $\phi_n(t)$. Thus ϕ_n changes in a time interval τ as:

$$\phi_n(t+\tau) = \phi_n(t) + \delta_n(t+\tau) \tag{3.3}$$

Since, the high number of spontaneous emission events contributes independently on the phase noise, the random phase change δ_n can be modeled as Gaussian distributed according to the Central Limit Theorem [10].

The linewidth of the laser is strictly related to the phase noise. The more frequent the random phase jumps are, the broader the laser spectrum is. An analytical derivation of the relation between the variance of the random phase change δ_n and the laser linewidth can be found in [10] and it yields to:

$$\sigma^2_{\delta_n} = 2\pi\ \Delta\nu_d|\tau|. \tag{3.4}$$

The intensity noise in a laser results both from quantum effects and from other technical noise sources. Generally the lowest possible intensity noise that can be obtained is given by the shot noise. This is due to the quantization of photons and electrons.

The fluctuation in the laser power can be expressed substituting P_s in (3.1) with:

$$P_{s_n}(t) = P_s + \delta P(t), \tag{3.5}$$

The intensity noise in a laser is generally measured through the Relative Intensity Noise (RIN). The RIN gives the ratio between the variance of the intensity noise over the squared average power:

$$\mathrm{RIN} = \frac{\langle \delta P^2(t) \rangle}{\langle P(t) \rangle^2} \tag{3.6}$$

where the squared average power is simply equal to P_s^2.

Sometimes, in the laser specification, the RIN is given in dB/Hz and represents the RIN per unit bandwidth. In this case the full RIN is found integrating the RIN per unit bandwidth over the (sigle-sided) detection bandwidth Δf of the system:

$$\int_0^{\Delta f} \mathrm{RIN}_{\mathrm{dB/Hz}}(f)df = \frac{\langle \delta P^2(t) \rangle}{\langle P(t) \rangle^2}. \tag{3.7}$$

Typical values for the RIN per unit bandwidth in laser diodes range from -160 dB/Hz to -130 dB/Hz [10].

3.1.2 Optical Modulators

What we have seen in the previous section is the model for a laser CW with constant amplitude. The next step is transferring the information given in the electrical domain in the optical domain. This can be done in two ways: either a direct modulation of the optical source is applied or the constant amplitude lightwave is modulated afterwards by an external modulator.

In the case of high bit rates and high order modulation formats the latter is usually employed. Thus, in this section only external modulators will be treated.

3.1.2.1 Phase Modulator

The key component of an external optical modulator is the phase modulator. Such a device is made of a particular crystal the refractive index of which depends linearly on the voltage applied to the material. This phenomenon is called linear electro-optic effect (or *Pockels effect*) and it makes possible the phase modulation of the light propagating through the crystal. In fact, the phase shift experienced by the lightwave is:

$$\phi_{PM} = \frac{2\pi}{\lambda}\, l\, n(V), \tag{3.8}$$

where l is the length of the cell and $n(V)$ is the refractive index of the crystal that depends on the voltage V.

Since this dependence is linear, the phase shift can be written also as:

$$\phi_{PM} = \pi \frac{V}{V_\pi}, \tag{3.9}$$

where V_π is called *half-way voltage* and is the voltage needed to obtain a phase shift of π. Hence, the relation between the incoming electric field E_{in} and the modulated one

$E_{out}(t)$ is:

$$E_{out}(t) = E_{in}\, e^{-j\pi \frac{V(t)}{V_\pi}} \tag{3.10}$$

The variation of the refractive index n does not occur instantaneously in an homogeneous fashion along the crystal length l. This phenomenon creates a bandwidth limitation in the phase modulator. The analysis of this effect is beyond the purpose of our project, but it has been extensively studied in [22].

Phase modulators can be fabricated as an integrated optical device by embedding an optical waveguide in an electro-optical substrate (e.g. $LiNbO_3$). The value of the half-wave voltage V_π depends on the material used and on the dimensions l and h of the phase modulator, and it is generally between 3 and 6 V.

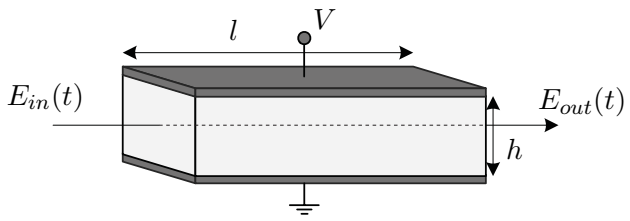

Figure 3.2: Optical phase modulator.

3.1.2.2 Mach-Zehnder Modulator

A Mach-Zehnder (MZ) modulator exploits the principle of interference in order to modulate a signal. The structure of a MZ modulator is shown in Figure 3.3.

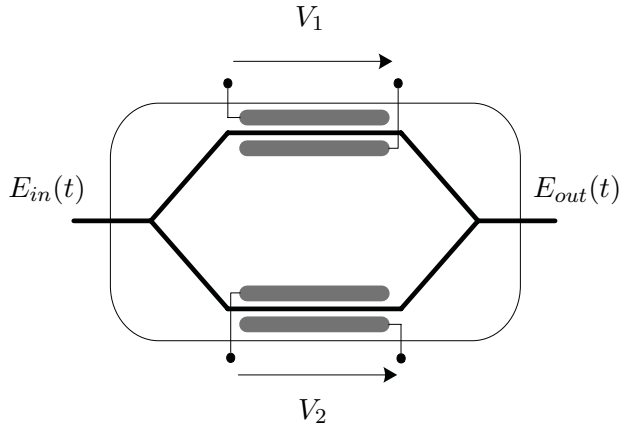

Figure 3.3: Optical Mach-Zehnder modulator.

In order to understand the mechanism that allows for modulation in a MZ modulator, let us first call the phase shifts experienced in the two branches ϕ_1 and ϕ_2. Thus, when the electric fields on the two arms recombines after the phase modulation, the output field is:

$$E_{out} = \frac{1}{2}E_{in}\left[e^{-j\phi_1} + e^{-j\phi_2}\right] = E_{in}\cos\left[\frac{\phi_2 - \phi_1}{2}\right]e^{-j\left(\frac{\phi_1+\phi_2}{2}\right)} \tag{3.11}$$

If the two phase shifts are now chosen as $\phi_1 = \phi_2 = 0$, then $E_{out} = E_{in}$. If instead $\phi_2 - \phi_1 = \pi$ then $E_{out} = 0$. It is therefore clear how modulating the phase on the two arms of the MZ interferometer we can obtain a modulation on the input field E_{in} (e.g. in the case just described an intensity modulation).

Using (3.9) in (3.11) it is possible to express the output field of the MZ interferometer as a function of the two voltages applied to the two phase modulators (see Figure 3.3):

$$E_{out} = E_{in}\cos\left[\frac{\pi}{2V_\pi}(V_2 - V_1)\right]e^{-j\frac{\pi}{2V_\pi}(V_1+V_2)}. \tag{3.12}$$

When the phase shift in one arm is the opposite of the one in the other arm (i.e. $V_2 = -V_1$), the MZ interferometer operates in a push-pull mode and a chirp-free operation is obtained. In this case, expressing the output field as function of the difference $\Delta V = V_2 - V_1$, we have:

$$E_{out} = E_{in}\cos\left[\frac{\pi}{2V_\pi}\Delta V\right], \tag{3.13}$$

and the output power is:

$$P_{out} = P_{in}\cos^2\left[\frac{\pi}{2V_\pi}\Delta V\right]. \tag{3.14}$$

In Figure 3.4 the MZ modulator transfer characteristic is shown. The point marked as OP is the operating voltage between which the applied voltage ΔV is modulated. In Figure 3.4(a) OP is set at $V_\pi/2$ and the peak-to-peak value of ΔV is V_π. It is easy to see how this yields to an intensity modulation with the output power P_{out} that oscillates between P_{in} and 0.

If instead the operating point is at 0, as in Figure 3.4(b), and the peak-to-peak value of ΔV is $2V_\pi$, the obtained modulation is a phase modulation. In fact at $\Delta V_1 = 0$ the output electric field is $E_{out} = E_{in}$ and at $\Delta V_2 = -2V_\pi$ the output electric field is $E_{out} = -E_{in}$. This means that the phase difference between the output and the input electric field is either 0 or π allowing for a binary phase modulation.

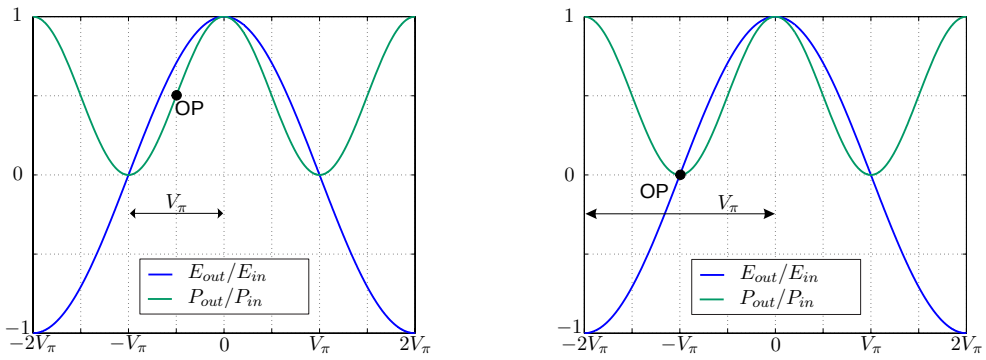

Figure 3.4: Operating point for a MZ modulator used for (a) intensity modulation and (b) phase modulation

3.1.2.3 IQ Modulator

The last modulator structure presented is the optical IQ modulator. From Figure 3.5 it can be seen how an IQ modulator exploits, in an interferometric structure, two MZ interferometers and a phase modulator. The upper arm is called in-phase (I) arm and the lower quadrature (Q) arm. In both arms a modulation of the signal is performed by a MZ interferometer but in the Q arm the signal experiences an additional phase shift of $\pi/2$ given by a phase modulator (from it the name quadrature arm). The two MZ interferometer can be used in push-pull mode to obtain an amplitude modulation (as shown in Figure 3.4(a)). Because of the $\pi/2$ phase shift, the resulting output field is:

$$E_{out} = \frac{1}{2}E_{in} \cdot \cos\left[\frac{\pi}{2V_\pi}V_I\right] + \frac{1}{2}E_{in} \cdot j\cos\left[\frac{\pi}{2V_\pi}V_Q\right]. \tag{3.15}$$

This means that, with appropriate values of V_I and V_Q, it is possible to reach all the point shown in Figure 3.5(b).

3.1.3 OOK Transmitter

In the following four sections we present the setups used in this project for the four modulation formats employed: OOK, DBPSK, DQPSK and 16QAM. We start from the OOK.

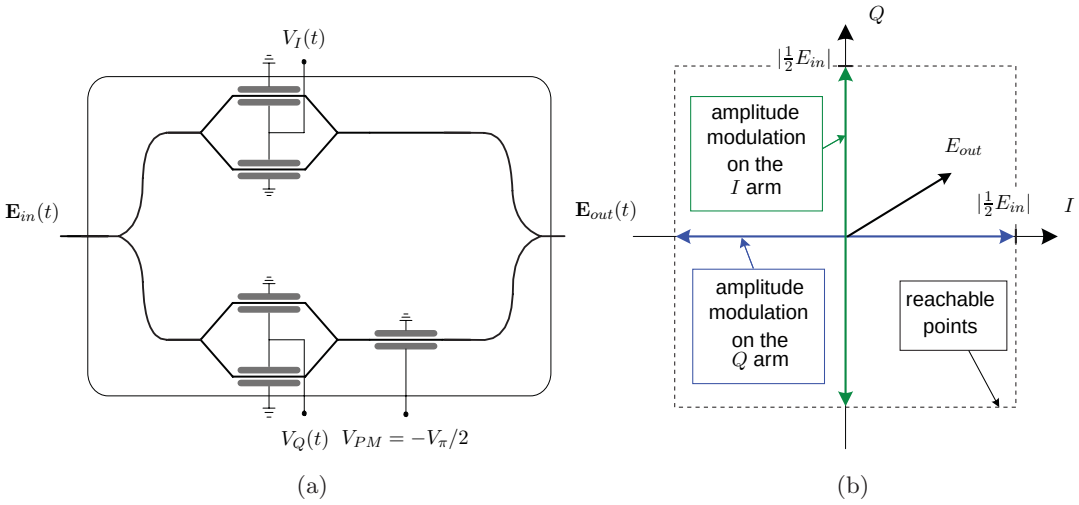

Figure 3.5: (a) Structure of an Optical IQ modulator and (b) reachable points on the constellation using an IQ modulator.

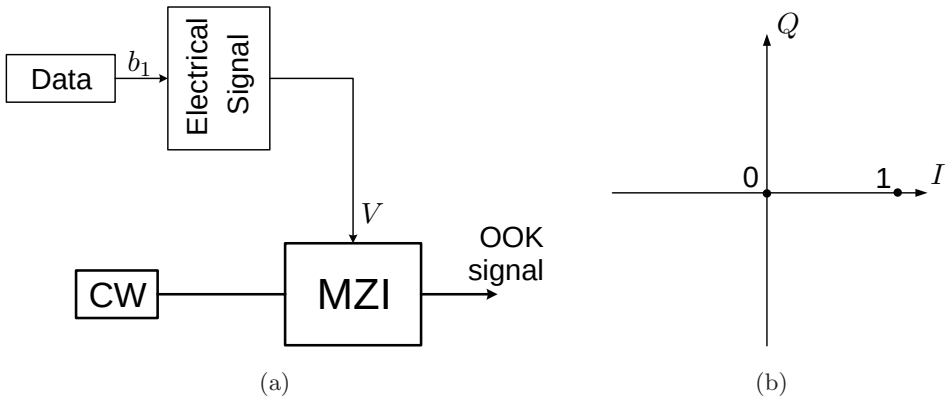

Figure 3.6: (a) Block diagram of an OOK transmitter and (b) OOK constellation.

As we already said in Section 3.1.2.2, a MZ interferometer can be used in push-pull mode with the operating point at $V_\pi/2$ and peak-to-peak driving voltage of V_π in order to obtain amplitude modulation. Thus, only a Laser CW and a MZ interferometer are necessary to obtain an OOK modulation.

The transmitter output power is:

$$P_{out} = P_s \cdot \cos^2\left[\frac{\pi}{2V_\pi}V_{0,1}\right] \tag{3.16}$$

where the voltage $V_0 = V_\pi/2$ corresponds to an input bit 0 and gives as output $P_{out} = 0$ and $V_1 = 0$ corresponds to an input bit 1 and gives as output $P_{out} = P_s$.

3.1.4 DBPSK Transmitter

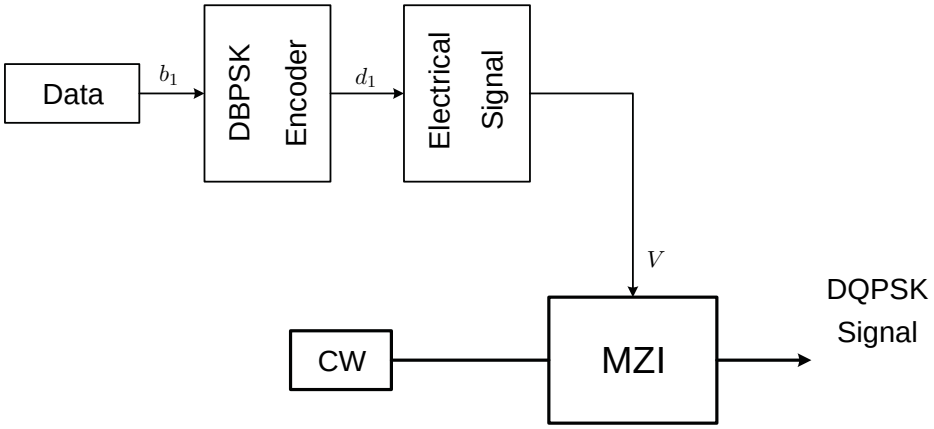

Figure 3.7: Block diagram of an DBPSK transmitter.

Two different methods are possible to generate a binary phase modulated signal. The simplest is to use only a phase modulator driven by binary sequence. This is surely a cheap and easy solution, but due to the linear dependence of the induced phase shift on the applied voltage, the eye opening is reduced by the noise on the electric signal. The other possibility is to use a MZ interferometer with OP at V_π and the peak-to-peak driving voltage is $2V_\pi$. In this way a binary phase modulation is obtained.

The latter is the only DBPSK transmitter setup used in this project. It is interesting to notice how, in the case of phase modulation with a MZ interferometer in push-pull mode, the noise ripples on the electrical signal is almost completely suppressed on the phase modulated optical signal [23]. This can be easily understood from Figure 3.4(b).

The field transfer function around the points $-2V_\pi$ and 0 is not linear but relatively flat (due to its sinusoidal trend). In this way, noise on the driving voltage ΔV is highly suppressed when it is transferred to the optical signal through the MZ interferometer. This was not the case of the MZ interferometer for amplitude modulation. In fact, the power transfer function is relatively linear at the point $V_\pi/2$ and therefore any oscillation on the driving voltage will be linearly transferred to the optical power of the modulated signal.

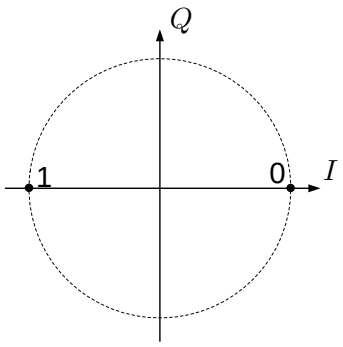

Figure 3.8: DBPSK constellation.

As already explained in Section 2.1, in order to use phase modulation with direct detection it is necessary to differentially encode the data before modulating the optical signal. Moreover, also in the case of coherent detection with DSP, it is often preferred to differentially encode the signal in order to recovery the carrier phase without employing synchronization sequences. Thus, all the phase modulation formats used in this project are differentially encoded.

In the case of DBPSK the differential encoder is fairly simple and the output of the decoder y depends on the input bit sequence x as:

$$d_k = d_{k-1} \oplus b_k. \tag{3.17}$$

As shown in Figure 3.7, the signal that drives the MZ modulator is the electrical signal generated by the differentially encoded signal. This means that the DBPSK constellation shown in Figure 3.8 represents the differentially encoded bits d_k.

From (3.13) the output field of the DPSK transmitter is:

$$E_{out} = \sqrt{P_s} \cdot \cos\left[\frac{\pi}{2V_\pi} V_{0,1}\right] \tag{3.18}$$

where the voltage $V_0 = 0$ corresponds to a 0 on the differentially encoded bit sequence and gives as output $E_{out} = \sqrt{P_s}$ (i.e. the signal phase $\phi_s = 0$) and $V_1 = -2V_\pi$ corresponds to a 1 on the differentially encoded bit sequence and gives as output $E_{out} = -\sqrt{P_s}$ (i.e. the signal phase $\phi_s = \pi$).

3.1.5 DQPSK Transmitter

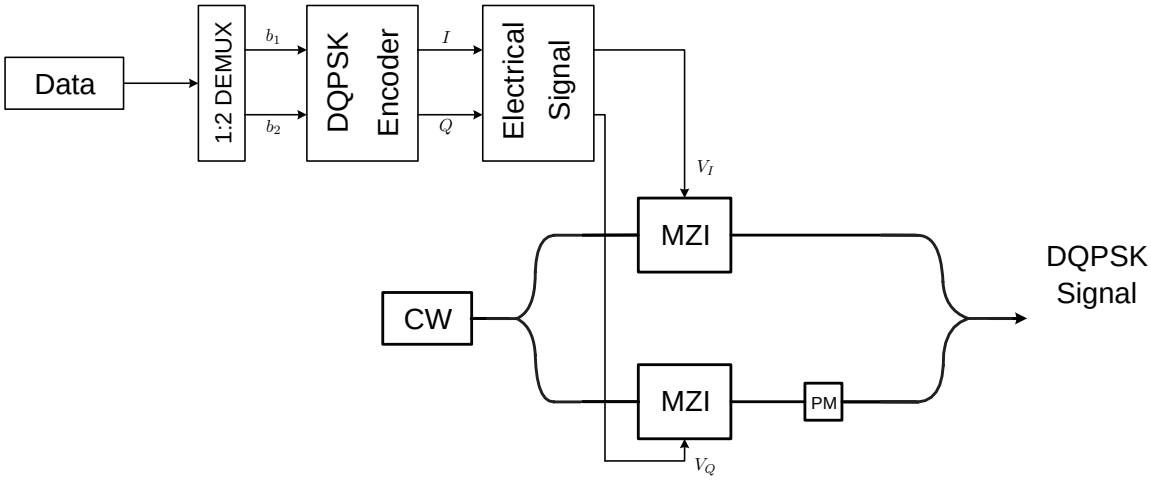

Figure 3.9: Block diagram of an DQPSK transmitter.

Also in the case of DQPSK it is possible to modulate a phase modulator with a multilevel signal in order to obtain a DQPSK signal. Even more than for the DPSK modulator the noise in the electrical signal would highly impair the optical signal generated in such a transmitter.

A second possibility is to use a MZ interferometer followed by a phase modulator that adds a $\pi/2$ modulation. In this way a perfect π phase modulation is obtained in the first stage, but the phase modulator that follows can still affect the optical signal linearly transferring the noise of the electrical signal that drives it.

The third way to obtain a DQPSK signal is to employ a parallel structure using an IQ modulator. If two phase modulations are employed on the two MZ of the IQ modulator from (3.15) the output electric field will be:

$$E_{out} = \frac{1}{2}\sqrt{P_s} \cdot e^{-j\cdot\phi_s} \tag{3.19}$$

where

$$\phi_s = \begin{cases} \pi/4 & \text{if } V_I = 0 \text{ and } V_Q = 0 \\ 3\pi/4 & \text{if } V_I = -2V_\pi \text{ and } V_Q = 0 \\ 5\pi/4 & \text{if } V_I = -2V_\pi \text{ and } V_Q = -2V_\pi \\ 7\pi/4 & \text{if } V_I = 0 \text{ and } V_Q = -2V_\pi \end{cases} \tag{3.20}$$

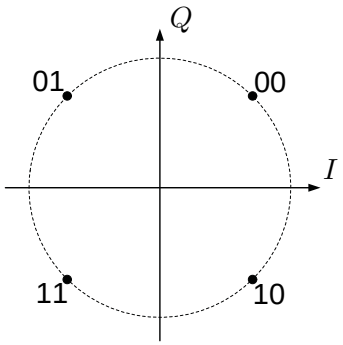

Figure 3.10: DQPSK constellation generated by a transmitter that employs a parallel structure.

As explained in [24], in the case of DQPSK with parallel transmitter, the differential encoding for the driving signals I and Q of the IQ modulators is given by:

$$I_k = \overline{(u_k \oplus v_k)}(u_k \oplus I_{k-1}) + (u_k \oplus v_k)(v_k \oplus Q_{k-1}) \tag{3.21}$$

$$Q_k = \overline{(u_k \oplus v_k)}(v_k \oplus Q_{k-1}) + (u_k \oplus v_k)(u_k \oplus I_{k-1}) \tag{3.22}$$

Again, also in the case of the DQPSK transmitter, the driving signal of the IQ modulator is the differentially encoded signal. Thus, the symbols shown in the constellation of FIgure 3.10, represent the $\{Q_k, I_k\}$ couples.

3.1.6 Star 16QAM Transmitter

In order to further increase the degree of freedom on the optical modulation it is possible to act on both the phase and the amplitude of the signal field. A common way to do this is to employ Quadrature Amplitude Modulation (QAM).

In Figure 3.11 the constellation of a Star 16QAM and a Square 16QAM are shown. In the case of Star QAM the points on the constellation lie on multiple circle and have equally spaced phases (Figure 3.11(a)). This causes the points on the inner circle to be closer together than the symbols on the outer one. In order to improve the noise performance, the symbols of a QAM modulation can be placed in equally spaced

points as in the case of a Square QAM (Figure 3.11(b)). This does not just lead to an improvement in terms of noise performance, but allows also for simpler modulations and demodulation schemes.

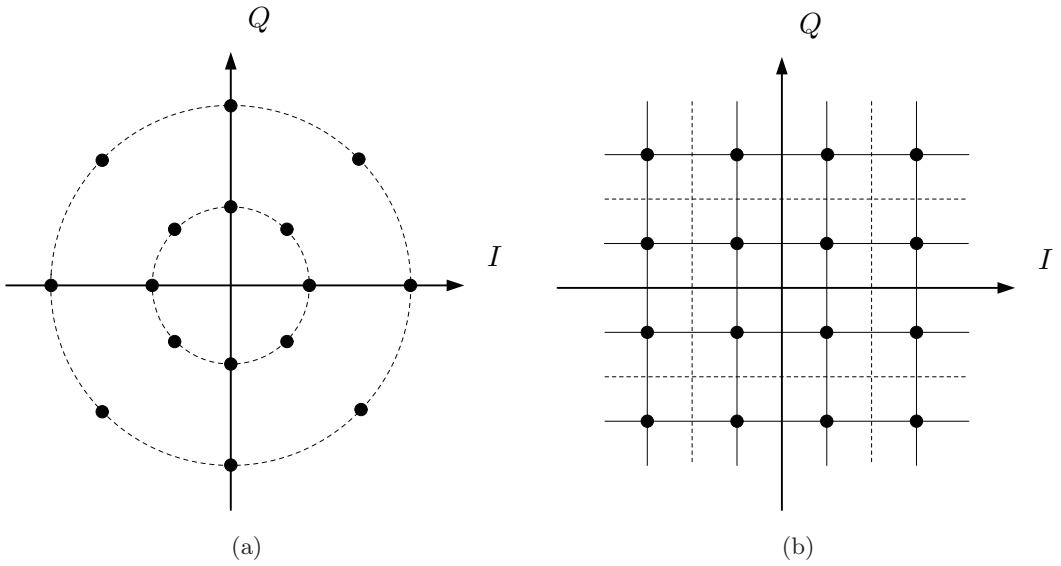

Figure 3.11: Constellations of (a) Star 16QAM and (b) Square 16QAM

In our model we only used Square 16QAM and its transmitter implementation has been carried out in a parallel structure employing two IQ modulators. In this section we are going to describe and study only the structure used in this project.

In Figure 3.12 it is possible to see how the core of the optical transmitter is made of an interferometric structure that combines two IQ modulators with a difference in the amplitude between the two arms of 6 dB. In this way it is possible to combine two QPSK modulations that interfering together create a Square 16QAM modulation.

3.1.6.1 Differential Quadrant Encoding

As in the case of QPSK signals, in a Square QAM signal a phase ambiguity of n times $\pi/2$ with $n \in (0, 1, 2, 3)$ arises at the carrier synchronization. This results in a quadrant ambiguity that means that after the carrier synchronization the symbols of a specific color in Figure 3.13(a) are not in the quadrant assigned at the transmitter side (e.g. the red once in quadrant I or the green ones in quadrant III) but they can be in whichever of the four quadrants.

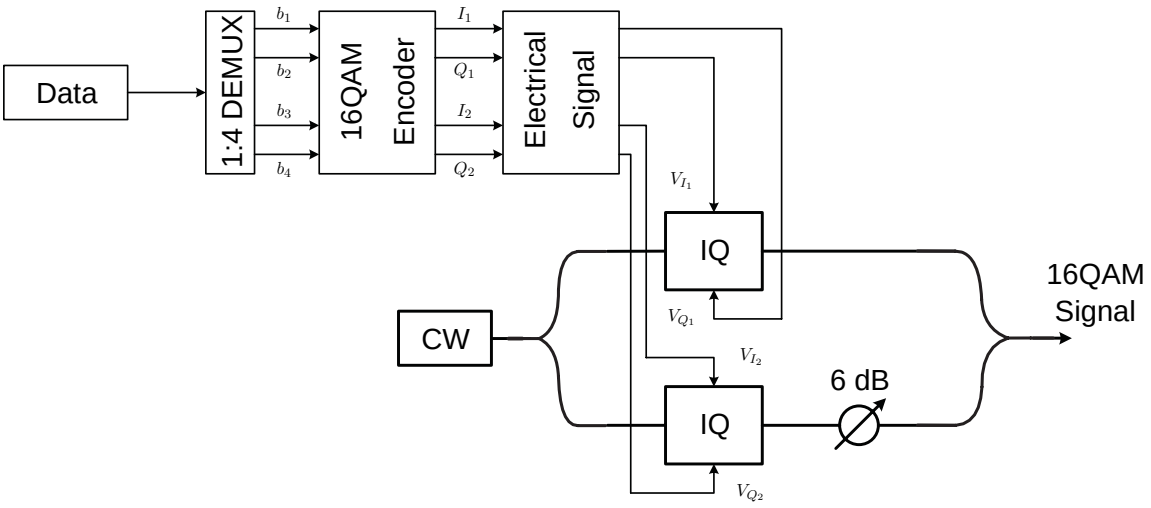

Figure 3.12: Block diagram of an 16QAM transmitter.

In order to solve this ambiguity it is possible to employ the *differential quadrant encoding* scheme. Out of the four bits (b_1, b_2, b_3, b_4) that describe each Square 16QAM symbol, two contain the information of the symbol quadrant and the other two the position of the symbol in the quadrant. Differentially encoding the former two with a DQPSK encoder, it is possible to solve the phase ambiguity at the receiver side. The other two bits can be mapped in a rotation symmetric way so that the quadrant rotation does not affect the correct demodulation of these two. In Figure 3.13(b) the mapping for the Square 16QAM symbols used in this project is shown. It can be noticed that any rotation of $n\pi/2$ does not affect the last two bits of each symbol.

The penalty introduced by the differential encoding for a 16-QAM modulation differential quadrant encoded is less then the one for the DQPSK modulation (i.e. 2.2 dB versus 3 dB). Indeed, just two out of four bits are differentially encoded. However, due to the necessity of a rotation symmetric encoding of the other two bits, the differential quadrant encoded 16-QAM cannot be Gray coded.

After being processed by the 16QAM encoder the four driving voltages $(V_{I_1}, V_{Q_1}, V_{I_2}, V_{Q_2})$ of the two IQ modulators are generated.

3.1.7 Pulse Carvers and Pulsed Sources

The shape of the optical pulses strongly affects the performance of the optical transmission. The most employed pulse shape in commercial systems is called Non-Return-

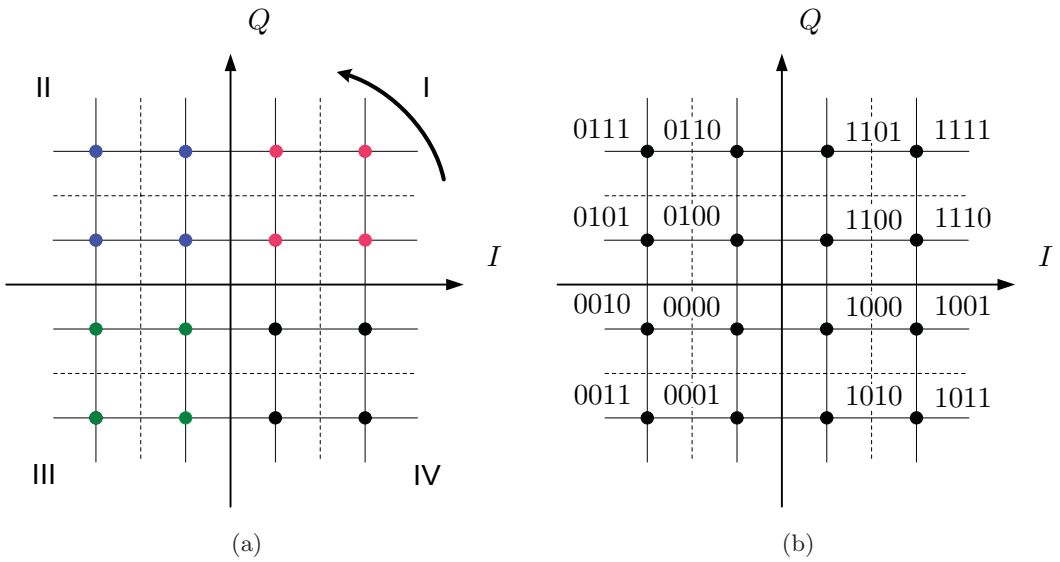

Figure 3.13: (a) Quadrant ambiguity in a Square 16QAM and (b) mapping of a Square 16QAM signal.

to-Zero (NRZ) and in it the power does not always go to zero when passing from one symbol to another. Conversely, in the case of Return-to-Zero (RZ) formats, the optical power goes to zero within the symbol slot. Thus, RZ formats allows for smaller power during the symbol transitions and so the effects of chirp during the phase transitions are significantly reduced, according to the pulse width and the rise time of the electrical driving signals [1], [10].

In order to obtain RZ formats it is possible to act in three ways: either employing electrical RZ waveforms to drive the optical modulators or carving RZ pulses in the optical domain or using a pulsed source instead of a CW laser.

An MZ interferometer, that modulates the output of an optical transmitter, can be used to carve RZ pulses with a duty cycle of 50% (see Figure 3.14(a)). In fact, if the signal used to drive the MZ interferometer is:

$$\Delta V = \frac{V_\pi}{2} + \frac{V_\pi}{2}\sin(2\pi\frac{t}{T_s} - \frac{\pi}{2}), \tag{3.23}$$

then from (3.13) we can derive the transfer characteristic of the pulse carver:

$$\frac{E_{out}(t)}{E_{in}(t)} = \cos\left[\frac{\pi}{4}\cdot\sin\left(2\pi\frac{t}{T_s} - \frac{\pi}{2}\right) - \frac{\pi}{4}\right], \tag{3.24}$$

that produces the pulses shown in Figure 3.14(b).

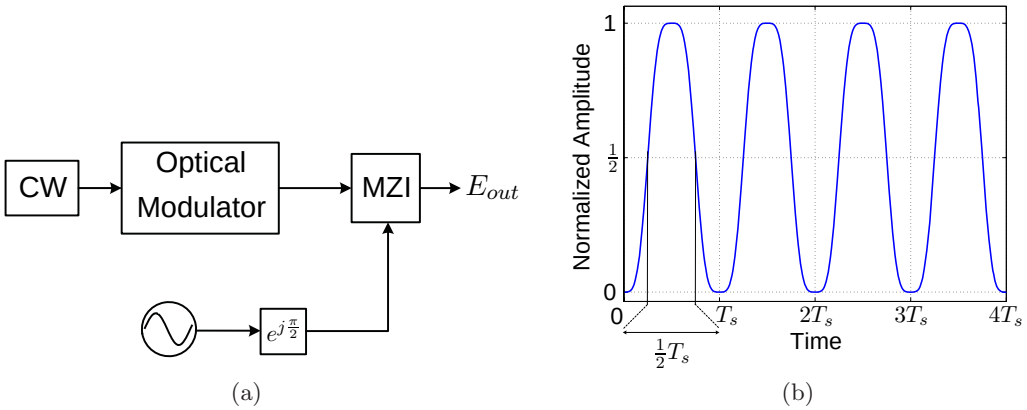

Figure 3.14: (a) Block diagram of a RZ pulse carver and (b) the obtained 50% pulses.

RZ formats can be obtained also by means of a pulsed source (e.g. a mode-locked laser). These sources have been extensively used in this project but we have not delved into their study and characterization. A deeper analysis of the pulsed sources used and their Matlab® models has been carried out in [22].

3.1.8 Polarization Multiplexer

The same fiber supports two modes orthogonally polarized that are degenerate and have the same mode index. Thus, exploiting two optical signal orthogonally polarized it is possible to double the capacity of our optical communication system. The two optical signal can be combined together through a Polarization Beam Combiner (PBC), thus without an increase in the complexity of the transmitter, obtaining a Polarization Multiplexed (PolMux) signal.

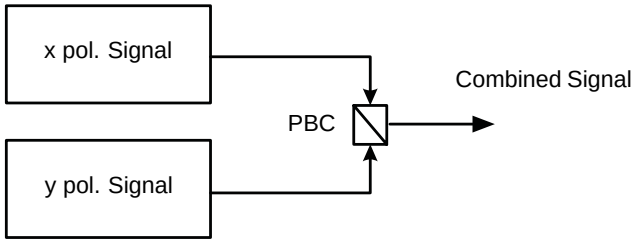

Figure 3.15: Polarization multiplexing.

However, due to fiber birefringence the SOP of the received signal is unknown (see section 3.2.3). This means that the original SOP must be recovered in order to correctly

detect the received signal. If this is possible in a coherent receiver, in a simple direct detection scheme this cannot be done.

3.1.9 Optical Time Division Multiplexer

As already explained in section 2.2, the OTDM technique consists in time-multiplexing n channels in the optical domain. The method used to obtain a optical multiplexer is shown in Figure 3.16. A pulsed source produces pulses every T_S. Moreover, these pulses must have a width T_p that is shorter than T_S/n, where n is the number of OTDM channels, ensuring that each pulse fits in its allocated time slot. These pulses are then split in n branches. The optical signal in each branch is firstly modulated and then delayed of $(k-1)\cdot T_S/n$ where $k \in \{1,\ldots,n\}$ is the number of the channel. Afterwards the n signals are combined together. However, due to the delay previously introduced, the pulses of the n branches will not overlap but will fall in each of the n portions of the symbol slot.

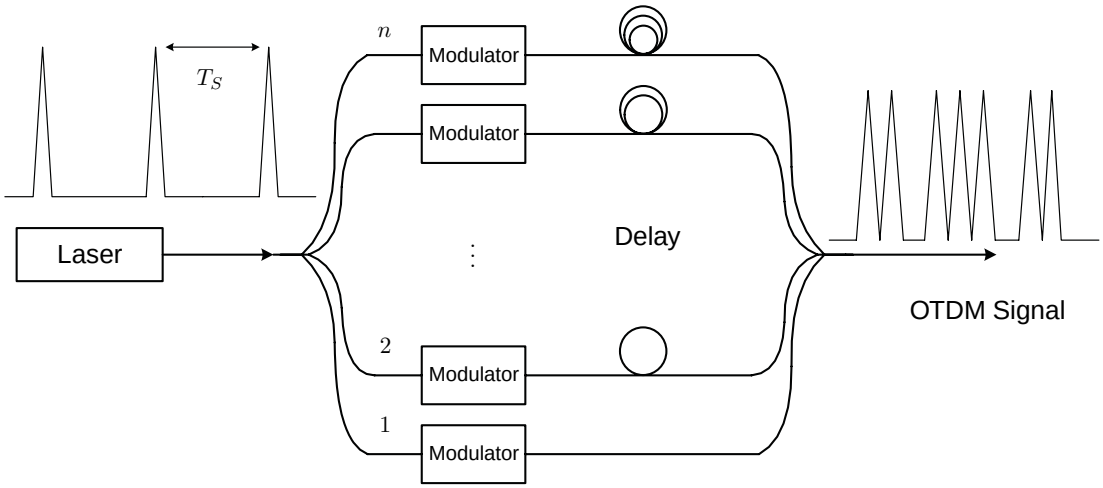

Figure 3.16: Optical Multiplexer suitable for an OTDM system.

If we exclude the optical modulators, the entire OTDM multiplexer can be built using single-mode fibers. In fact, in order to obtain the different delay lines it is possible to use pieces of fiber of different lengths. However, this approach is not feasible for high bit rates where the precision requires is very high (e.g. for a 40 Gb/s OTDM signal the fiber length should have a precision of around 20 μm). Thus, more precise approaches

(e.g. planar lightwave circuits that make use of the silica-on-silicon technology) are generally used for high speed OTDM multiplexers [1].

3.2 Optical Channel

In order to deliver the information to the receiver the optical signal is sent through an optical fiber. During its propagation along the fiber the signal is distorted by the several linear and nonlinear degradation effects that characterize fiber optic transmission.

In this chapter we will give a brief theoretical introduction to the most important degradation effects developed in our model. In [22] a wider study of the fiber propagation effects and of a possible model implementation has been developed.

3.2.1 Fiber Attenuation

Neglecting the effects of chromatic dispersion and the Kerr nonlinearities in (2.4), the complex envelope of the electrical field at the output of an optical fiber of length L is given by:

$$\mathbf{E}_0(z = L, t) = \mathbf{E}_0(z = 0, t) \cdot e^{-\frac{\alpha}{2}L} \tag{3.25}$$

where $z = 0$ denotes the fiber input and $z = L$ the fiber output. The evolution of the optical power can be derived from the one of the complex electric field as:

$$P(z = L, t) = \mathbf{E}_0(z = L, t) \cdot \mathbf{E}_0(z = L, t)^* = P(z = 0, t) \cdot e^{-\alpha \cdot L}. \tag{3.26}$$

The attenuation coefficient α has the unit of km^{-1} and is commonly expressed in dB/km. The usual values of fiber loss are between 0.2 and 0.25 dB/km at $\lambda = 1550$ nm and they can be considered constant within the modulation bandwidth of a single channel [1] [10]. The compensation of fiber losses can be done with optical amplifier such as EDFAs. We will briefly discuss about optical amplifiers and their related issues in Section 3.2.4.

3.2.2 Chromatic Dispersion

Let us consider a single mode fiber of length L. A spectral component of the lightwave at the angular frequency ω would arrive at the output of the fiber after a time $T = L/\nu_g$, where the *group velocity* ν_g is defined as [1]:

$$\nu_g = (d\beta/d\omega)^{-1}. \tag{3.27}$$

where $\beta = \bar{n}k_0 = \bar{n}\omega/c$ is the propagation constant. We can now expand the frequency dependent propagation constant $\beta(\omega)$ into a Taylor series around the central frequency ω_0:

$$\beta(\omega) = \beta_0 + \beta_1(\omega - \omega_0) + \frac{1}{2}\beta_2(\omega - \omega_0)^2 + \frac{1}{6}\beta_3(\omega - \omega_0)^3 + \ldots, \tag{3.28}$$

where $\beta_n = d^n\beta(\omega)/d\omega^n|_{\omega=\omega_0}$. From 3.28 it is clear how if $\beta_2 \neq 0$ the group velocity will depend on the frequency ω. This frequency dependence leads to pulse broadening simply because the different frequency components of the lightwave will propagate with different velocities and will not arrive simultaneously at the fiber output.

In 3.28, β_1 is equal to the group delay per length unit $\tau_g(\omega)$ at $\omega = \omega_0$. The parameters β_2 and β_3 characterize respectively the chromatic dispersion and the chromatic dispersion slope around the frequency $\omega = \omega_0$.

Generally the dispersion and the dispersion slope are expressed as first and second derivative of the group delay on the wavelength λ:

$$D_\lambda = \left.\frac{d\tau_g(\lambda)}{d\lambda}\right|_{\lambda=\lambda_0} = -\frac{2\pi \cdot c}{\lambda_0^2}\,\beta_2, \tag{3.29}$$

$$S_\lambda = \left.\frac{d^2\tau_g(\lambda)}{d\lambda^2}\right|_{\lambda=\lambda_0} = \left(\frac{2\pi \cdot c}{\lambda_0^2}\right)^2 \beta_3 + \frac{4\pi \cdot c}{\lambda_0^3}\,\beta_2, \tag{3.30}$$

In the case of Standard Single Mode Fibers (SSMF), the dispersion coefficient D is zero at around $\lambda = 1310$nm and increases to 17 ps/(nm·km) at $\lambda = 1550$ nm [1]. The broadening induced by CD is highly impairing and it significantly reduces the performance of an optical communication system. Other types of fibers are specifically designed to reduce the dispersion around $\lambda = 1550$ nm (e.g. Dispersion Shifted Fibers (DSFs) have $D = 0$ at $\lambda = 1550$ nm). However, the presence of dispersion allows for the reduction of the signal degradation caused by nonlinear effects in the fiber.

There are different ways to compensate for the chromatic dispersion both in the optical domain and in the electrical domain after the reception of the signal. In Chapter 5 we will show the use of the DSP for CD compensation.

3.2.3 Polarization Effects

An optical mode corresponds to a specific solution to the wave equations that satisfies the boundary conditions at the core-cladding interface. A fiber in which only one mode can propagate is called single mode fiber (SMF) and the mode is called *foundamental*

mode. This mode is polarized along the **x** axis. The same fiber supports also another mode linearly polarized along the **y** axis. These two orthogonally polarized modes are degenerate and have the same mode index. However, this degenerate condition holds true only in the case of an ideal SMF with perfectly cylindrical core of uniform diameter. This is not realized in commonly used SMFs that show variation of the core shape along the fiber length. Thus, due to these factors, the degeneracy of the orthogonally polarized modes is broken and the fiber acquires *birefringence*, that introduces two different propagation indexes for the two orthogonal modes [1]. The degree of modal birefringence is measured by the absolute value of the difference between the mode indices for the orthogonally polarized fiber modes:

$$B_m = |\bar{n}_x - \bar{n}_y| \tag{3.31}$$

This phenomenon leads to a periodical power exchange between the two orthogonal polarization.

In conventional fibers birefringence is not constant along the fiber but changes randomly. This leads to an arbitrary polarization of the received field at the fiber output.

Moreover, different frequency components of the lightwave acquire different polarization states inducing pulse broadening. This phenomenon is called polarization mode dispersion (PMD) [1] [10]. The mean value of the group delay difference $\Delta\tau_{\mathrm{PMD}}$ induced by PMD in a fiber long L is:

$$\langle \Delta\tau_{\mathrm{PMD}} \rangle = PMD \cdot \sqrt{L} \tag{3.32}$$

where, in good fibers, the parameter PMD-parameter is around $PMD = 0.1$ ps/$\sqrt{\mathrm{km}}$. Since the dependence on the fiber length of the group delay difference goes with the square root of L the PMD effect is generally not very strong even for long distances and with symbol rates of 40 GBt/s.

3.2.4 Optical Amplifiers and ASE Noise

Optical amplification is often necessary to compensate for the fiber losses, particularly in long-haul systems. Most optical amplifiers amplify light through stimulated emission and therefore, as in the case of lasers, are susceptible to the noise created by spontaneous emission (ASE noise). This worsens the OSNR of the signal reducing the performance of the system.

3.3 Optical Receiver

In this chapter we will analyze the most important aspects of an optical receiver. Particular attention is given to Direct Detection receivers since the Coherent Detection is studied separately in Chapter 5.

3.3.1 Optical Receiver Structure

In Figure 3.17 the structure of an optical receiver is shown. It is possible to divide an optical receiver in four stages.

Firstly, the optical signal is filtered by an optical band-pass filter used to limit the noise bandwidth and thus reducing the noise components that fall into the detection bandwidth. The filtered optical signal is then received by the photodetector that transforms it into an electrical signal. Afterwards, the electrical signal is low-pass filtered to reduce the impact of shot noise and thermal noise and the amplifier noise in case of electrical amplifiers after the photodetector. Eventually, the electrical signal is processed by the decision circuit that converts it into the recovered data sequence.

In the following sections we will study deeper the most important components of an optical receiver.

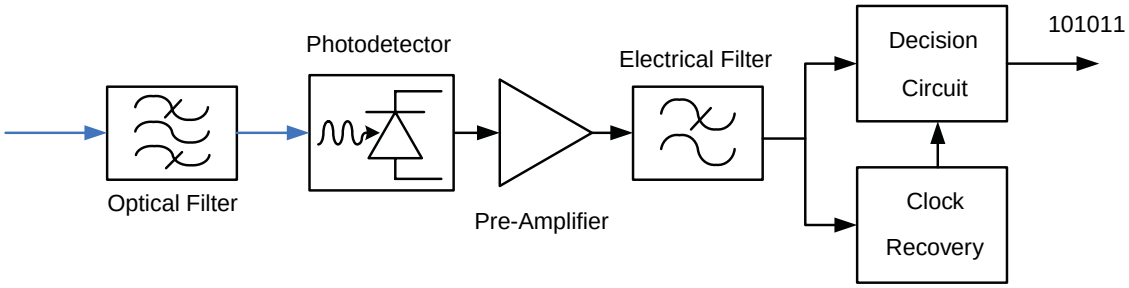

Figure 3.17: Simplified block diagram of a generic direct detection receiver front end and decision circuit. In blue the optical signal, in black the electrical signal.

3.3.2 Photodetectors

The photodiode is the core of an optical receiver. It is an optoelectronic device that transforms the optical signal into an electrical one through the process of optical absorption. As a matter of fact, if we consider a slab of semiconductor hit by an optical

signal, if the energy $h\nu$ of the incident photons exceeds the bandgap energy, an electron-hole pair is released each time a photon is absorbed by the semiconductor. Under the influence of an electric field set up by a bias of the semiconductor, the electrons and holes generated by the optical absorption move across the semiconductor generating electric current [1].

The photocurrent I_p is directly proportional to the incident optical power P_{in}:

$$I_p = RP_{in}, \tag{3.33}$$

where the coefficient of proportionality R is called responsivity of the photodetector.

A simply photodetector is the *p-n* photodiode. In these devices the depletion region created in a reverse-biased *p-n* junction is used to accelerate carriers created with the optical absorption.

In a *p-i-n* photodiode a layer of undoped semiconductor material allows for an enlargement of the depletion region and consequently an increase in responsivity. Moreover, the bandwidth in a *p-i-n* photodiode is considerably improved and can reach 100 GHz in modern devices [1].

Together with the responsivity and the bandwidth, the dark current I_d is a third important parameter in a photodetector. The dark current is the current generated by a photodetector in absence of input optical signal. For good photodiodes the photocurrent is negligible.

We will not analyze deeper the different technologies employed in modern photodetectors and in this project we will assume to use always a simple InGaAs *p-i-n* photodiode. In Table 3.1 the most important specifications of an InGaAs *p-i-n* photodiode are shown.

Table 3.1

Parameter [dBm]	Symbol	Unit	Value
Wavelength	λ	μ m	1.0 - 1.7
Responsivity	R	A/W	0.6 - 0.9
Quantum efficiency	η	%	60-70
Dark current	I_d	nA	1-20
Bandwidth	Δf	GHz	10-100

3.3.3 Receiver Noise

Two fundamental noise mechanisms affects the receiver performance: the shot noise and the thermal noise. In this section we will review these two noise mechanisms and explain how they affects the optical receiver.

3.3.3.1 Shot Noise

The shot noise is a manifestation of the discretization of the electrical carriers. In the photodiode, the electron-holes pairs created by the absorption of photons, are generated at random times [1]. Thus, it is possible to write the photocurrent at the output of the photodiode as:

$$I(t) = I_p + i_s(t), \tag{3.34}$$

where $I_p = RP_{in}$ is the average current and $i_s(t)$ is the random fluctuation due to shot noise. The random contribution i_s has Poisson statistics (that can be approximated with Gaussian statistics in case of high average current I_p).

With this approximation, the noise variance ϕ_s^2 is related to the power spectral density $S_s(f)$ by:

$$\sigma_s^2 = \langle i_s^2(t) \rangle = \int_{-\infty}^{\infty} S_s(f) df, \tag{3.35}$$

and since the shot noise can be consider as white noise with spectral density $S_s(f) = qT_p$ we have that the noise variance becomes:

$$\sigma_s^2 = \langle i_s^2(t) \rangle = 2qI_p \Delta f, \tag{3.36}$$

where Δf is the effective noise bandwidth of the receiver. It generally depends on the receiver design, but it can be approximated with the photodetector bandwidth.

Since the dark current also generates shot noise it should be included in (3.36) by replacing I_p with $I_p + I_d$:

$$\sigma_s^2 = 2q(I_p + I_d)\Delta f, \tag{3.37}$$

3.3.3.2 Thermal Noise

The thermal noise is caused by the thermal motion of electrons in conductors. This phenomenon is reflected in fluctuation of the current through a resistor even in absence of applied voltage [1].

The load resistor in the front end of the optical receiver suffers as well of thermal noise. Thus, we can include a component $i_T(t)$ in the total photodiode current, to represent the fluctuations due to thermal noise:

$$I(t) = I_p + i_s(t) + i_T(t). \tag{3.38}$$

The thermal current fluctuation $i_T(t)$ can be modeled as a stationary Gaussian random process with a spectral density that is frequency independent up to 1 THz and is:

$$S_T(f) = 2k_bT/R_L, \tag{3.39}$$

where k_B is the Boltzmann constant, T is the absolute temperature and R_L is the load resistor. As in the case of shot noise the noise variance of the thermal noise can be obtained by integrating the spectral density over the effective noise bandwidth:

$$\sigma_T^2 = (4k_BT/R_L)\Delta f \tag{3.40}$$

In the derivation made above, we considered as origin of the thermal noise only the load resistor in the receiver front end. However, the actual receiver contains other electrical components (e.g electrical amplifiers) that increase the thermal noise. In order to account for the noise introduced by the rest of the circuitry, we can multiply (3.40) by the amplifier noise figure F_n, that represents the factor with which the thermal noise is enhanced. This yields to:

$$\sigma_T^2 = (4k_BT/R_L)F_n\Delta f \tag{3.41}$$

The total noise variance is therefore given by the sum of the shot noise and thermal noise variances:

$$\sigma^2 = \sigma_s^2 + \sigma_T^2 \tag{3.42}$$

3.3.4 Direct Detection Receivers

In Direct Detection schemes, the signal is detected without the means of a local oscillator but directly detecting the optical signal with a simple photodetector. The block diagram of Figure 3.17 shows the structure of a Direct Detection receiver for intensity modulation. In this type of receiver, the whole information of the received signal complex envelope is lost because the photodiode detects only the intensity of the optical

wave. However, in case of intensity modulation this is not a problem and the signal can be correctly detected anyway.

Nevertheless, in case of phase modulated signals and direct detection, this scheme is not enough and the phase information must be converted into intensity information before detecting the optical signal with a photodiode.

This can be done with a delay line interferometer (DLI). As it is shown in Figure 3.18, a DLI exploits an interferometric structure to make beat the signal phase shifted of ϕ_{DLI} with the signal itself delayed by one symbol duration T_S.

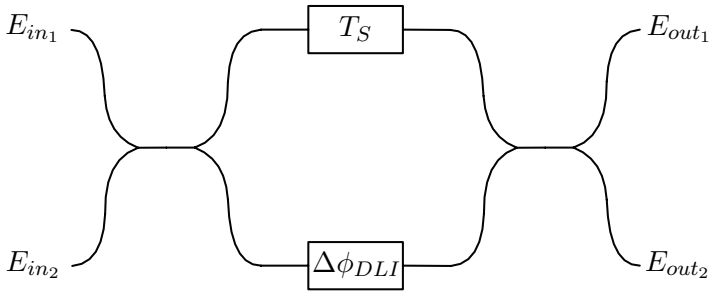

Figure 3.18: Delay line interferometer.

Thus, we can write the relation between the input and output electric fields as:

$$E_{out_1} = \frac{1}{2}E_{in}(t - T_S) - \frac{1}{2}E_{in}(t)e^{-j\phi_{DLI}} \tag{3.43}$$

$$E_{out_2} = j\frac{1}{2}E_{in}(t - T_S) - j\frac{1}{2}E_{in}(t)e^{-j\phi_{DLI}} \tag{3.44}$$

If the input electric field is:

$$E_{in} = \sqrt{P_s(t)} \cdot e^{j\omega_s t + \phi_s} \cdot e^{-j\phi(t)} \cdot e^{-j\phi_{n_s}}, \tag{3.45}$$

and we neglect the phase noise ϕ_{n_s}, we obtain that the optical power at the two DLI outputs is:

$$\begin{aligned} P_{out_1}(t) =& E_{out_1}(t) \cdot E^*_{out_1}(t) = \frac{1}{4}P_s(t) + \frac{1}{4}P_s(t - T_S) \\ & - \frac{1}{2}\sqrt{P_s(t)}\sqrt{P_s(t - T_S)}\cos\left[\Delta\phi(t) + \phi_{DLI}\right], \end{aligned} \tag{3.46}$$

$$\begin{aligned} P_{out_2}(t) =& E_{out_2}(t) \cdot E^*_{out_1}(t) = \frac{1}{4}P_s(t) + \frac{1}{4}P_s(t - T_S) \\ & + \frac{1}{2}\sqrt{P_s(t)}\sqrt{P_s(t - T_S)}\cos\left[\Delta\phi(t) + \phi_{DLI}\right], \end{aligned} \tag{3.47}$$

where $\Delta\phi(t) = \phi(t) - \phi(t - T_S)$ is the phase difference between two consecutive symbols.

It now clear how the information encoded in the phase difference is converted into intensity modulation. This makes a phase modulated signal detectable also by using a simple direct detection scheme. However, it is necessary to differentially encode the signal in order to have the information encoded in the difference of phase between two adjacent symbols and not in the absolute phase.

Without spending more words on the DD receiver for OOK modulation, that basically consists only in a photodiode, let us now see how to perform a direct detection of phase modulated signals.

3.3.4.1 DPSK Receiver

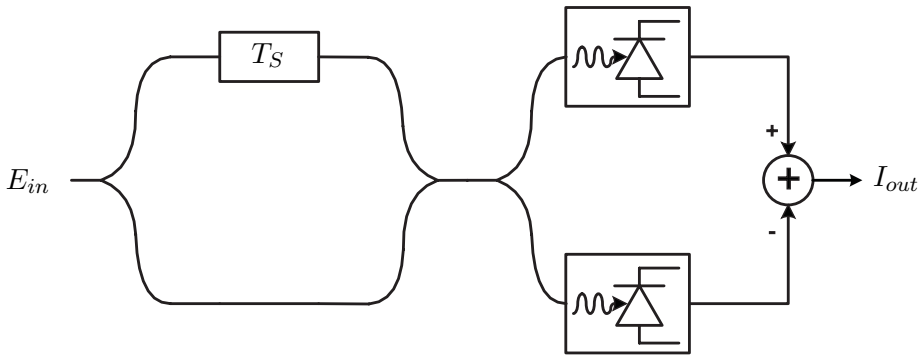

Figure 3.19: Block diagram of the direct detection DBPSK receiver.

For a binary phase modulation it is possible to simply use a DLI with $\phi_{DLI} = 0$ before detecting the optical signal (see Figure 3.19). Thus, the optical power at the two outputs of the DLI is:

$$P_{out_1} = \begin{cases} 0 & \text{if } \Delta\phi = 0 \\ P_s & \text{if } \Delta\phi = \pi \end{cases} , \tag{3.48}$$

$$P_{out_2} = \begin{cases} P_s & \text{if } \Delta\phi = 0 \\ 0 & \text{if } \Delta\phi = \pi \end{cases} . \tag{3.49}$$

Hence, it is possible to directly detect the optical signal at one of the two DLI outputs or employ a balance detector that, exploiting both P_{out_1} and P_{out_2}, improves the receiver performance [5].

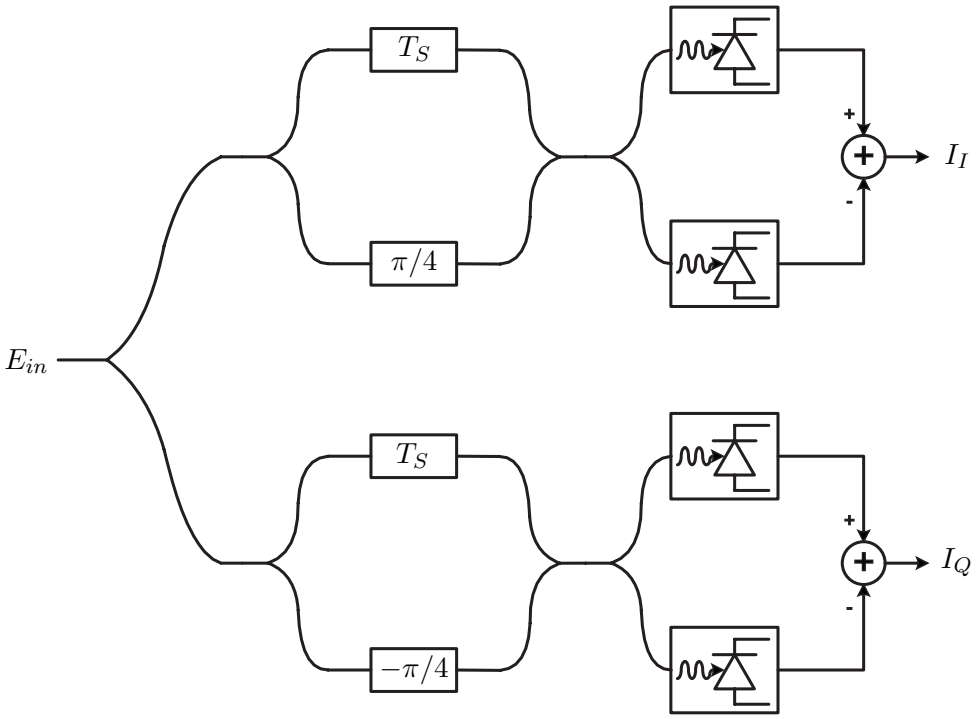

Figure 3.20: Block diagram of the direct detection DQPSK receiver.

3.3.4.2 DQPSK Receiver

In the case of DQPSK the optical signal is fed into two DLIs with respectively $\phi_{DLI_1} = \pi/4$ and $\phi_{DLI_2} = 3\pi/4$ (see Figure 3.20). With this configuration the differential output of the first DLI is:

$$\Delta P_1 = P_{out_1,1} - P_{out_2,1} = \begin{cases} -\frac{1}{\sqrt{2}}P_s & \text{if } \Delta\phi = 0 \\ \frac{1}{\sqrt{2}}P_s & \text{if } \Delta\phi = \frac{\pi}{2} \\ \frac{1}{\sqrt{2}}P_s & \text{if } \Delta\phi = \pi \\ -\frac{1}{\sqrt{2}}P_s & \text{if } \Delta\phi = \frac{3\pi}{2} \end{cases}, \tag{3.50}$$

and the differential output of the second DLI is:

$$\Delta P_2 = P_{out_1,2} - P_{out_2,2} = \begin{cases} -\frac{1}{\sqrt{2}}P_s & \text{if } \Delta\phi = 0 \\ -\frac{1}{\sqrt{2}}P_s & \text{if } \Delta\phi = \frac{\pi}{2} \\ \frac{1}{\sqrt{2}}P_s & \text{if } \Delta\phi = \pi \\ \frac{1}{\sqrt{2}}P_s & \text{if } \Delta\phi = \frac{3\pi}{2} \end{cases}. \tag{3.51}$$

Thus, the output power ΔP_1 contains the information of the in-phase component of the DPSK signal (I) and the output power ΔP_2 contains the information of the quadrature

component (Q) [5].

3.3.5 Decision Circuit

Once the signal has been detected, the photocurrent I_p (it can be more then one in the case of multilevel signals) must be converted to a binary signal. This task is performed by the decision circuit. In the case of binary conversion (e.g. in the receivers for OOK, DPSK and DQPSK) the decision circuit checks the photocurrent once per symbol slot and if I_p results higher than a certain threshold I_{th}, it will assign to it a '1' or otherwise it assigns a '0' (as shown in Figure 3.21). The temporal point at which the decision circuit samples the photocurrent and the threshold current I_p are two variable that depend on the modulation format used and can be adjusted in order to improve the performance of the system.

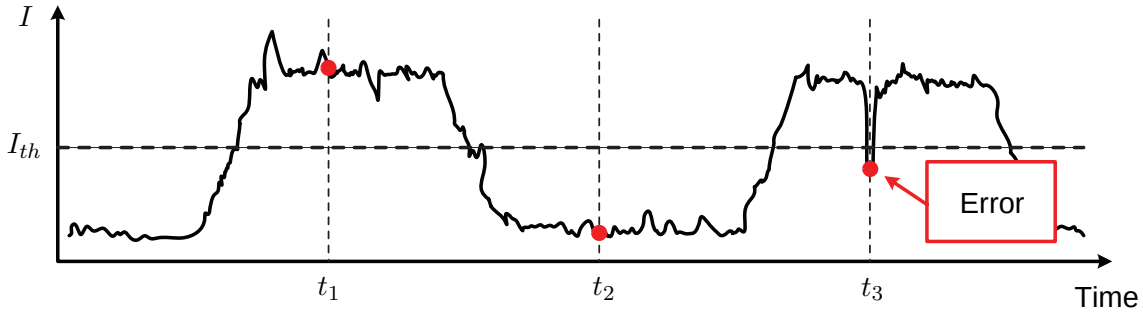

Figure 3.21: Example of decision within a basic decision circuit with single threshold current I_{th}. The photocurrent is sampled at three times, t_1, t_2, and t_3, and an error occurs in the last one.

4

System Model

In this chapter we will treat all the different aspects related to the realization of the optical communication system model developed for this project. This has been written in Matlab® code and even if it does not present all the characteristics and features of more complex commercial softwares, it can be considered a very complete model and, most importantly, it allowed us, during its implementation, to fully understand every single component and function implemented.

The model has been done in collaboration with my friend and colleague Luca Ferrari. Here we will describe the implementation of the most important blocks and operations used in the model. Particular attention is given to the part of the model used for this project.

Most of the operations and functions of the model are directly derived by the system theory described in Chapter 2. These blocks will not be treated here. Instead, in this chapter we will focus on all the elements that required a more complex modeling.

4.1 General Conventions used in the Model

The analysis follows a logical order, presenting first the general conventions and functions used in the model.

4.1.1 Time and Frequency Axis Generation

In order to represent signals in the Matlab® digital domain, it is important to define the time and frequency array to describe a certain moment in time and a specific frequency

in the spectrum. In Figure 4.1 it is possible to understand how this discretization takes place.

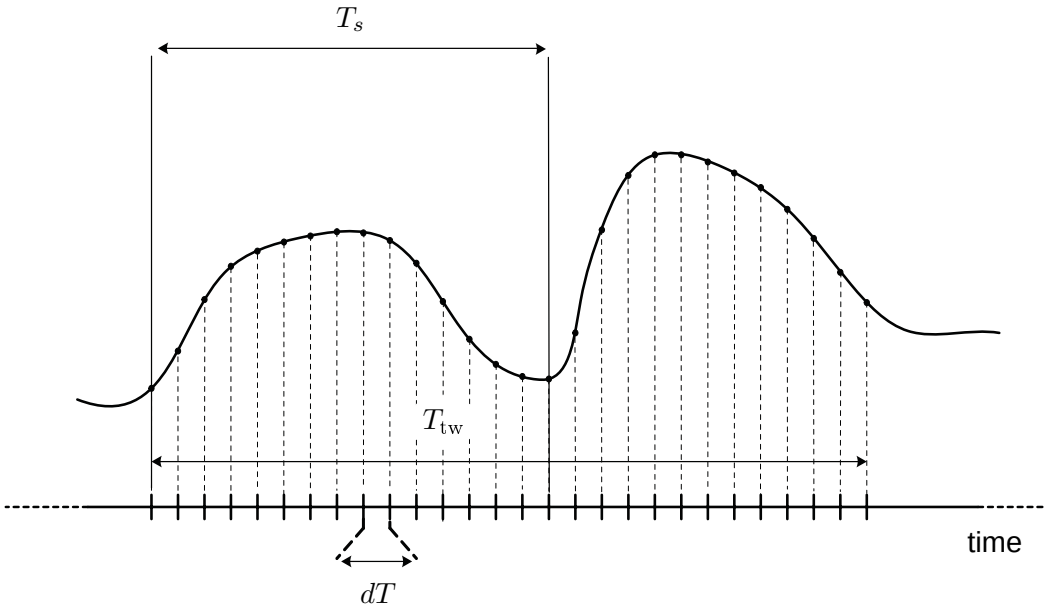

Figure 4.1: Discretization of the time.

The time array is an array of temporal values that describes a time window of duration T_{tw}. The time distance between two adjacent points is dT and therefore a time array with N points will be able to represent only the time instances $k \cdot dT$ with $k \in \{1, \ldots, N\}$.

The generation of the time array is strictly related to the number of symbols we want to represent and the accuracy that we require to represent these symbols.

Knowing that the time array is discrete, the accuracy of the representation of one symbol is given by the amount of time points contained in the symbol time window T_s (`SamplesPerSymbol`). The time interval dT is therefore defined as:

```
dT = 1/(SamplesPerSymbol*SymbolRate)
```

Where the symbol rate (`SymbolRate`) is simply $1/T_S$. Knowing the number of symbol (`Nsymbols`) that we want to represent, the time array will have a number of points N equal to `Nsymbols*SamplesPerSymbol`.

The parameter `SamplesPerSymbol` is generally chosen as power of two. This choice is due to the fact that the Fast Fourier Transform (FFT) algorithm, that allows for

calculating the discrete Fourier transform moving from the time domain to the frequency one, is fastest for a sequence length N that is power of two. Thus, as `Nsymbols` is power of two for the way the signal is generated (as explained in Section 4.1.2,) `SamplesPerSymbol` is also chosen as power of two.

The frequency array is similarly generated. Hoverer, its specifications depend on the parameters used to generate the time array. The length of the array is equal to the time array one. The granularity defined by dF is inversely proportional to the time window defined in the time array ($dF = 1/T_{TW}$), so the resolution is higher for a longer time window. However, since the number of points of the two array is the same, the spam of frequencies contained in the frequency array is also inversely proportional to T_{tw}. In fact, the highest representable frequency is:

$$f_{max} = \frac{1}{2} \cdot N \cdot dF$$

where N is the number of points of the array.

It is important to underline that, in the case the frequency array is used to represent an optical signal, the central frequency of the frequency array ($f_0 = 0$ Hz) must be shifted of $f = f_{ReferenceFrequency}$ in order to have the real optical spectrum (only the positive frequencies). This is due to the way the optical signal is represented in Matlab® (see Section 2.5).

4.1.2 Pseudo-Random Binary Sequence Generation

In order to correctly evaluate the performance of our system, it is of great importance to appropriately choose the bit or symbol sequence to send. In the simulation of optical communication systems, the common choice is to use pseudo-random binary sequences (PRBS) to represent the data.

In a system with binary modulation and memory length of n_b bits, the sequence that allows for the best simulation of the ISI effects, is a sequence that contains all the possible n_b-bit patterns. Let us now see how to obtain and model this kind of bit sequence.

Using a line of n_b shift registers it is possible to obtain a sequence long $2^{n_b} - 1$ that contains all the possible n_b-bit patterns, but the sequence of n_b consecutive zeros. This is generated by loading an initial pattern (called seed) on the n_b registers and then by feeding iteratively into the first register the result of the xor operation between

the output and a register in an appropriate location. The sequence obtained from the output after $2^{n_b} - 1$ iterations is called *maximum length sequence*. In Figure 4.2 the generation of a maximum length sequence of length $2^7 - 1 = 127$ bits is shown. In this case the xor operation is made between the output and the sixth register.

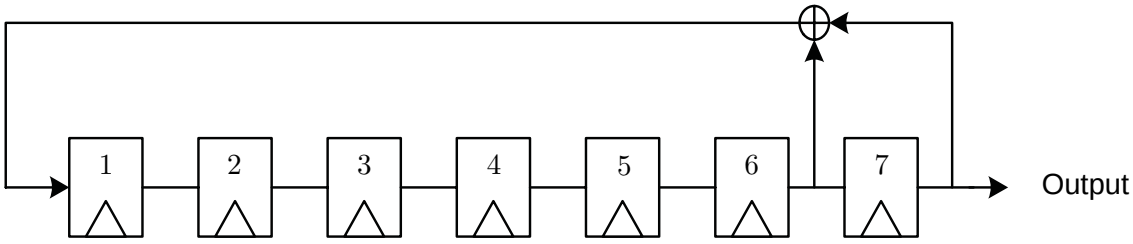

Figure 4.2: Block diagram of shift register scheme used to generate a maximum length sequence with a seed of 7 bits.

In order to obtain the sequence that contains all the n_b-bit patters it is possible to generate a maximum length sequence and add a zero to the longest sequence of consecutive zeros. This kind of pseudo-random binary sequence is called *de Bruijn bit sequence*. In our model, in the case of binary modulation, the PRBS is generated through a de Bruijn bit sequence.

Dealing with multilevel modulation, the ideal bit sequence must contain all the n_s-symbol patterns. Like de Bruijn bit sequences, de Bruijn symbol sequences can be obtained exploiting linear feedback shift registers. However the length of such sequences makes them generally not usable in practice. Indeed, the length of a de Bruijn symbol sequence of m-bit symbols is $m \cdot 2^{m \cdot n_s}$. This means that in the case of 16-QAM the bit sequence length for $n_s = 3$ is 16384 bit and for $n_s = 4$ is 262144. This directly affects the correctness of the simulation of ISI effects since it depends on the length of the seed length n_s, and the shorter it is the less accurate is the simulation [10], [25].

In our model, in the case of multilevel simulations, we decided not to use de Bruijn symbol sequences but m de Bruijn bit sequences multiplexed together. In this way the implementation is simplified. Moreover, due to the differential encoding often used in our system, the advantages related to the use of a de Bruijn sequence would be lost anyway.

In all the Monte Carlo simulations presented in this project, the length of one single bit sequence is kept fix to 512 bits. This is done in order to obtain a good trade-off between speed and accuracy of the simulations.

4.1.3 Electrical Signal Generation

In real systems, the transmitter modulators (both internal and external modulators) are driven by electrical signals generated from the data pattern to transmit. Because of the limited bandwidth of the electric modulators, these signals present rise and fall times different from zero.

In our model the electrical signal rise and fall times are obtained filtering a perfect square signal obtained from the data pattern with a low-pass Gaussian filter with transfer function equal to:

$$H(f) = e^{-\frac{1}{2}\frac{f^2}{(\omega_0/2\pi)^2}}. \tag{4.1}$$

In order to understand how to relate the parameter ω_0 to the rise time t_r of the signal (and so also to the fall time t_f), we could consider that the output of the filter is given by:

$$g(t) = f * h(t) \tag{4.2}$$

where $f(t)$ is the ideal input signal, and it can be written as a step function $f(t) = V \cdot \Theta(t - t_0)$, with V the maximum value assumed by the function.

In (4.2), $h(t)$ is instead the impulse response of the filter, and from (4.1) it can be written as:

$$h(t) = \frac{\omega_0}{\sqrt{2\pi}} e^{-\frac{\omega_0^2 t^2}{2}}. \tag{4.3}$$

Equation (4.2) can thus be solved obtaining:

$$g(t) = \frac{V}{2}\left[2 - \ \mathrm{erfc}\left(\frac{\omega_0}{\sqrt{2}}(t - t_0)\right)\right] \tag{4.4}$$

By definition of rise time, t_r is the time it takes for the signal to increase from 10% to 90% of its maximum value. Therefore, in Figure 4.3, if $g(t_1) = V\frac{1}{10}$ and $g(t_2) = V\frac{9}{10}$, $t_r = t_2 - t_1$.

From these two conditions, we can solve (4.4) and obtain

$$\begin{aligned} t_1 - t_0 &= \frac{\sqrt{2}}{\omega_0}\mathrm{erfc}^{-1}(1.8) \\ t_2 - t_0 &= \frac{\sqrt{2}}{\omega_0}\mathrm{erfc}^{-1}(0.2) \end{aligned} \tag{4.5}$$

that yields to:

$$t_r = t_2 - t_1 = \frac{\sqrt{2} \cdot 1.82}{\omega_0} \tag{4.6}$$

This result made us able to directly use the wanted value of rise and fall time in the model.

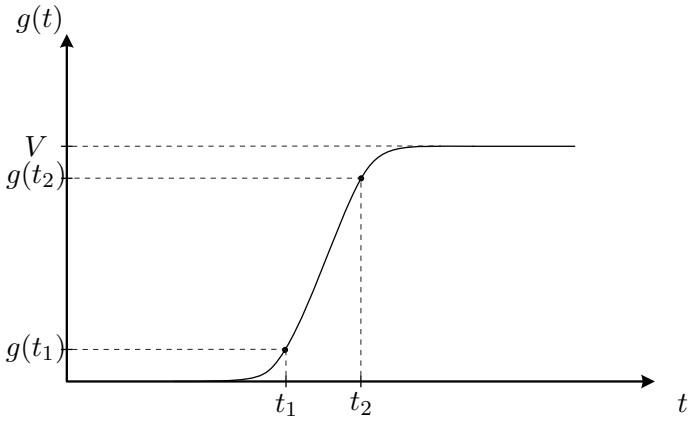

Figure 4.3: Rise time.

4.2 Optical Transmitter

4.2.1 Laser CW

In our Matlab® implementation we stated modeling the ideal lightwave field equation given by (3.1) and adding afterwards the different non-idealities on top of it.

The implementation of the phase noise in Matlab® can be easily done exploiting (3.2), (3.3), and (3.4). In fact, on the ideal equation of the laser lightwave we add the phase noise term `phi_n` as in (3.2). This term is generated from (3.3) as:

```
phi_n = zeros(1, length(TimeArray));
sigma_phase_noise = sqrt(2*pi*linewidth*dT);
phase_noise = random('norm', 0, sigma_phase_noise, [1, length(
    TimeArray)-1]);
for i = 2 : 1 : (length(TimeArray))
  phi_n(i) = phi_n(i-1) + phase_noise(i-1);
end
```

where `sigma_phase_noise` $= \sigma_{\delta_n}$ and the time interval τ is given by the time array granularity `dT`. In the model the intensity noise has been modeled as white Gaussian noise. Again as for the phase noise the Matlab® implementation is fairly simple:

```
sigma_intensity_noise = sqrt(10^(RIN/10))*P;
intensity_noise = random('norm', 0, sigma_intensity_noise, [1,
    length(TimeArray)]);
```

where the `intensity_noise` is added on top of the original laser power.

In our model, for simplicity, we considered the possibility of having the normalized Jones vector $\mathbf{e}_s$ only along the polarization $\mathbf{x}$ or $\mathbf{y}$. Therefore, the final equation, for the $\mathbf{x}$ polarization, that takes into account the two non-idealities is:

```
out.x = sqrt(P+intensity\_noise).*exp(1i*2*pi*(f0 -
    ReferenceFrequency)*TimeArray);
```

4.2.2 OTD PRBS Preserving Multiplexer

The OTD multiplexer modeled in our project allows for the multiplexing of the same signal on the n optical channels of the OTDM system. The implementation of this block is done such that the multiplexing process preserves the PRBS nature of the overall bit sequence. More information about the way this has been modeled in Matlab® are present in [22].

4.3 Optical Channel

4.3.1 Fiber Losses and Second Order Dispersion

In a first implementation of the fiber model only the second order dispersion and the fiber losses were added.

The second order dispersion has been added multiplying the signal in the frequency domain by the chromatic dispersion transfer function in the second order approximation. The losses can be superimposed on the dispersion dividing the result by the accumulated loss after a length L. In the following code lines this simple implementation is shown:

```
N.x = fftshift(fft(in.x));
M.x = N.x.*exp(-1/2*1i*beta2*(2*pi*(FrequencyArray +
    ReferenceFrequency - f0)).^2*L)}
out.x = ifft(ifftshift(M.x))/sqrt(10^(alpha*L/10/1e3));
```

A more complex model, that considers higher order dispersion and fiber nonlinearities, has been developed in [22]. This has been used in some simulations of this project but it will not be presented here because it has not been developed by the author.

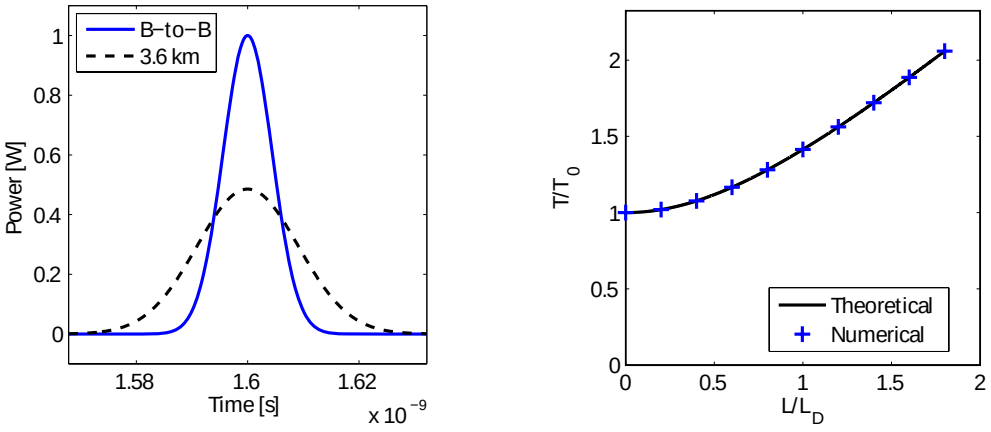

(a) (b)

Figure 4.4: For an unchirped Gaussian pulse, (a) broadening after 3.6 km, (b) comparison of the relative broadening as a function of distance implemented in our model and the analytical results found in [1].

4.3.2 Polarization Rotation

Due to the fiber birefringence, the mode polarization experiences an endless rotation with an angular frequency of ω. This can be modeled by multiplying the lightwave field vector (with the component for the **x** and **y** polarization) by the Jones matrix:

$$\mathbf{J} = \begin{pmatrix} \cos(\omega t + \alpha) & \sin(\omega t + \alpha) \\ -\sin(\omega t + \alpha) & \cos(\omega t + \alpha) \end{pmatrix} \tag{4.7}$$

where the initial angle α is due to an unknown initial state of polarization.

4.4 Optical Receiver

The model used for the optical receiver differs according to whether we employ direct detection o coherent detection. The schemes used for the different DD modulators have been already presented in section 3.3.4 and a deeper analysis of the theory and the model behind the coherent receiver is going to be presented in chapter 5.

In this section we are going to delve into the details of the components used in both structures. First we describe the implementation of optical and electrical filters and then we study the model of a simple PIN photodiode (i.e. the photodetector employed in our project).

4.4.1 Optical and Electrical Filters

Optical and electrical filters are used to reduce the effect of the various sources of noise that affect the signal. The filtering of the signal is performed multiplying it with the transfer function of the filter in the frequency domain. The change of domain, in this case from time to frequency domain, is performed calculating the discrete Fourier transform through the Fast Fourier Transform (FFT) function in Matlab® :

```
X1.x = fft(in.x);
X1.y = fft(in.y);
X2.x = fftshift(X1.x);
X2.y = fftshift(X1.y);
```

The `fftshift` function is used to reorder the array with the zero-frequency component in the center of it.

Optical filters are mainly utilized to reduce the ASE noise introduced by the optical amplifiers used in the system. Optical filters are band-pass filters generally modeled as non-casual Gaussian filters with Gaussian amplitude and real-valued transfer function [10]. The transfer function of such a Gaussian filter of n-th order can be written as:

$$H_G(f) = e^{\frac{(f-f_c)^{2n}}{2(f_0)^{2n}}} \tag{4.8}$$

where f_c is the central frequency of the filter and $f_0 = \frac{B_0}{2(\log 2)^{1/2n}}$ is a parameter that contains the bandwidth B_0 of the filter.

Another type of filter used in the project is the Fabry-Perot (FP) optical filter. FP filters have been modeled utilizing the transfer function given in [3]:

$$H(f) = \frac{1}{\left(1 + \frac{j2f}{B_0}\right)} \tag{4.9}$$

Finally also an OOK-matched filter has been implemented. From the definition of matched filter as the optimal linear filter that maximizes the SNR at its output, the transfer function of a matched filter for a ideal NRZ-OOK signal can be written as:

$$M(f) = \mathrm{sinc}(f \cdot T_S) \tag{4.10}$$

The Matlab® implementation of the frequency responses for the different filter types has been done accordingly with the signal representation given in 2.5. This gives the following frequency responses for the three kinds of filter just described:

```
switch type

    case 'GAUSSIAN'
        f0 = bandwidth/2/log(2)^(1/(2*n));
        frequency_response = exp(-((FrequencyArray +
            ReferenceFrequency - fc).^(n*2))/(2*(f0)^(n*2)));

    case 'FP'
        frequency_response = 1./(1 + 1i*2*(FrequencyArray +
            ReferenceFrequency - fc)/bandwidth);

    case 'MATCHED'
        frequency_response = sinc((FrequencyArray +
            ReferenceFrequency - fc)*SamplesPerSymbol*dT);

end
```

The filtering process is done multiplying the signal in the frequency domain with the selected frequency response and then moving back to the time domain:

```
Y1.x = X2.x.*frequency_response;
Y1.y = X2.y.*frequency_response;
Y2.x = ifftshift(Y1.x);
Y2.y = ifftshift(Y1.y);
out.x = ifft(Y2.x);
out.y = ifft(Y2.y);
```

Electrical filters are used to suppress thermal and shot noise introduced by the photodetector. They are low-pass filters and they are often modeled as Bessel or Butterworth filters.

The transfer function of a Bessel filter is:

$$H_B(s) = \frac{B_n(0)}{B_n(s)}, \tag{4.11}$$

with $B_n(s)$ the Bessel polynomial of order n. Also the Butterworth filters present a transfer function of the type:

$$H_{BW}(s) = \frac{BW_n(0)}{BW_n(s)}, \tag{4.12}$$

where $BW_n(s)$ is the Butterworth polynomial. More details about the implementation of Butterworth and Bessel filters can be found in [26].

The Matlab® implementation of the electrical filters described is the same as the one for the optical filters.

4.4.2 PIN Photodiode

As already explained in section 3.3.1, the photocurrent generated by the PIN photodiode is proportional to the optical power of the received signal (with a constant of proportionality equal to the responsivity R of the photodiode). However, this current is affected by two sources of noise: the shot and thermal noise. In order to model this phenomenon it is possible to add on top of the photocurrent $I_p = RP_{in}$ a variable current generated by a random process with normal distribution and with variance given by (3.42). To simulate the bandwidth of the photodiode the current is filtered by a Gaussian low-pass filter of the 5-th order. The model of the PIN photodiode is thus given by:

```
I1 = R*Power(in);
sigma_noise = sqrt(2*CONSTANT.q*(I1+Id)*delta_f + (4*CONSTANT.
    kb*Temperature/RL)*Fn*delta_f);
noise = random('norm',0, sigma_noise, [1, length(TimeArray)]);
I2 = Electrical_Filter(I1, 'GAUSSIAN', 5, bandwidth);
out = I2 + real(noise);
```

4.4.3 Direct Detection Decision Circuit

In a DD receiver, after the optical signal is detected by the photodiode and transformed in photocurrent, the decision circuit decides whether the received current corresponds to a logical '0' or a '1'. As we already explained in section 3.3.5, the optimal threshold current I_{th} and sampling point used by the decision circuit can differ according to the specifications of the system and the modulation used. An analytical derivation for these parameters cannot be found. Thus, the optimal values are found deterministically testing the system with different values of I_{th} and sampling point.

4.5 Other Blocks

4.5.1 Optical 3dB COupler

The optical 3dB coupler, shown in Figure 4.5, is a block often used in our model. In our implementation, input and output relationship of such a device can be expressed

as:

$$E_{out,1} = \frac{1}{\sqrt{2}} E_{in,1} + -j\frac{1}{\sqrt{2}} E_{in,2},$$
$$E_{out,2} = \frac{1}{\sqrt{2}} E_{in,2} + +j\frac{1}{\sqrt{2}} E_{in,1}. \tag{4.13}$$

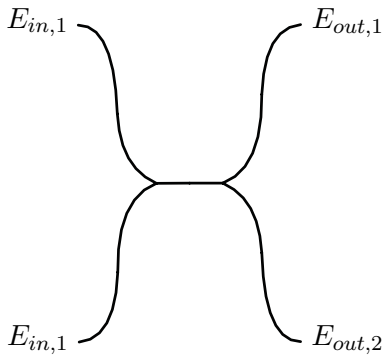

Figure 4.5: Optical 3dB coupler.

4.6 OSNR imposition

As described in section 2.3, the OSNR and the SNR give a reference to the amount of noise present in the system. In order to simulate the noise introduced in the system, it is possible to artificially add a white Gaussian noise on the optical signal that impinges on the optical receiver. This gives the possibility of knowing the value of the actual OSNR. However, this holds true if the noise introduced before the receiver is much stronger than the one introduced in the optical receiver. In the case the system presents strong ASE noise introduced by the optical amplifiers (ASE limited system) this is generally valid.

Thus, in our model we artificially impose a certain white Gaussian noise with noise variance appropriate to obtain the wanted OSNR.

The noise variance of Gaussian process with constant single-sided spectral density N_0 is equal to:

$$\sigma_n^2 = \frac{N_0}{dT}, \tag{4.14}$$

where the factor $1/dT$ represents the baseband frequency span used in the model. Moreover, the noise generated is applied separately to both signal quadratures. Thus,

the noise variance per quadrature is half of the total noise quadrature:

$$\sigma^2_{ASE} = \frac{N_0}{2dT}. \tag{4.15}$$

Then, from (2.2) we can derive the relation between N_0 and the OSNR that gives:

$$N_0 = \frac{\langle P(t) \rangle}{p \cdot \mathrm{OSNR} \cdot B_{ref}}, \tag{4.16}$$

that yields to:

$$\sigma^2_{ASE} = \frac{\langle P(t) \rangle}{2p \cdot dT \cdot \mathrm{OSNR} \cdot B_{ref}}. \tag{4.17}$$

From this, the noise is applied to one polarization in case $p = 1$ or both of them if $p = 2$:

```
switch polarizations
    case 2
        noise.x = random('norm', 0, sigma_noise, [1, Nsamples
            ]) + 1i*random('norm', 0, sigma_noise, [1, Nsamples
            ]);
        noise.y = random('norm', 0, sigma_noise, [1, Nsamples
            ]) + 1i*random('norm', 0, sigma_noise, [1, Nsamples
            ]);
        out.x = in.x + noise.x;
        out.y = in.y + noise.y;
    case 1
        noise.x = random('norm', 0, sigma_noise, [1, Nsamples
            ]) + 1i*random('norm', 0, sigma_noise, [1, Nsamples
            ]);
        out.x = in.x + noise.x;
        out.y = in.y;
end
```

Where `sigma_noise` is σ_{ASE} of equation (4.17).

4.7 Monte Carlo Simulations for BER analysis

In section 2.4, the BER analysis, one of the most important error performance parameters, has been presented. A simple way to perform a BER analysis is to send an input bit sequence through the investigated system, count the bit errors at the received bit sequence and then relate them to the total number of bit transmitted. We call this procedure Monte Carlo (MC) simulation [10].

In our model we perform MC simulations simulating the system with a relatively short symbol sequence (i.e. between 128 and 1024 symbols) and repeating the simulation until the total number of errors counted reaches the initially defined threshold.

The accuracy of the obtained results depends strongly on the total number of errors detected. The higher it is, the better is the accuracy of the BER value obtained. In our model the error counting is done separately for each bit of a symbol and on each polarization (e.g. on a 16QAM-PolMux the bit comparison is done separately on b_1, b_2, b_3 and b_4 of both $\mathbf{x}$ and $\mathbf{y}$ polarization). We then impose a threshold for the error counted on each bit sequence (this threshold is generally of 100 errors). Finally, the monte carlo simulation is stopped when all the bit sequences have overtaken the given threshold. In this way we make sure that the accuracy of the BER analysis is high for each bit sequence.

4.8 Validation of the Model

In order to validate the model used in our project we compared the results obtained with different system specifications with the ones found in literature.

With started with the comparison with [2] that provided different simulations of an OOK system with different optical and electrical filters. In Figure 4.6 the four comparisons between the results obtained with our model and those obtain in [2] are shown. The simulations have been made with a NRZ-OOK at 10 Gb/s, the ASE noise has been imposed on one polarization and the filters specifications are: matched optical filter and no electrical filter (Figure 4.6(a)), Gaussian optical filter of first order with bandwidth $= 8 \cdot R_S$ and Gaussian electrical filter of first order with bandwidth $= 0.7 \cdot R_S$ (Firgure 4.6(b)), Gaussian optical filter of first order with bandwidth $= 8 \cdot R_S$ and RC electrical filter with bandwidth $= 0.7 \cdot R_S$ (Figure 4.6(c)), and Gaussian optical filter of first order with bandwidth $= 8 \cdot R_S$ and Butterworth electrical filter of second order with bandwidth $= 0.7 \cdot R_S$ (Figure 4.6(d)). The rise and fall time for the electrical signal have been kept at 0 s.

The most important among these results is shown in Figure 4.6(a) where the BER versus OSNR curve for a OOK system with match filter (quantum limit curve) is presented. The two curves show an almost perfect overlap. This validation is very important and confirms the solidity of our model.

The other three plots in Figure 4.6 show the results obtained with an OOK system and different types of optical and electrical filters. It is possible to notice how the overlap is again almost perfect for Figure 4.6(b), but in the case of Figure 4.6(c) and 4.6(d) the results provided by our model are slightly better (around 1 dB at BER = 10^{-3}). It is not clear from [2] how the author optimizes the threshold current and the sampling point in the DD decision circuit and this might be a source of discrepancies. However, the reason for such a difference in the two curves has not been fully understood.

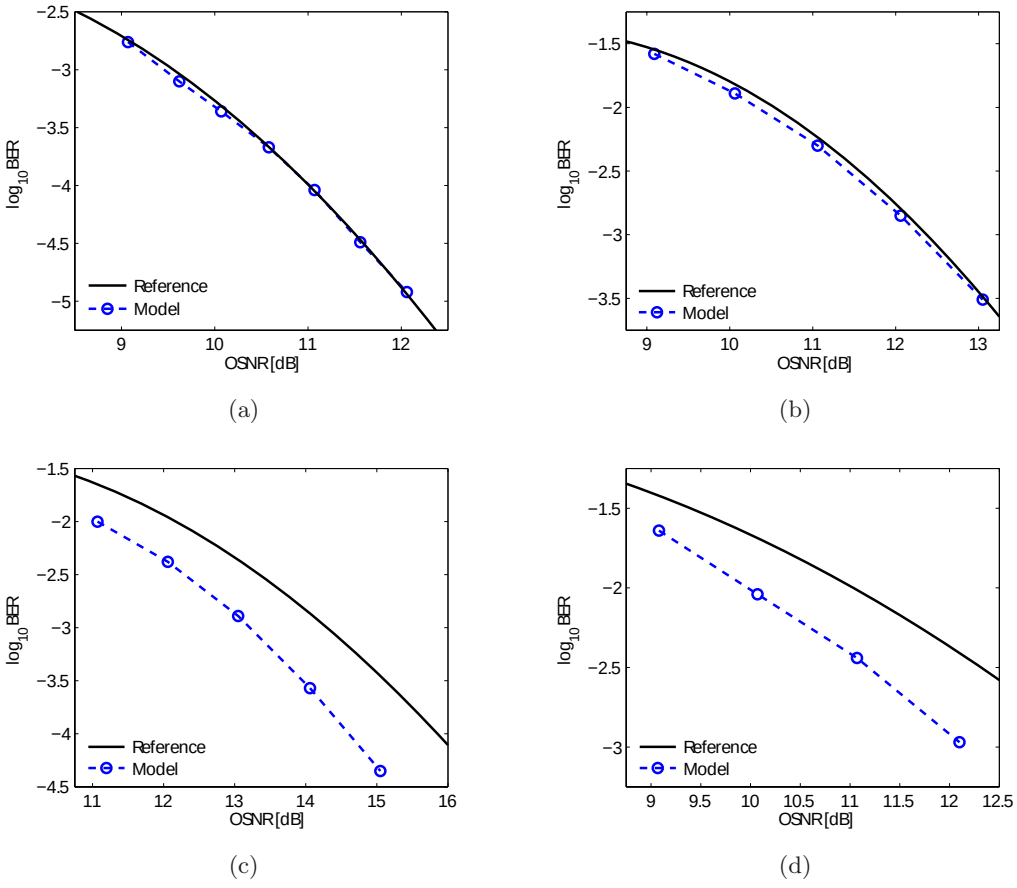

Figure 4.6: BER versus OSNR curves with the comparison of the results obtained with our model and the once of [2]. The simulations compare OOK systems with different optical and electrical filters: (a) Matched optical filter and no electrical filter (b) Gaussian optical filter with $B_o = 8 \cdot R_S$ and Gaussian electrical filter with $B_e = 0.7 \cdot R_S$, (c) Gaussian optical filter with $B_o = 8 \cdot R_S$ and RC electrical filter with $B_e = 0.7 \cdot R_S$ and (d) Gaussian optical filter with $B_e = 8 \cdot R_S$ and Butterworth electrical filter with $B_e = 0.7 \cdot R_S$.

The second comparison has been made with [3] and the simulatiosn for both a DPSK and a DQPSK system are shown in Figure 4.7. The simulations have been made with a NRZ-DPSK at 10 Gb/s (Figure 4.7(a)), and a NRZ-DQPSK at 10 Gb/s (Figure 4.7(b)) and the ASE noise has been imposed on two polarizations. The filters specifications are: FP optical filters with bandwidth $= 3.2 \cdot R_S$ and Bessel electrical filters of 5-th order with bandwidth $= 0.55 \cdot R_S$. The rise and fall time used is again 0 s. As it can be seen, the results obtained overlap perfectly in both simulations.

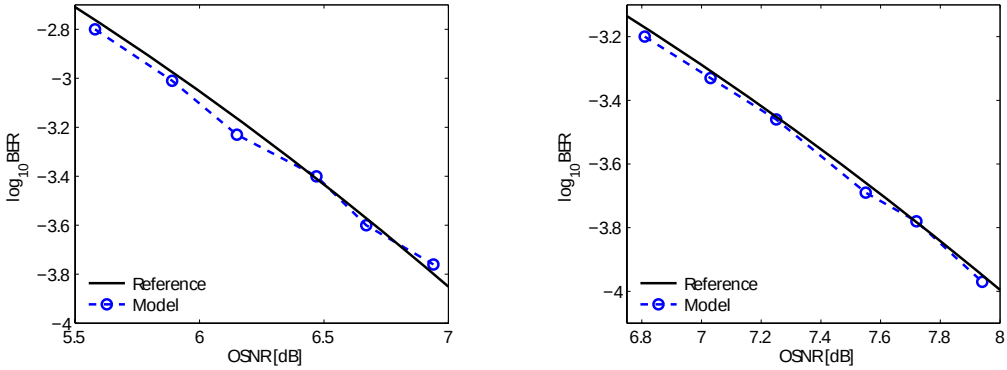

Figure 4.7: BER versus OSNR curves with the comparison of the results obtained with our model and the once of [3] for (a) a NRZ-DPSK at 10 Gb/s and (b) a NRZ-DQPSK at 10 Gb/s.

The results for DPSK and DQPSK modulations have been also verified with [4]. The simulations have been made with (Figure 4.8(a)) a NRZ-DPSK at 40 Gb/s and (Figure 4.8(b) a NRZ-DQPSK at 40 Gb/s and the ASE noise has been imposed on two polarizations. The filters specifications are: Gaussian optical filters of first order with bandwidth $= 2.2 \cdot R_S$ and Butterworth electrical filters of 3-rd order with bandwidth $= 0.7 \cdot R_S$. In this comparison the rise and fall time has been set to $0.44 \cdot T_S$ as in [4]. As it can be noticed from Figure 4.8, the results for the DQPSK modulation overlap. On the other hand, the BER curve for the results obtained with DPSK modulation presents a penalty of 0.4 dB at $BER = 10^{-3}$. Both the simulations have been made with the same specifications used in [4] and the reason for a penalty in the DPSK system is not clear.

Overall, the validation of our model can be considered successful.

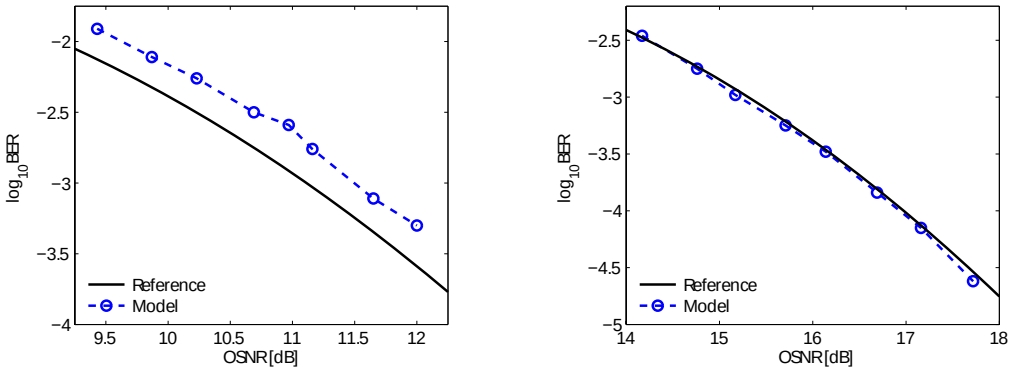

Figure 4.8: BER versus OSNR curves with the comparison of the results obtained with our model and the once of [4] for (a) a NRZ-DPSK at 40 Gb/s and (b) a NRZ-DQPSK at 40 Gb/s.

5

Coherent Receiver with Digital Signal Processing

The employment of coherent receivers in optical communication systems started to be popular in the 80s. Due to scarcity of efficient optical amplifiers, coherent systems were exploited particularly for the opportunity of improving the receiver sensitivity by up to 20 dB. However, after the advent of Erbium Doped Fiber Amplifier (EDFA), the popularity of coherent receivers faded away because of their high complexity. Nowadays, the use of coherent systems is again at the center of attention due to the increasing employment of higher complexity modulation formats for higher spectral efficiency. As a matter of fact, through coherent receivers it is possible to retrieve the whole complex field of the received lightwave and so employ modulation formats that use all the information of the optical signal wave (e.g. amplitude, frequency, phase and polarization).

The main obstacles for the practical implementation of traditional coherent receivers are polarization and phase tracking. Due to the fiber birefringence, the output State of Polarization (SOP) in the fiber fluctuates without matching the SOP of the Local Oscillator (LO). Dynamic control of the SOP is therefore necessary. Its implementation is bulky and expensive and requires a separate control for each WDM channel. Phase locking is also needed, increasing even more the complexity of the receiver. The use of OPLL is practically not feasible due to the complexity and the stringent requirements in the laser linewidth.

Conversely, electrical Digital Signal Processing (DSP) circuits are becoming faster

and faster and provide a simple solution to estimate the carrier phase without using a OPLL. Moreover, its use allows also for digital compensation of fiber-optic transmission impairments (e.g. Chromatic Dispersion or Polarization Mode Dispersion).

The main drawback of DSP schemes is related to the limit on the speed of the electronic circuits that process the received signal. This difficulty inherent on the digital coherent receiver can be overcome by parallelizing the digital processing in the receiver. This parallelization perfectly coexists with the use of time-division multiplexing techniques.

In this chapter we report the implementation of a coherent receiver that employs DSP for demultiplexing and processing of OTDM signals employing high-order modulation formats. As shown in Figure 5.1, the received optical signal is processed differently in the case it is OTDM encoded or not. If it is, the signal is firstly demultiplexed in the different OTDM channels and then these channels are fed into their respective DSP units. Otherwise, the optical signal is directly processed by one single DSP.

In our analysis, we start giving a small introduction about coherent detection and then we move to a more detailed description of a coherent receiver with digital signal processing. In order, we will present the front-end stage and the Analog-to-Digital conversion and the DSP unit with the different algorithms used to process and decode the signal. Finally, we extend the model for the employment of Optical Time Division Multiplexed signal.

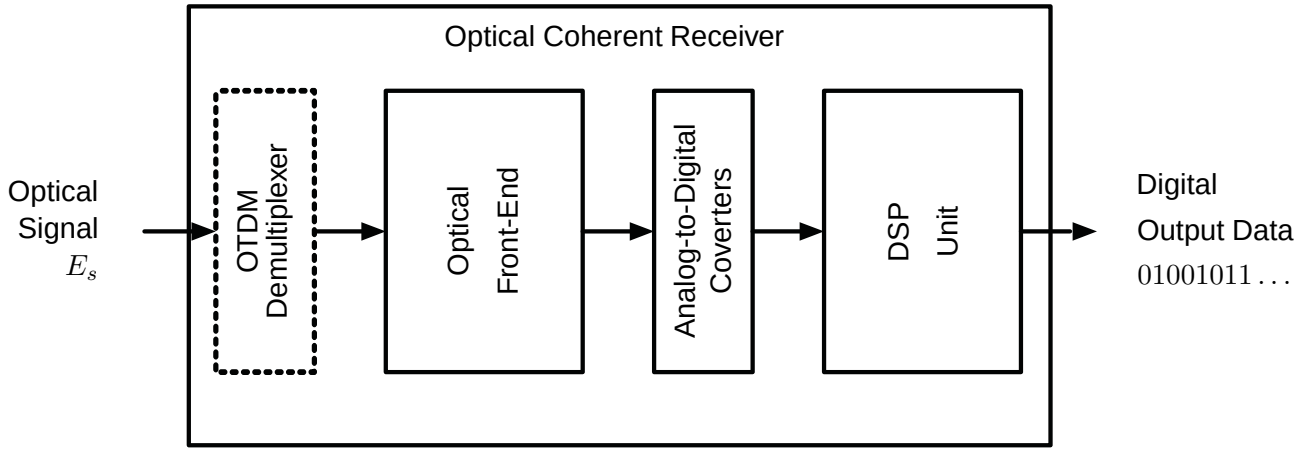

Figure 5.1: Block diagram of the optical coherent receiver with digital signal processing.

5.1 Basic Concepts of Coherent Detection

The basic idea behind coherent communication is to combine the received signal field coherently with another field generated by the so called Local Oscillator (LO) [1].

In order to understand how the two fields mix together and how this affects the performance of the system, let us first write the field of the received signal as:

$$E_s(t) = \sqrt{P_s(t)} \cdot e^{-j(\omega_0 t + \phi_{0_s})} \cdot e^{-j(\phi_s(t) + \phi_{n_s}(t))} \cdot \mathbf{e}_s \tag{5.1}$$

where P_s is the signal power, ω_0 is the carrier frequency, ϕ_{0_s} is the initial phase of the signal, ϕ_s is the signal phase modulation and ϕ_{n_s} is the phase component due to the phase noise on the signal laser. Equally, the LO field can be written as:

$$E_{LO} = \sqrt{P_{LO}} \cdot e^{-j(\omega_{LO} t + \phi_{0_{LO}})} \cdot e^{-j(\phi_{n_{LO}}(t))} \cdot \mathbf{e}_{LO} \tag{5.2}$$

where P_{LO}, ω_{LO}, $\phi_{0_{LO}}$, $\phi_{n_{LO}}$ are the power, the angular optical frequency, the initial phase, and the phase noise of the local oscillator.

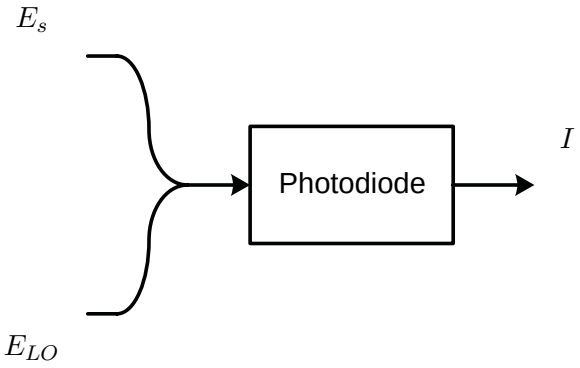

Figure 5.2: Block diagram of a simple coherent detection scheme.

As shown in Figure 5.2, a photodiode detects the beat between the signal field E_s and the LO field E_{LO}. Since the photocurrent I is proportional to the power of the received field (i.e. the power of $E_s + E_{LO}$), we can write from (5.1) and (5.2) :

$$I(t) = RP_s(t) + RP_{LO} + 2R\sqrt{P_s(t)P_{LO}} \cos\left(\Delta\omega t + \phi_0 + \phi_n(t) + \phi_s(t)\right) \cdot \mathbf{e}_s \cdot \mathbf{e}_{LO}, \tag{5.3}$$

where R is the photodiode responsivity, $\Delta\omega = \omega_0 - \omega_{LO}$ is the frequency offset between the local oscillator laser and the signal one, $\phi_0 = \phi_{0_s} - \phi_{0_{LO}}$ is the difference between the initial phases and $\phi_n = \phi_{n_s} - \phi_{n_{LO}}$ is the difference between the phase noise

introduced by the signal and the local oscillator. The frequency $f_{IF} = \Delta\omega/2\pi$ is called intermediate frequency. Let us now suppose that the power of the local oscillator P_{LO} is much higher than the signal one since in real systems P_{LO} is around 20 dB higher than the received P_s. In this way, the term RP_s can be neglected. However, In the case the receiver exploits balanced detection both RP_s and P_{LO} disappear anyway leaving only the beating terms in (5.3). Through this simplifications it is possible to write the photocurrent as:

$$I(t) = 2R\sqrt{P_s(t)P_{LO}}\cos\left(\Delta\omega t + \phi_0 + \phi_n(t) + \phi_s(t)\right) \cdot \mathbf{e}_s \cdot \mathbf{e}_{LO}, \tag{5.4}$$

We can now distinguish between two types of coherent detection techniques: *homodyne* and *heterodyne*.

For homodyne detection, the local oscillator frequency ω_{LO} is set to coincide with the signal-carrier frequency ω_0 so that $\Delta\omega = 0$ and the optical spectrum is directly converted to base band. One of the main challenges for homodyne receivers is the implementation of carrier synchronization that lock frequencies and phases of the local oscillator to the signal laser ones.

In the case of heterodyne detection the local oscillator frequency is chosen to be different from the signal one and therefore $\Delta\omega \neq 0$. For heterodyne detection, the intermediate frequency f_{IF} must be higher than the baseband bandwidth of the modulated signal. One advantage of heterodyne detection is that the demodulation scheme and the synchronization with the signal is easier than in the homodyne case. Conversely, due to lower spectral efficiency and practical feasibility at high bit rates, heterodyne detection is generally not considered as possible solution for the implementation of a optical coherent receiver. Thus, in our project we consider only coherent receivers that make use of homodyne detection.

In order to decode the information present in the signal (generally encoded in the power P_s and in the phase ϕ_s) it is important to efficiently control the parameters $\Delta\omega$ ϕ_0, ϕ_n. $\phi_0 \neq 0$ leads to an initial rotation of the constellation, and a combination of the phase noise ϕ_n and a frequency offset $\Delta\omega \neq 0$ leads to a time dependent rotation of the constellation in arbitrary directions. Hence, in order to detect the signal correctly, these effects must be compensated. One way to do this is to exploit an Optical Phase Lock Loop to lock the local oscillator frequency and phase with the signal one [27].

However, an OPLL is not feasible in practice due to its complexity and the stringent requirements in the laser linewidth.

Hence, it is preferable to exploit DSP circuits to process the signal and estimate the carrier phase without using OPLL.

From (5.4) it is also evident how the polarizations of the local oscillator and the signal must match in order to have the optimal photocurrent. However, the availability of the polarization information can be also exploited to increase the degrees of freedom of the system. For instance, it is possible to transmit two signals, one on one polarization and one in the orthogonal one[1] doubling in this way the spectral efficiency of any modulation format.

5.2 Front-end and Analog-to-Digital Conversion

In order to be able to retrieve the information encoded in both the real and imaginary part of the signal electric field (in-phase and quadrature components), a phase and polarization diversity optical quadrature front-end must be employed [10].

As shown in Figure 5.3 the **x** and **y** polarizations of signal and LO are firstly split through a Polarization Beam Splitter (PBS). The LO is polarized at 45° in order to have equal intensity on the **x** and **y** polarizations. The signals E_{sx}, E_{LOx} and E_{sy}, E_{LOy} are then respectively superimposed in two 2x4 90° optical hybrids.

The 2x4 90° optical hybrid is a key element in a coherent receiver and it allows for the detection of the in-phase and quadrature component. In Figure 5.4 a possible implementation of an optical hybrid is shown.

Four couplers and one phase shifter of $\pi/2$ are used to combine the two inputs $E_{in,1}$ and $E_{in,2}$. If we use the transfer function for an optical coupler (4.13), omitting the power attenuation given by the couplers, we obtain the transfer function for the optical hybrid:

[1] orthogonally-polarized lightwaves do not interfere with each other

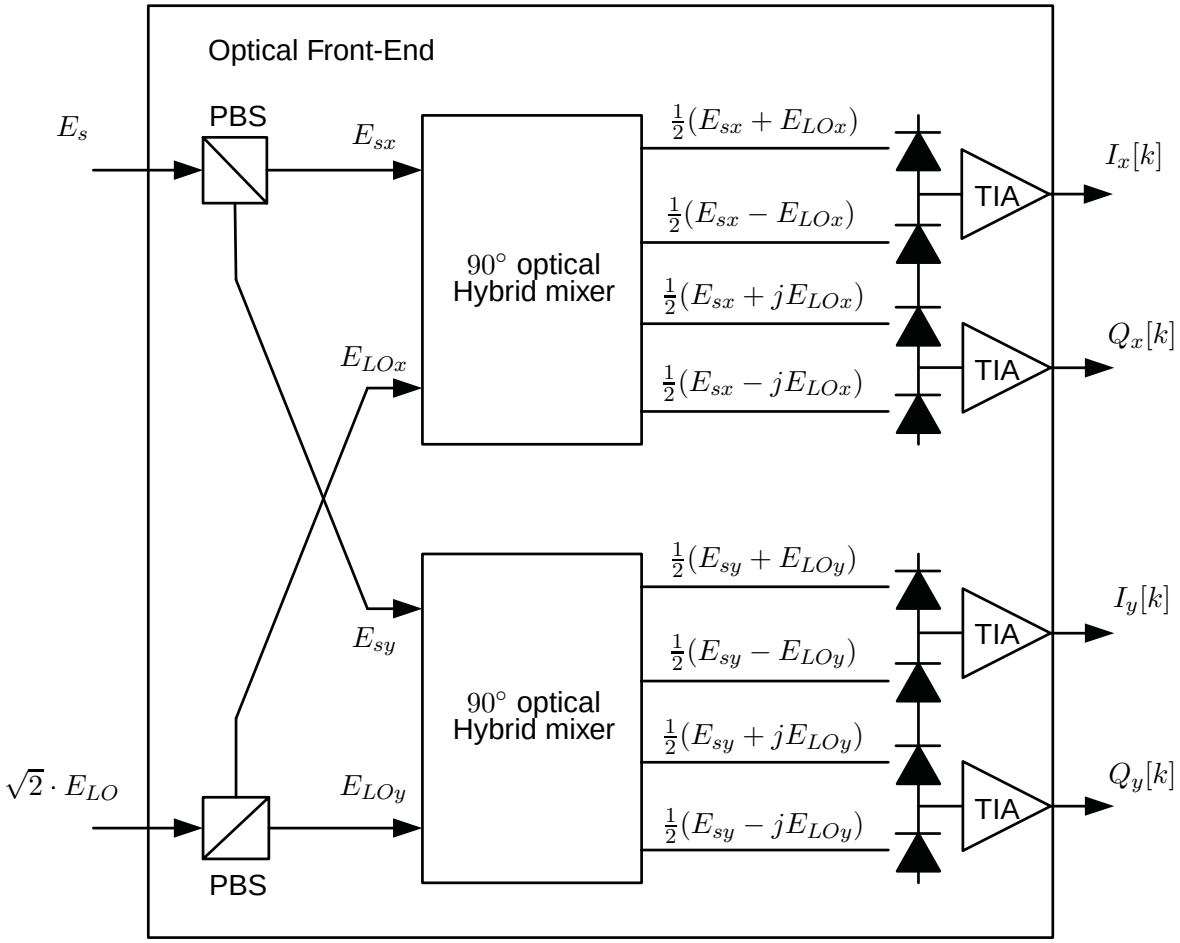

Figure 5.3: Phase and polarization diversity optical quadrature front-end.

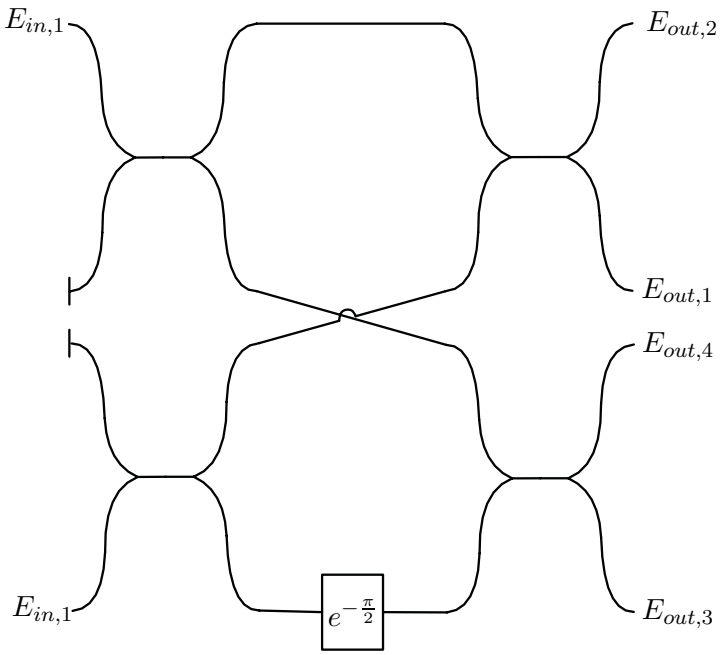

Figure 5.4: 90° Optical hybrid.

$$
\begin{aligned}
E_{out,1}(t) &= Ein,1(t) + E_{in,2}(t),\\
E_{out,2}(t) &= Ein,1(t) - E_{in,2}(t),\\
E_{out,3}(t) &= Ein,1(t) + jE_{in,2}(t),\\
E_{out,4}(t) &= Ein,1(t) - jE_{in,2}(t).
\end{aligned}
\tag{5.5}
$$

If we then feed the received signal and the LO into the two inputs of the optical hybrid E_{in_1} and E_{in_2} as

$$E_{in_1}(t) = E_s(t), E_{in_2}(t) = E_{LO}(t), \tag{5.6}$$

then the output ports of the optical hybrid will have the following combination of the received signal and local oscillator fields:

$$
\begin{aligned}
E_{out,1}(t) &= E_s(t) + E_{LO}(t),\\
E_{out,2}(t) &= Es(t) - E_{LO}(t),\\
E_{out,3}(t) &= Es(t) + jE_{LO}(t),\\
E_{out,4}(t) &= Es(t) - jE_{LO}(t).
\end{aligned} \tag{5.7}
$$

It can be noticed how the output terms $E_{out_1}(t)$ and $E_{out_3}(t)$ in equation (5.7) represent the in-phase and quadrature component of the beating between the signal and the LO. The remaining terms $E_{out_2}(t)$ and $E_{out_4}(t)$ can be used to employ balance detection [28].

The eight outputs of the two optical hybrids are then used as inputs of four balance detectors, obtaining the information of the in-phase and quadrature components in the **x** and **y** polarizations $(I_x[k], Q_x[k], I_y[k], Q_y[k])$.

These photocurrents are then electrically filtered by four Low-Lass (LP) filters. The filter used in our model is (unless differently specified) a Bessel filter of 3rd order. The design of LP filters bandwidth will be specified in the Chapter 6 according to the different systems and modulation formats used. It is important to notice how this filtering process introduces a delay, according to the type and order of the filter used. In our model we decided to compensate these delays in order to be able to confront more easily input and output signals. The delay is calculated using the cross-correlation between the input and output signal.

Afterwards the analog signals are digitally converted by ADCs. The Matlab ® implementation of the ADC block is made focusing on the trade-off between the reliability of the model, computational speed, and ease of use. The reliability of the model is mainly due to the fact that in Matlab ® the signals are always discrete. In order to represent the analog signal, input of the ADC, we introduce a stage of interpolation that, for our purpose, make the digital signal close enough to an analog one. However, the interpolation process introduces an high computational workload so we limited the oversampling rate (i.e. the ratio between the samples we have after and before the interpolation) to 10. After the interpolation stage, the signal is in order: filtered by an anti-aliasing filter, sampled and finally quantized. The anti-aliasing filter is simply a LP filter at half the frequency of the sampling frequency. Again, the design of this filter

is not trivial. In Figure 5.5 the impact of different choices in the ADC anti-aliasing filter design is shown.

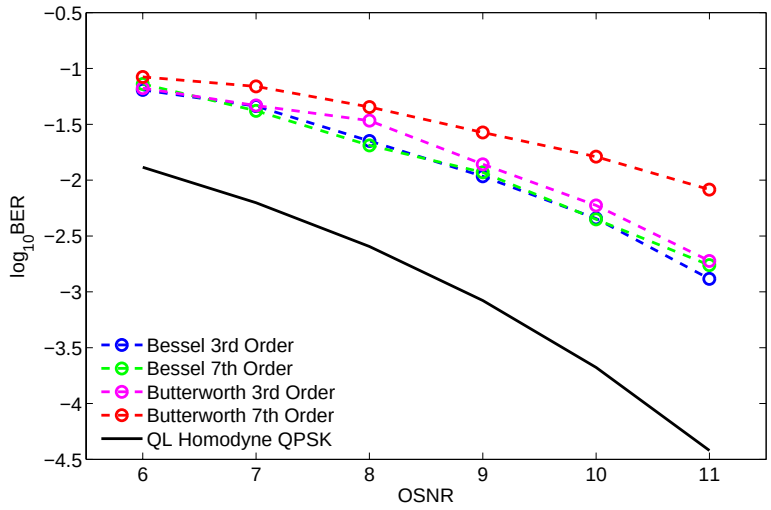

Figure 5.5: BER versus OSNR curves for different type of anti-aliasing filters in the front-end ADC. The signal used is NRZ 10-GBt/s PolMux-DQPSK

For simplicity, we decided to use a unique type of anti-aliasing filter for all the different front-ends used in our model. After a short investigation, based on the BER versus OSNR performance of the system with different types of anti-aliasing filters and different modulation formats, an anti-aliasing filter based on a Bessel LP filter of 3rd order has been chosen. The delay introduced by the filter is again compensated as done before with other filters in the model. After passing through the anti-aliasing stage the signal is sampled and afterwards quantized. In the ADC implemented in our model, the sampling process is uniform and thus the samples are all equally spaced. This means that, if the sampling frequency is F, the sampling slot is $T = 1/F$ and the samples are taken at $t = t_0 + k \cdot T$ with $k = (0, 1, 2, 3, \dots)$. The initial sampling point t_0 assumes random values in $0 \leq t_0 \leq T$ in the case the transmitter and receiver clocks are not phase locked. Otherwise, t_0 can be chosen in order to sample the signal in the optimum point (see Figure 5.6). Finally, the quantization process converts the signal with an infinite resolution to a n-bit resolution signal (e.g. in our model the default resolution is $n = 12$).

In order to recover all the information encoded in the signal, the sampling frequency

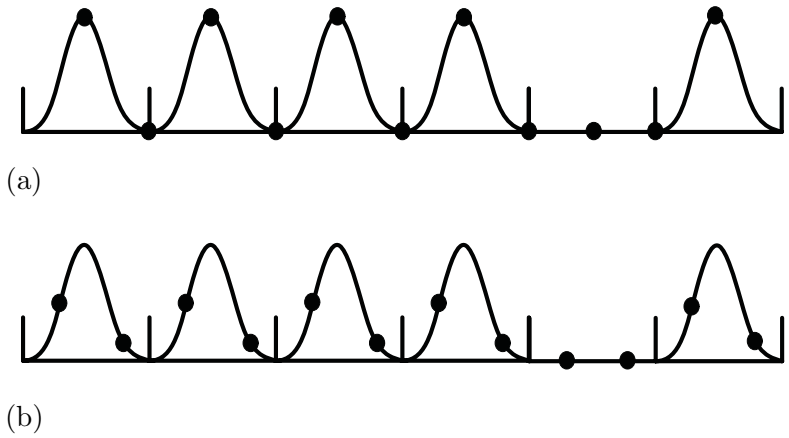

Figure 5.6: Different sampling instants used by the ADC. (a) The samples are taken in the optimal instants. (b) A suboptimal sampling can lead to a decrease in the eye-opening, diminishing the performance.

of the ADCs should be at least equal to the symbol rate of the system. In systems that do not uses a clock recovery stage before the Analog-to-Digital conversion, the sampling frequency of the ADCs is generally double the symbol rate. This allows for a time recovery in the digital domain used to correct the timing phase and frequency offset between the transmitter and receiver clocks. In the case the clock is recovered and synchronized before the digital conversion, the ADCs can use the recovered clock to sample the signal with sampling frequency equal to the symbol rate. In real systems that employ OTDM signal a clock recovery stage before the AD conversion is required. Hence, in our model we hypothesize a clock recovery stage that anticipates the Analog-to-Digital conversion. Despite the timing recovery stage is not needed, the ADCs sampling frequency is kept at twice as much (or more) the symbol rate. This choice is due to the fact that the performance of the algorithms for CD and PMD compensation depends on the amount of samples used to describe each symbol.

Since we hypothesize that the clock is recovered before the AD conversion, the samples can be taken in the optimal instants (see Figure 5.6).

5.3 Digital Signal Processing Algorithms

In Figure 5.7 the structure of the DSP stage is shown. The inputs $\mathbf{p}_x[k] = I_x[k] + jQ_x[k]$ and $\mathbf{p}_y[k] = I_y[k] + jQ_y[k]$ of the DSP unit are in order processed by the

Chromatic Dispersion (CD) compensating block, the Polarization Mode Dispersion (PMD) compensating block, the digital phase estimation block, and the data recovery circuit. In the following sections we will analyze in detail the algorithms used by these processing units.

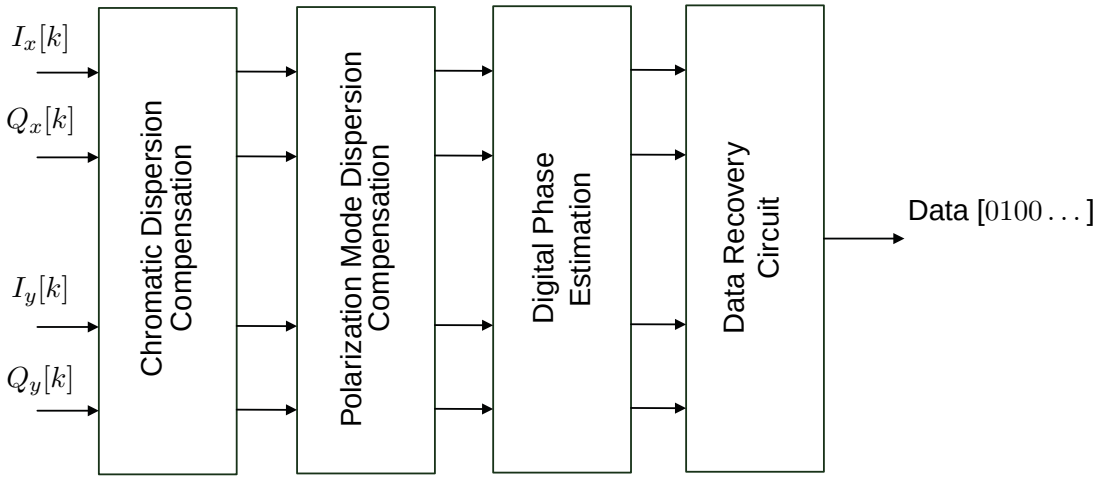

Figure 5.7: Digital Signal Processing unit.

5.3.1 Chromatic Dispersion Compensating Block

As already explained in Chapter 4, the chromatic dispersion is one of the most impairing phenomena that affects a signal transmitted through an optical fiber. Therefore, in order to improve the performance of an optical communication system we need to provide CD compensation. There are different ways to compensate for the chromatic dispersion: we can either do it in the optical domain or process the signal in the digital domain in the case we use a DSP unit with coherent detection. In this section we analyze the different methods to compensate for CD through digital signal processing.

The two method mostly used both utilize a non-adaptive filter. A distinction between the two is in which domain they filter the signal. The Time Domain Equalizer (TDE) directly filters it in the time domain. The Frequency Domain Equalizer (FDE) firstly transfers the signal in the frequency domain, then it filters it and at last transfers the result back to the time domain. The choice between TDE and FDE mainly depends on the maximum dispersion in the channel and the resulting filter length [8]. Generally, the complexity of a FDE filter grows much slower with the amount of CD to

compensate in spite of their non trivial design. Second, both TDE and FDE algorithms can work blindly (i.e. without having information about the length and the dispersion of the fiber) or knowing a priori the amount of chromatic dispersion to compensate (data-aided). In the following, we analyze the data-aided estimation with both TDE and FDE.

In both cases, in order to reconstruct the signal, it is necessary to understand how it has been distorted during its propagation along the fiber. As already shown in Chapter 4, the chromatic dispersion transfer function can be expressed, in the case of second order approximation, as:

$$G(\omega, l) = \exp\left(-jD\frac{\lambda^2}{2\pi c}\frac{\omega^2}{2}l\right). \tag{5.8}$$

The dispersion compensating filter is thus an all pass filter with transfer function $W_c(\omega, l) = 1/G(\omega, l)$.

In the case of frequency-domain equalization (as shown in Figure 5.8(a)), the signal is multiplied in the frequency domain by $W_c(\omega, l)$. This can be done using both a recursive or non-recursive filter. However, in both cases, the filter design is often not trivial and the exact transfer function cannot be always obtained [9].

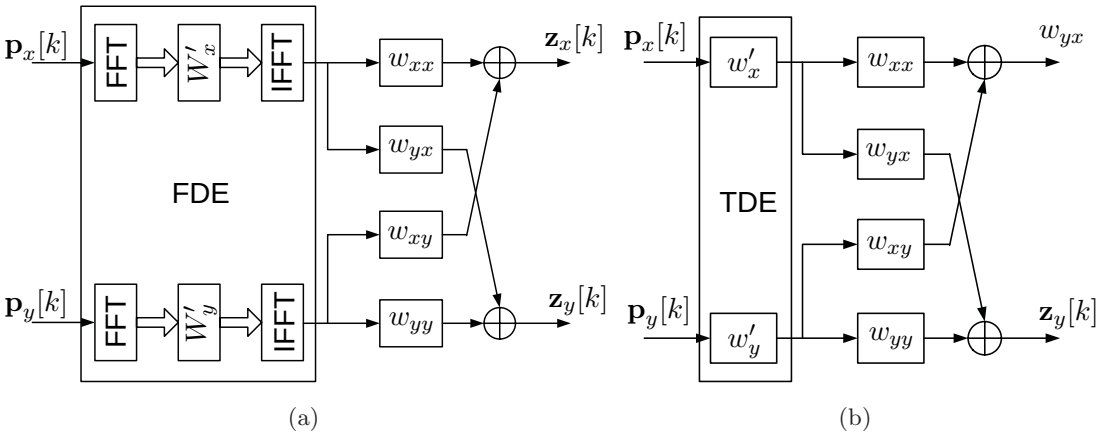

Figure 5.8: Chromatic dispersion and polarization mode dispersion compensation using: (a) frequency-domain equalization and (b) time-domain equalization.

If we consider TDA implementation (Figure 5.8(b)) the signal is multiplied in the time domain by the impulse response of the compensating filter:

$$w_c(t, l) = \mathcal{F}^{-1}(W_c(\omega, l)) = \sqrt{\frac{jc}{D\lambda^2 l}}\exp\left(-j\frac{\pi c}{D\lambda^2 l}t^2\right). \tag{5.9}$$

This impulse response is not only non-casual with infinite duration, but since it passes all the frequencies for a finite sampling rate it introduces also aliasing. All of this makes the digital implementation of (5.9) very difficult. In order to overcome these problems the impulse response of equation (5.9) must be truncated. The truncation process is performed calculating the largest truncation window that guarantees no aliasing. If the ADCs sample every T seconds, then the truncation window is given by:

$$-\frac{|D|\lambda^2 l}{2cT} < t < \frac{|D|\lambda^2 l}{2cT}. \tag{5.10}$$

In this case, the compensating filter can be implemented with a non-recursive FIR filter. If we use an high odd number of coefficients N, then the sampled impulse response is a good approximation of the continuous time impulse response and the taps coefficients are given by [9]:

$$a_k = \sqrt{\frac{jcT^2}{D\lambda^2 l}} \exp\left(-j\frac{\pi cT^2}{D\lambda^2 l}k^2\right) \text{ with } -\left\lfloor\frac{N}{2}\right\rfloor < k < \left\lfloor\frac{N}{2}\right\rfloor \text{ and } N = 2\cdot\left\lfloor\frac{|D|\lambda^2 l}{2cT}\right\rfloor + 1. \tag{5.11}$$

From equation (5.11), it can be noticed how the complexity of the FIR filter increases linearly with the length of the fiber (e.g. for 10.7 Gbouns/s system transmitting through a standard single mode fiber with $D = 17$ ps/(nm·km) and ADC sampling frequency of 21.4 GHz, the required number of taps for a transmission of 4000 km is 251 and for 40000 km is 2510). Conversely, the complexity of the FDE goes with $log_2 N$ [14]. Thus in the case of high values of accumulated dispersion $D \cdot l$, FDE is preferable.

In our model we implemented only the TDE. The coefficient values are directly derived by (5.11):

```
lambda = CONSTANT.c/ReferenceFrequency;
T = 1/(SamplingFrequency);
N = 2*floor(abs(D*1e-6)*lambda^2*Length/(2*CONSTANT.c*T^2))+1;
for n = 1 : length(k)
  a_k(n) = sqrt(-1i*CONSTANT.c*T^2/(D*1e-6*lambda^2*Length))*
    exp(1i*pi*CONSTANT.c*T^2/(D*1e-6*lambda^2*Length)*k(n)^2)
    ;
end
```

These coefficients are then used in N taps of the FIR filter:

```
for j = 1 : length(FinalTimeArray)
  if j <= length(a_k)
    E(j) = 0;
```

```
  else
      for nf = 1 : length(a_k)
        E(j) = a_k(n)*in(j - n) + E(j);
      end
   end
end
```

5.3.2 Polarization Mode Dispersion Compensating Block

As already mentioned before, another well-known problem in coherent communication is related to the State of Polarization (SOP) of the received signal. In fact, due to the fiber birefringence, present in almost all common fibers, there is a periodic power exchange between the two polarization components **x** and **y**. This makes the received signal SOP unknown and time varying.

As shown in section 4.3.2, this phenomenon can be modeled by means of the Jones Matrix as:

$$\begin{pmatrix} E_{x_{out}} \\ E_{y_{out}} \end{pmatrix} = \mathbf{J} \cdot \begin{pmatrix} E_{x_{in}} \\ E_{y_{in}} \end{pmatrix} = \begin{pmatrix} J_{xx} & J_{xy} \\ J_{yx} & J_{yy} \end{pmatrix} \cdot \begin{pmatrix} E_{x_{in}} \\ E_{y_{in}} \end{pmatrix}. \tag{5.12}$$

The Jones matrix **J** should both account for endless polarization rotation and for an initial unknown SOP. Therefore it can be expressed as:

$$\mathbf{J} = \begin{pmatrix} \cos(\omega t + \alpha) & \sin(\omega t + \alpha) \\ -\sin(\omega t + \alpha) & \cos(\omega t + \alpha) \end{pmatrix} \tag{5.13}$$

where ω is the angular frequency of rotation and α is the initial rotation.

We are now interested in understanding how to digitally keep track of the polarization rotation introduced by the fiber birefringence and how to compensate for it.

In order to do so, we have to estimate the Jones matrix **J** and obtain the inverse to compensate for the impairments incurred. Moreover, due to the time variation of **J**, the compensation should be adaptive.

From (5.12) it is evident how the optical channel can be seen as a special case of a more general Multiple-Input-Multiple-Output (MIMO) system (i.e. a 2×2 MIMO). Indeed, the output on one polarization depends both on the inputs on the **x** and **y** polarization (e.g. $E_{x_{out}} = J_{xx} \cdot E_{x_{in}} + J_{xy} \cdot E_{x_{in}}$). Thus, to compensate the polarization rotation, it is possible to use an equalizer for a MIMO system, as shown in Figure 5.8

[15] [9] [8]. The function of the circuit is expressed as:

$$\begin{pmatrix} E_{x_{out}} \\ E_{y_{out}} \end{pmatrix} = \begin{pmatrix} \boldsymbol{w}_{xx} & \boldsymbol{w}_{xy} \\ \boldsymbol{w}_{yx} & \boldsymbol{w}_{yy} \end{pmatrix} \cdot \begin{pmatrix} E_{x_{in}} \\ E_{y_{in}} \end{pmatrix} \tag{5.14}$$

where $\boldsymbol{w}_{xx}$, $\boldsymbol{w}_{xy}$, $\boldsymbol{w}_{yx}$ and $\boldsymbol{w}_{yy}$ are adaptive filters with M taps.

There are different method for adapting the equalizer. A popular choice is the Constant-Modulus-Algorithm (CMA), that is particularly efficient if applied to constant modulus modulation formats (e.g. M-PSK). However, the CMA has shown to be effective also with modulation formats that do not preserve the modulus (e.g. QAM) [29].

In order to understand how the CMA works, let us first assume to have a QPSK modulation with equal power on each input polarization component and to relate them to the total power $P_{tot_{in}} = |E_{x_{in}}|^2 + |E_{y_{in}}|^2$. In this way, after we have:

$$|E_{x_{in}}|^2 = |E_{y_{in}}|^2 = 1/2 \cdot P_{tot_{in}}. \tag{5.15}$$

As shown in (5.13), due to the fiber birefringence, there is a periodic power exchange between the two polarizations and therefore $|E_{x_{out}}|^2 \neq |E_{y_{out}}|^2$. Nonetheless, assuming that all the losses in the system are equally distributed on the two polarizations, the corrected received signal must respect the relation shown in (5.15). Hence, if we normalize the signals on **x** and **y** polarization with respect to the total output power $P_{tot_{out}}$:

$$\begin{aligned} |E_{x_{out,norm}}|^2 &= \frac{|E_{x_{out}}|^2}{P_{tot_{out}}}, \\ |E_{y_{out,norm}}|^2 &= \frac{|E_{y_{out}}|^2}{P_{tot_{out}}} \end{aligned} \tag{5.16}$$

the corrected signal must have:

$$\begin{aligned} |E_{x_{out,norm}}|^2 &= 1/2, \\ |E_{y_{out,norm}}|^2 &= 1/2. \end{aligned} \tag{5.17}$$

It is now clear that, in order to correct the polarization rotation, the CMA will attempt to minimize, in a mean square sense, the magnitude of the error $\epsilon_x = 1/2 - |E_{x_{out,norm}}|^2$ and $\epsilon_y = 1/2 - |E_{y_{out,norm}}|^2$. This corresponds to update the tap weights of (5.14)

symbol by symbol according to:

$$\begin{aligned}
\boldsymbol{w}_{xx}(k+1) &= \boldsymbol{w}_{xx}(k) + \mu(1/2 - |E_{x_{out,}}|^2)E_{x_{out}}E^*_{x_{in}} \\
\boldsymbol{w}_{xy}(k+1) &= \boldsymbol{w}_{xy}(k) + \mu(1/2 - |E_{x_{out}}|^2)E_{x_{out}}E^*_{y_{in}} \\
\boldsymbol{w}_{yx}(k+1) &= \boldsymbol{w}_{yx}(k) + \mu(1/2 - |E_{y_{out}}|^2)E_{y_{out}}E^*_{x_{in}} \\
\boldsymbol{w}_{yy}(k+1) &= \boldsymbol{w}_{xy}(k) + \mu(1/2 - |E_{y_{out}}|^2)E_{y_{out}}E^*_{y_{in}}
\end{aligned} \tag{5.18}$$

where all the complex fields are normalized and the subscript $_{norm}$ has been dropped for simplicity. In (5.18) μ is a convergence parameter and $E^*_{x,y}$ denotes the complex conjugate of $E_{x,y}$. In order to initialize the algorithm we can set all the tap weights to 0, but the central taps of $\boldsymbol{w}_{xx}$ and $\boldsymbol{w}_{yy}$ that are set to 1.

By using this adaptive equalization we can expect $|E_{x,y_{out}}|^2$ to converge to 1/2 after some iterations. However, as shown in [15], since all four filter are updated independently it is possible that both output ports have the same SOP. In order to avoid this, we can exploit the fact that, for polarization transformation we must have:

$$\begin{aligned}
\boldsymbol{w}_{yx} &= -\boldsymbol{w}^*_{xy} \\
\boldsymbol{w}_{yy} &= \boldsymbol{w}^*_{xx}
\end{aligned} \tag{5.19}$$

and therefore update the last two terms in (5.18) according to (5.19).

Since this condition corresponds to having the Jones matrix singular, another way to avoid the degeneracy of the same SOP on the two output ports of the equalizer is by monitoring the determinant of the Jones matrix in (5.14). If it approaches zero then the weights are reinitialized as:

$$\begin{aligned}
\boldsymbol{w}_{xx}(k) &= 0.5\left(\boldsymbol{w}_{xx}(k) + \boldsymbol{w}^*_{yy}(M-1-k)\right), \\
\boldsymbol{w}_{xy}(k) &= 0.5\left(\boldsymbol{w}_{xy}(k) - \boldsymbol{w}^*_{yx}(M-1-k)\right), \\
\boldsymbol{w}_{yx}(k) &= -\boldsymbol{w}^*_{xy}(M-1-k), \\
\boldsymbol{w}_{yy}(k) &= \boldsymbol{w}^*_{xx}(M-1-k),
\end{aligned} \tag{5.20}$$

where M is the number of taps of the adaptive filter.

Our Matlab® implementation of the adaptive filters is:

```
P_tot_mean = mean(abs(in_x).^2 + abs(in_y).^2);
new_in_x = in_x/sqrt(P_tot_mean);
new_in_y = in_y/sqrt(P_tot_mean);
```

```
mu = 0.05;
for kk=1:length(new_in_x)

    if kk-number_coeff+1<1
        lim1 = 1;
        lim2 = kk;
    else
        lim1 = kk-number_coeff+1;
        lim2 =number_coeff;
    end

    out_x(kk) = p_xx(1:lim2)*conj(new_in_x(kk:-1:lim1)') +
       p_xy(1:lim2)*conj(new_in_y(kk:-1:lim1)');
    out_y(kk) = p_yy(1:lim2)*conj(new_in_y(kk:-1:lim1)') +
       p_yx(1:lim2)*conj(new_in_x(kk:-1:lim1)');

    E_x = 0.5 - abs(out_x(kk)).^2;
    E_y = 0.5 - abs(out_y(kk)).^2;

    p_xx(1:lim2) = p_xx(1:lim2) + mu*E_x*out_x(kk).*conj(
       new_in_x(kk:-1:lim1));
    p_xy(1:lim2) = p_xy(1:lim2) + mu*E_x*out_x(kk).*conj(
       new_in_y(kk:-1:lim1));
    p_yx(1:lim2) = -conj(p_xy(1:lim2));
    p_yy(1:lim2) = conj(p_xx(1:lim2));
end
```

5.3.3 Digital Phase Estimation

As already mentioned in the first part of the chapter, coherent receivers based on OPLLs suffer from stringent laser linewidth requirements and implementation issues. For this reason most of the recent coherent receivers that make use of digital signal processing handle the carrier synchronization in the digital domain.

Theoretically, the digital phase estimation can use Feed Forward (FF) techniques [10][6] or closed loop concepts (DPLL [11]). On top of this, the estimation can be aided by pilot sequences, or non-data-aided. The main approach used in modern coherent receivers is based on non-data-aided FF techniques. In this section we will analyze only this approach, studying the possible implementations for the most popular modulation formats in coherent optical communication [10] [6].

Let us first assume to deal with a M-PSK modulation and to have a zero frequency offset between the signal laser and the local oscillator (i.e. $\omega_s = \omega_{LO}$). In this case we can express the digitalized complex field received by the digital phase estimation block as:

$$\mathrm{z}_{x,y}[k] = \sqrt{P_0} \cdot e^{-j(\phi_s(k)+\phi_n(k)+\phi_{LO}(k))} + n_c(k), \tag{5.21}$$

where $\phi_s(k) = 2m(k) \cdot \frac{\pi}{M}$ with $m(k) = \{1, 2, \ldots, M-1\}$ is the phase modulation of the signal, $\phi_{LO}(k)$ is the phase of the local oscillator, $\phi_n(k)$ is the phase noise introduced by both the signal and the local oscillator, and $n_c(k)$ is the complex noise due to ASE/shot noise. In order to retrieve the phase modulation ϕ_s we need to evaluate ϕ_n and ϕ_{LO}. This can be simply done taking the Mth power of $\mathbf{z}_{x,y}[k]$:

$$\begin{aligned}(\mathrm{z}_{x,y}[k])^M &= (\sqrt{P_0})^M \cdot e^{-j(M\phi_s(k)+M\phi_n+M\phi_{LO})} \\ &= (\sqrt{P_0})^M \cdot e^{-j(2m(k)\pi+M\phi_n+M\phi_{LO})}.\end{aligned} \tag{5.22}$$

In 5.22 it is evident how the M-th power removes the phase modulation. Since the ASE/shot noise in the term n_c contributes to the total phase error ϕ_{err}, it is appropriate to average (5.22) over a block of N symbols in order to have a better estimation of ϕ_{err}. The correction of the phase can be performed calculating the phase error individually for every symbol ("sliding window technique") or using a common phase error for a block on N symbols ("M-th power block scheme") [10]. The former solution (see Figure 5.9) is more accurate but difficult to use in a real time implementation. The latter (Figure 5.10) instead is more easily implementable but less performing.

In the case of "sliding window technique" the phase error ϕ_{err} of the k-th symbol is calculated through averaging with the phase error of the previous $N-1$ symbols as:

$$\Psi_{err}[k] = \frac{1}{M} \cdot arg\left[\sum_{n=0}^{N-1} (\mathrm{z}[k-n])^M\right] \tag{5.23}$$

Otherwise, using the "M-th power block scheme", the average is calculated once for every block of N symbols as:

$$\Psi_{err,i} = \frac{1}{M} \cdot arg\left[\sum_{n=0}^{N-1} (\mathrm{z}[n+(i-1)N])^M\right] \tag{5.24}$$

Through this operation the ASE/shot noise is diminished. However we have to consider that the phase error ϕ_{err} is also due to the phase noise in the signal laser and in the LO.

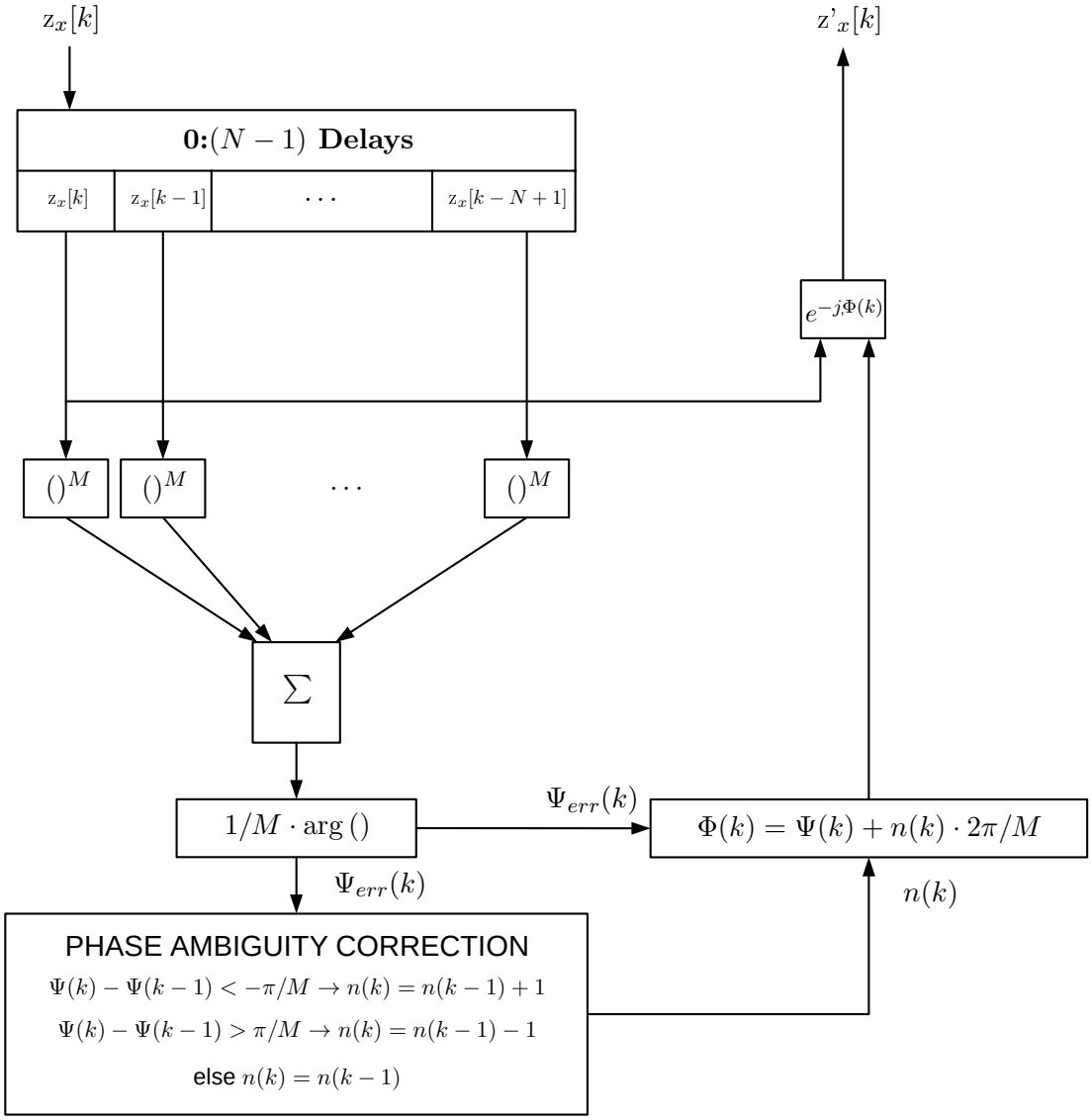

Figure 5.9: Block diagram of the digital phase estimation algorithm implemented with a non-data aided FF technique. In this scheme the phase error is calculated individually for each symbol ("Sliding window technique").

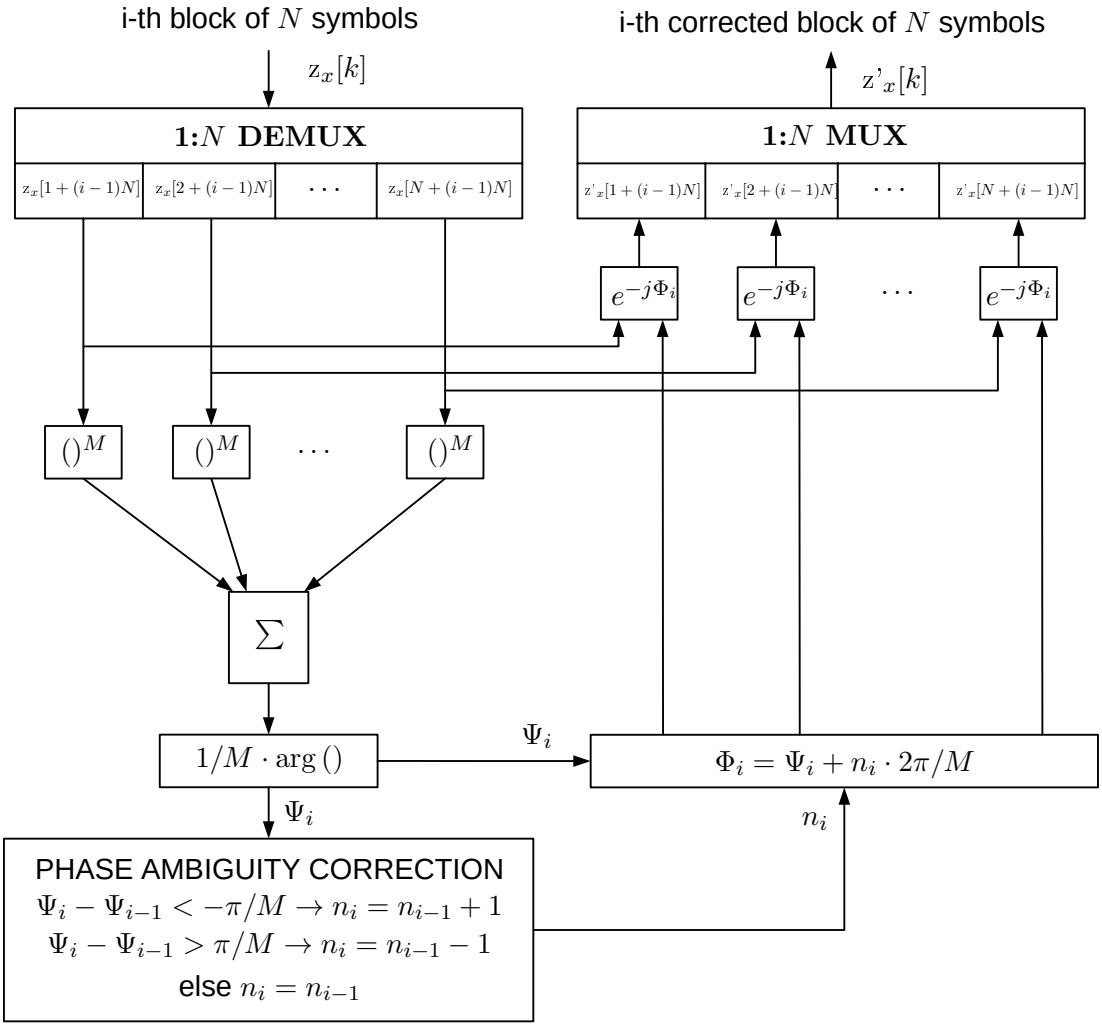

Figure 5.10: Block diagram of the digital phase estimation algorithm implemented with a non-data aided FF technique. This scheme performs the calculation of a unique phase error for a block of N symbols ("M-th power block technique").

Therefore, the calculation of the phase drift due to phase noise is worsened by averaging ϕ_{err} over N symbols. This means that the optimal length N for the averaging window is a trade-off between a good suppression of the ASE/shot noise and a good estimation of the phase noise.

The result of the arg-operation in (5.23) and (5.24) is an angle contained in the interval $]-\pi, \pi]$ and thus the estimation of the phase error Ψ_{err} will be limited in the interval $]-\pi/M, \pi/M]$. This introduces a M-fold phase ambiguity of $n \cdot 2\pi/M$ with $n \in \{0, 1, \ldots, M-1\}$. In order to solve this problem it is possible to use differential encoding in the case of M-PSK modulation and differential quadrature encoding in the case of square QAM modulation.

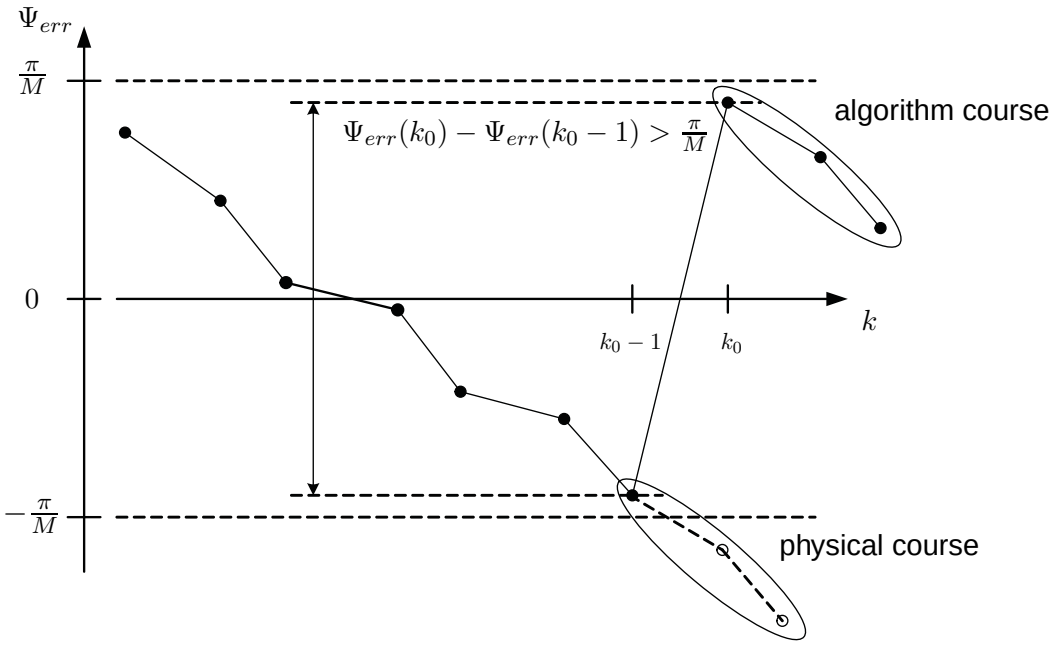

Figure 5.11: Phase jumps introduced by the arg-operation in the phase error estimation.

However, as one can notice from Figure 5.11, the physical trend of the phase drift cannot be followed by the algorithm because of the intrinsic limitation of Ψ_{err} between $-\pi/M$ and π/M. Due to this issue, every time the phase error becomes less than $-\pi/M$ or higher than π/M, the calculated value Ψ_{err} shows a jump of more than

$\pm\pi/M$. Hence, calling Φ_{err} the corrected value of the estimated phase error:

$$\Phi_{err}(k) = \Psi_{err}(k) - \frac{2\pi}{M}, \qquad \text{if} \quad \Psi_{err}(k) - \Psi_{err}(k-1) > \frac{\pi}{M}$$
$$\Phi_{err}(k) = \Psi_{err}(k) + \frac{2\pi}{M}, \qquad \text{if} \quad \Psi_{err}(k) - \Psi_{err}(k-1) < -\frac{\pi}{M}. \tag{5.25}$$

A way to implement this correction in the algorithm is to keep track of the number of jumps higher then $\pm\pi/M$ in an index $n(k)$. Every time $\Psi_{err}(k) - \Psi_{err}(k-1) > \frac{\pi}{M}$ then the index is updated as $n(k) = n(k-1)-1$, every time $\Psi_{err}(k)-\Psi_{err}(k-1) < -\frac{\pi}{M}$ then $n(k) = n(k-1) + 1$, otherwise $n(k) = n(k-1)$. Thus, the corrected phase error estimation is:

$$\Phi_{err}(k) = \Psi_{err}(k) + n(k) \cdot \frac{2\pi}{M}. \tag{5.26}$$

It is important to note that, in order for the algorithm to work, the phase walk cannot exceed the limit $]-\pi/M, \pi/M]$ within the average block duration. This gives an upper limit to the size N of the averaging block and this decreases with the increasing of the light source phase noise [7].

The phase error estimation given by $\Phi(k)$ is now correct and we can subtract it to the original signal by calculating:

$$\mathbf{z}'_x[k] = \mathbf{z}_x[k] \cdot e^{-j\Phi_{err}(k)}. \tag{5.27}$$

In our model we implemented both the "M-th power block scheme" and the "Sliding window technique". Its Matlab® implementation is fairly simple and the core code (for a M-PSK modulation) is:

```
for m = 1 : length(in)
  for i = 1 : length(in)/k_CR

    for j = 1 : k_CR
        D2(i) = D2(i) + (in(j+(i-1)*k_CR)*exp(-1j*pi/M))^M;
      end

      D2_angle(i) = angle(D2(i));
      psi(i) = angle(D2(i))/M;

      if i > 1
        if psi(i) - psi(i-1) < -pi/M
          n_i(i) = n_i(i-1) + 1;
        elseif psi(i) - psi(i-1) > pi/M
```

```
            n_i(i) = n_i(i-1) - 1;
          else
            n_i(i) = n_i(i-1);
          end
        end

      phi(i) = psi(i) + n_i(i)*2*pi/M;
    end
    out(m) = in(m)*exp(-1i*(phi(ceil(m/k_CR))));
end
```

in the case of "M-th power block scheme" and:

```
for i = 1 : length(in)
    for j = 1 : k_CR
        if (i-j+1) < 1
            break
        end
        D2(i) = D2(i) + (in(i - j+1)*exp(-1j*pi/M))^M;
    end

    D2_angle(i) = angle(D2(i));
    psi(i) = D2_angle(i)/M;

    if i > 1
        if psi(i) - psi(i-1) < -pi/M
            n_i(i) = n_i(i-1) + 1;
        elseif psi(i) - psi(i-1) > pi/M
            n_i(i) = n_i(i-1) - 1;
        else
            n_i(i) = n_i(i-1);
        end
    end

    phi(i) = psi(i) + n_i(i)*2*pi/M;

    out(i) = in(i)*exp(-1i*(phi(i)));
end
```

in the case of "Sliding window scheme", where `k_CR` is the averaging window length N in both techniques.

The algorithm for the estimation of the phase error shown in Figure 5.9 and 5.10 can be applied only to M-PSK signals. However, in the case of Star QAM and Square

QAM it can be applied with little modifications.

The former modulation presents equally spaced phases and therefore the suppression of the phase modulation through the M-th power can still be applied. Nevertheless, the signal does not present constant modulus and thus, before averaging, it must be normalized to amplitude one and (5.23) becomes:

$$\Psi_{err}[k] = \frac{1}{M} \cdot arg \left[\sum_{n=0}^{N-1} \frac{\mathrm{z}[k-n]^M}{|\,\mathrm{z}[k-n]|^M} \right] \tag{5.28}$$

It is important to note that, for a Star QAM modulated signal, M is not the number of symbols but the number of different phase states.

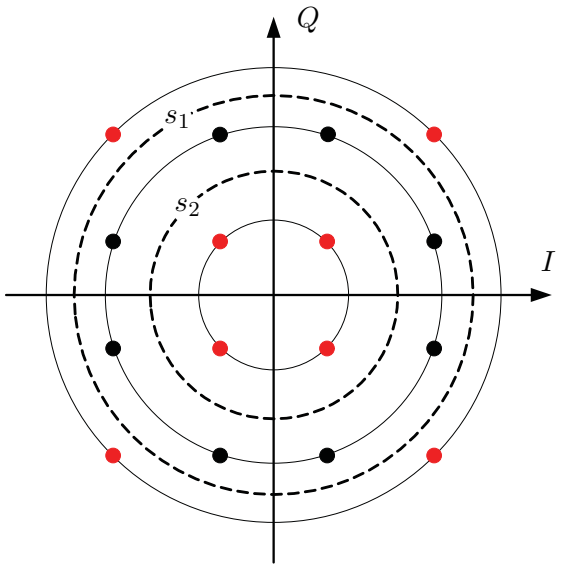

Figure 5.12: Different classes for the symbols of a 16QAM modulated signal. The red circles identify Class 1 symbols and the black Class 2 symbols.

In the case of Square QAM the phase states are not equally spaced and therefore the phase modulation cannot be suppressed by the M-power operation. However, as it can be seen in Figure 5.12, in the Square QAM constellation, two groups of symbols can be identified. The symbols marked with red circles, present equally spaced phases as in a Star QAM signal. Hence, it is possible to apply the phase error estimation with the M-power operation using just these symbols. In order to do that, it is necessary to partition the symbols that arrive to the phase estimation block, identifying those from Class I (red circles in Figure 5.12) and those from Class II. This partitioning can be

made with a decision on the intensity of the received symbol. Two threshold (s_1 and s_2 in Figure 5.12) are used. If the symbol presents an intensity higher than s_1 or lower than s_2 then it belongs to Class I and it is processed as in the case of a Star QAM. Otherwise, if the symbol belongs to Class II, the phase correction is made using the last calculated Class I correction angle.

It can be easily understood how the performance of the algorithm are worsened by the partitioning of the symbols. In fact, if we consider a Square 16-QAM signal, in average just one half of the symbols are used for the phase error estimation (this ratio is even smaller for higher order Square QAM) and we also must avoid long series of Class II symbols in order not to worsen the estimation even more.

In the Matlab® implementation of the "M-power block scheme" for a Square 16QAM modulation, the signal is firstly normalized in order to perform the discrimination between Class I and Class II points. The rest of the code is a direct extension of the M-PSK one:

```
scale = modnorm(in,'avpow',1);
in_norm = scale*in;

s1 = (sqrt(10/9) - sqrt(2/9))/2 + sqrt(2/9);
s2 = (sqrt(2) - sqrt(10/9))/2 + sqrt(10/9);
class = zeros(1, length(in)/SPS);
last_class_1 = 1;
class_1_number = 0;

for m = 1 : length(in)
    for i = 1 : length(in)/k_CR

        for j = 1 : k_CR
            if abs(in_norm(j+(i-1)*k_CR)) < s2 && abs(in_norm(
               j+(i-1)*k_CR)) > s1 || abs(in_norm(j+(i-1)*k_CR
               )) == 0
            class(j+(i-1)*k_CR) = 2;
            else
            class(j+(i-1)*k_CR) = 1;
            end
            if class(j + (i-1)*k_CR) == 1
                    D2(i) = D2(i) + ((in_norm(j + (i-1)*k_CR)*
                       exp(-1j*pi/M))^M)/(abs((in_norm(j + (i
                       -1)*k_CR)*exp(-1j*pi/M))^M));
            end
```

```
        end

        D2_angle(i) = angle(D2(i));
        psi(i) = angle(D2(i))/M;

        if i > 1
            if (class(i) == 1 && class_1_number > 0)
                if psi(i) - psi(last_class_1) < -pi/M
                    n_i(i) = n_i(last_class_1) + 1;
                elseif psi(i) - psi(last_class_1) > pi/M
                    n_i(i) = n_i(last_class_1) - 1;
                else
                    n_i(i) = n_i(last_class_1);
                end
                class_1_number = class_1_number + 1;
                last_class_1 = i;
            end
        end

    end

    for i = 1 : length(in)
        [min_val, index_first_class1] = min(class == 2);

        if class(i) == 1
            phi(i) = psi(i) + n_i(i)*2*pi/M;
        else
            if i == 1
               phi(i) =  psi(index_first_class1) + n_i(
                  index_first_class1)*2*pi/M;
            else
            phi(i) = phi(i-1);
            end
        end

    end
    out(m) = in_norm(m)*exp(-1i*(phi(ceil(m/k_CR))));
end
```

where `k_CR` is the size of the averaging block N. The "sliding window scheme" for a Square 16QAM has been implemented following the same technique as the one use in the "M-th power block scheme".

5.3.4 Frequency offset between the signal laser and the local oscillator

In the analysis made so far we started with the hypothesis of zero frequency offset between the signal laser and the local oscillator ($\Delta\omega = \omega_s - \omega_{LO} = 0$). However, this assumption is not true and in real systems the frequency offset $\Delta\omega$ is not negligible. Hence, equation (5.29) is not valid anymore and the digitalized complex field received by the digital phase estimation block is:

$$\mathrm{z}_{x,y}[k] = \sqrt{P_0} \cdot e^{-j(\Delta\omega t(k) + \phi_s(k) + \phi_n(k) + \phi_{LO}(k))} + n_c(k), \tag{5.29}$$

where the new term $\Delta\omega t(k)$ is the phase walk due to the frequency offset $\Delta\omega$.

As previously said, the total phase walk cannot exceed the limit $]-\pi/M, \pi/M]$ within the averaging block duration. This means that in order not to have errors in the phase correction, we must have:

$$\Delta\omega \cdot NT_s \quad \in \quad]-\pi/M, \pi/M]. \tag{5.30}$$

that in the case of a DQPSK at 10 GBt/s with $N = 10$ gives a maximum offset of $\Delta\omega = 780$ MHz. Moreover, even if (5.30) is respected, in case of high frequency offset, the phase noise tolerance of the receiver is highly restrained (see Section 6.3.4).

In the case of modulation formats with equally spaced phase states (e.g. M-PSK or Star QAM), a solution to this issue is to correct the frequency offset through the phase differential algorithm before the digital phase estimation block.

As in the case of the phase error estimation, the input complex field is firstly raised to the M-th power:

$$(\mathrm{z}_{x,y}[k])^M = (\sqrt{P_0})^M \cdot e^{-jM(\Delta\omega t(k) + \phi_n(k) + \phi_{LO}(k))} + (n_c(k))^M. \tag{5.31}$$

Afterwards, $(\mathrm{z}_{x,y}[k])^M$ it is multiplied by $(\mathrm{z}_{x,y}[k-d]^M)^*$. In the case we can neglect the ASE/shot noise n_c this can be written as:

$$(\mathrm{z}_{x,y}[k])^M \cdot (\mathrm{z}_{x,y}[k-k]^M)^* = (\sqrt{P_0})^2 M \cdot e^{-jM(\Delta\omega(t(k)-t(k-d)) + \phi_n(k) - \phi_n(k-d))} \tag{5.32}$$

since we can assume the phase noise difference $\phi_n(k) - \phi_n(k-d)$ to be Gaussian distributed we can isolate the frequency offset introduced by the local oscillator averaging

(5.32) over a large observation window. Thus, it is possible to obtain the frequency offset estimation as:

$$\Delta\omega_{est} = \frac{1}{MdT_s} \cdot \arg\left[\sum_{k=1+d}^{N} (\mathrm{z}_{x,y}[k])^M \cdot (\mathrm{z}_{x,y}[k-k]^M)^*\right]. \tag{5.33}$$

Again the restriction introduced by the use of the arg operation limits the values of the estimated frequency offset in the interval $]-\Delta\omega_{max}, \Delta\omega_{max}]$ where $\Delta\omega_{max}$ is given by:

$$\Delta\omega_{max} = \frac{\pi}{MdT_s}. \tag{5.34}$$

From (5.34) it is clear how the choice of the delay d is a trade of between a good accuracy of the frequency offset estimation (i.e. high d) and the frequency offset tolerance (i.e. low d).

As in the case of phase error calculation, this algorithm can be extended to the Star QAM simply normalizing the field of the symbol to amplitude one before averaging them. In this way (5.33) becomes:

$$\Delta\omega_{est} = \frac{1}{MdT_s} \cdot \arg\left[\sum_{k=1+d}^{N} \frac{(\mathrm{z}_{x,y}[k])^M}{|\mathrm{z}_{x,y}[k]|^M} \cdot \frac{(\mathrm{z}_{x,y}[k-k]^M)^*}{|\mathrm{z}_{x,y}[k-k]^M|^*}\right]. \tag{5.35}$$

Unfortunately, if the signal is Square QAM modulated, the symbols that present equally spaced phase states (i.e. the Class I symbols in Figure 5.12) are randomly distributed in time. This means that the two symbols $\mathrm{z}_x[k]$ and $\mathrm{z}_x[k-d]$ are not necessarily both Class I symbols and hence it is not possible to rise them the the M-th power in order to wipe out the phase modulation. Thus, this algorithm cannot be used to estimate the frequency offset in case of Square QAM modulation.

The Matlab® implementation of the frequency offset estimation is similar to the phase estimation implementation and core code is:

```
for i = (d_FO+1) : length(in)

  A1(i) = angle(in(i));

  for j = 1 : k_FO
    if (i - j+1-d_FO) < 1
        break
    end
  A2(i) = A2(i) + ((in(i - j+1)*exp(-1j*pi/M))^M)*conj((in(i -
      j+1-d_FO)*exp(-1j*pi/M))^M);
```

```
    end

    Delta_w0(i) = SymbolRate/(M*d_FO)*angle(A2(i));
    FO = mean(Delta_w0)/(2*pi);
    out_FO_compensated = in.*exp(-1i*FO*2*pi.*TimeArray);
end
```

where `d_FO` is the delay d and `k_FO` is the averaging window size N.

5.3.5 Data Recovery Circuit

In this section we present the implementation of the data recovery circuit for the principal modulation formats used in this project (i.e. DPSK, DQPSK and Square 16QAM).

After the received signal has been processed, mitigating the impairments introduced by the fiber and correcting the frequency offset and the phase error, the correct binary data must be decoded from the complex values of the signals on the **x** and **y** polarization. In Figure 5.13 the different stages of the data recovery circuit are shown.

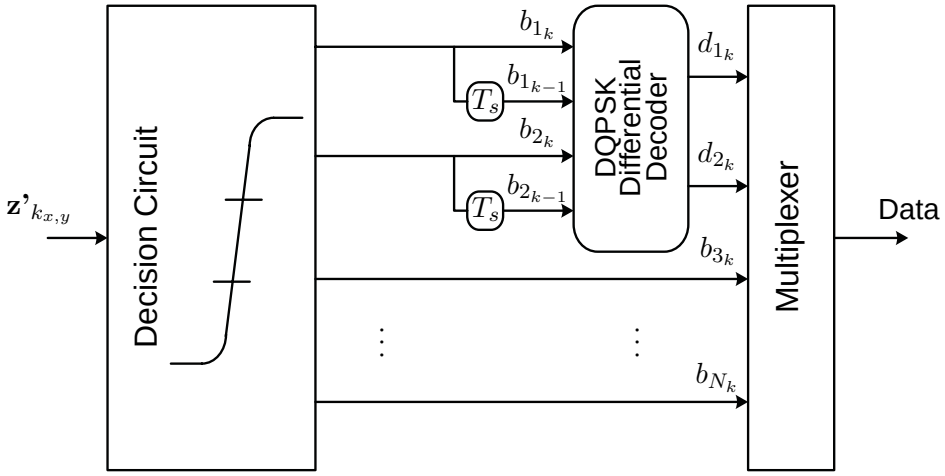

Figure 5.13: Block diagram of the decision circuit for a QAM signal.

Firstly the complex values of the processed signal $\mathbf{z'}_{x,y}$ are converted in a binary sequence according to the modulation format used. Each point of the received complex constellation is converted to a binary symbol with $N = \log_2(M)$ bits $(b_1, \ldots, b_N)$ where M is the modulation order of used format (e.g. in the case of DQPSK $M = 4$ and in the case 16QAM $M = 16$). In order to perform the conversion, the signal is firstly normalized and then the real and imaginary parts of the received complex field

is discriminated according to the thresholds correspondent to the modulation format considered. The decision on which symbol to assign to a certain complex value depends on the design used on the transmitter side. In Figure 5.14 the convention used in our project is shown.

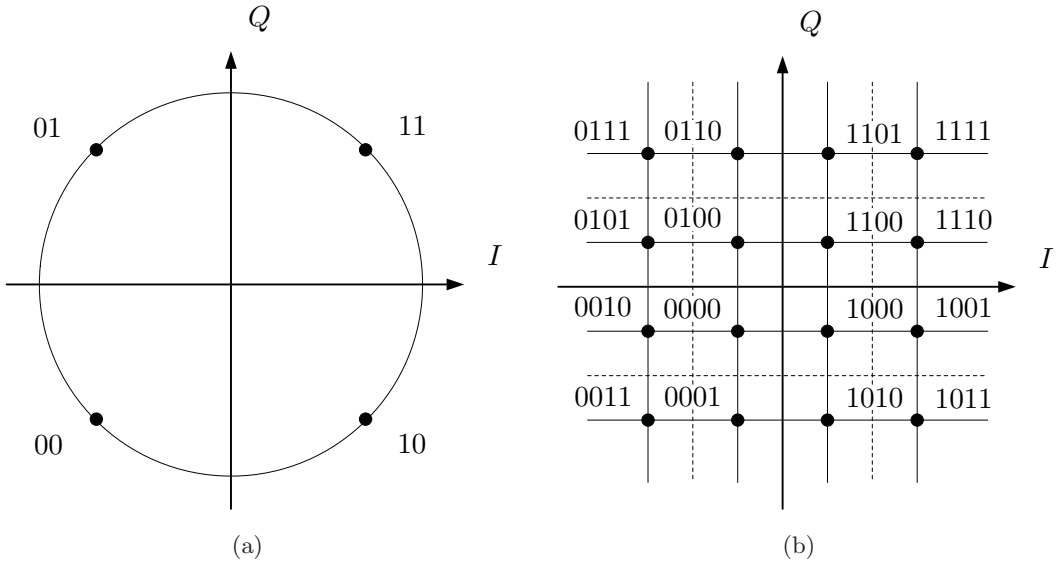

Figure 5.14: Symbol correspondence for the different points in the constellation diagram for both DQPSK and Differential Quadrant Encoded 16-QAM.

Due to the arg calculation, the phase estimation process gives a phase ambiguity of $2\pi/M$ for a M-PSK modulation and $\pi/2$ for QAM. In the case of QPSK and 16-QAM this means that there is a quadrant uncertainty on the received constellation.

For the QPSK modulation this is easily solvable using differential encoding. In this way the information is not encoded on the phase of the symbol itself but on the phase difference between two adjacent symbols. Thus, at the receiver side, the symbol sequence must be differentially decoded. The logic for the differential decoding of a DQPSK, as described in [10] [24], and it is:

$$d_{1_k} = \overline{b_{1_k}}\,\overline{b_{2_k}} b_{1_{k-1}} + \overline{b_{1_k}} b_{2_k} \overline{b_{2_{k-1}}} + b_{1_k} b_{2_k} \overline{b_{1_{k-1}}} + b_{1_k} \overline{b_{2_k}} b_{2_{k-1}}, \tag{5.36}$$

$$d_{2_k} = \overline{b_{1_k}}\,\overline{b_{1_{k-1}}}\,\overline{b_{2_{k-1}}} + b_{2_k} \overline{b_{1_{k-1}}} b_{2_{k-1}} + b_{1_k} b_{1_{k-1}} b_{2_{k-1}} + \overline{b_{2_k}} b_{1_{k-1}} \overline{b_{2_{k-1}}}, \tag{5.37}$$

where (d_1, d_2) is the decoded symbol.

In [10] it is also possible to find the table of truth.

The drawback of this is that one error on the differentially encoded signal causes two consecutive bits to be wrong, giving a 3 dB penalty.

In the case of 16-QAM the ambiguity is again only related to the quadrant of the received symbol. As described in Section 3.1.6.1 this is solved using Differential Quadrant Encoding. Out of the four bits (b_1, b_2, b_3, b_4) present in each symbol, the two that contain the quadrant information, in our case b_1 and b_2, are differentially encoded using a DQPSK encoder. The other two bits, b_3 and b_4, are encoded to be rotation symmetric and they can be correctly decoded despite the $\pi/2$ phase ambiguity. Hence, after the conversion of the complex received signal to binary sequence, the first two bits of the symbol are differentially decoded, as in the case of DQPSK, and then added to the other two to have the correct decoded symbol.

5.4 Optical Time-Division Demultiplexing Combined with Coherent Detection

In this section we discuss a possible implementation of Time-Division Demultiplexing compatible with the coherent detection.

5.4.1 Optical Time-Division Demultiplexing

In Figure 5.15 and 5.16 the different steps of the time-division demultiplexing are shown. Firstly, the OTDM signal (Figure 5.15 (a)) is used to recover the base-clock. Through it the pulse train at the base-clock rate, used as local oscillator, is synchronized with one of the n channels in order to exactly overlap with its pulses (Figure 5.15 (b)). Through $n-1$ delay lines of T_s/n, other $n-1$ versions of the local oscillators are made. Each of these is perfectly aligned with one of the other $n-1$ channels (see Figure 5.16). All the n versions of the LO are then made beat with only one of the OTDM signals through n different phase-diversity homodyne receivers. Each of these is then connected to a coherent receiver front-end through which each tributary is converted in the digital domain.

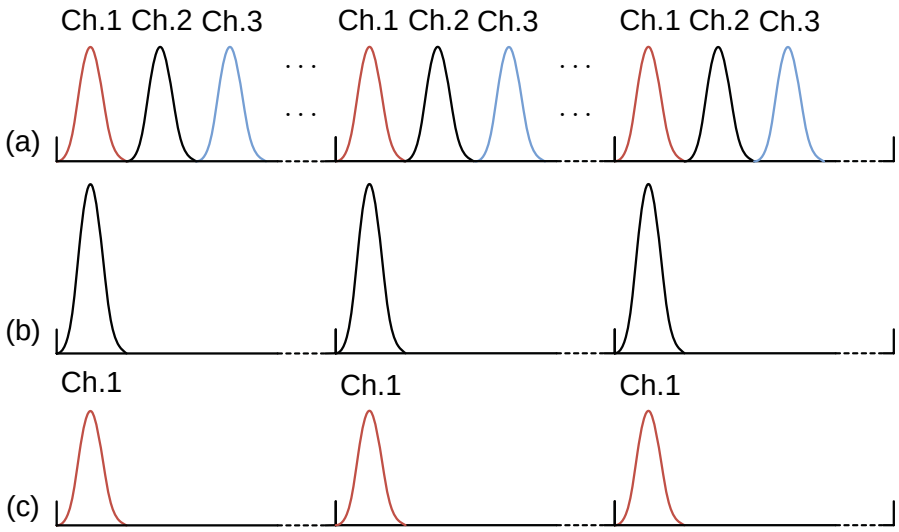

Figure 5.15: Principles of Time-Division demultiplexing. (a) OTDM signal received by the TD demultiplexer. (b) pulse source used as local oscillator to beat with the received signal. (c) demultiplexed output (channel 1 in the figure).

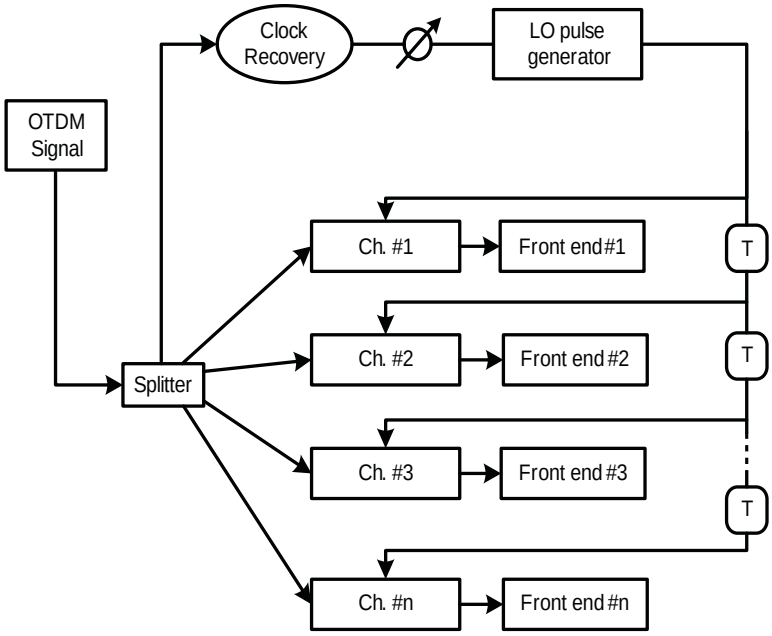

Figure 5.16: Block diagram of the time-division demultiplexer for coherent detection.

5.4.2 Electrical Part of the Digital Coherent Receiver for OTDM signals

The n ADCs are synchronized by the base clock. Again a series of $n-1$ delay lines is used to synchronize each ADC to one specific tributary. After the complex field is digitalized, it is sent to the DSP block.

According to whether there is interaction between the tributaries or not, the DSP block is different.

In the latter case, each tributary is sent to a different DSP sub-block and it is processed in parallel as described in Section 5.3. As a matter of fact, the information contained in each channel is independent of the others and can be processed separately.

If the tributaries interact with each other, as in the case of high broadening of the pulses, it is necessary to multiplex again the channels in the digital domain and serially process all the n signals together.

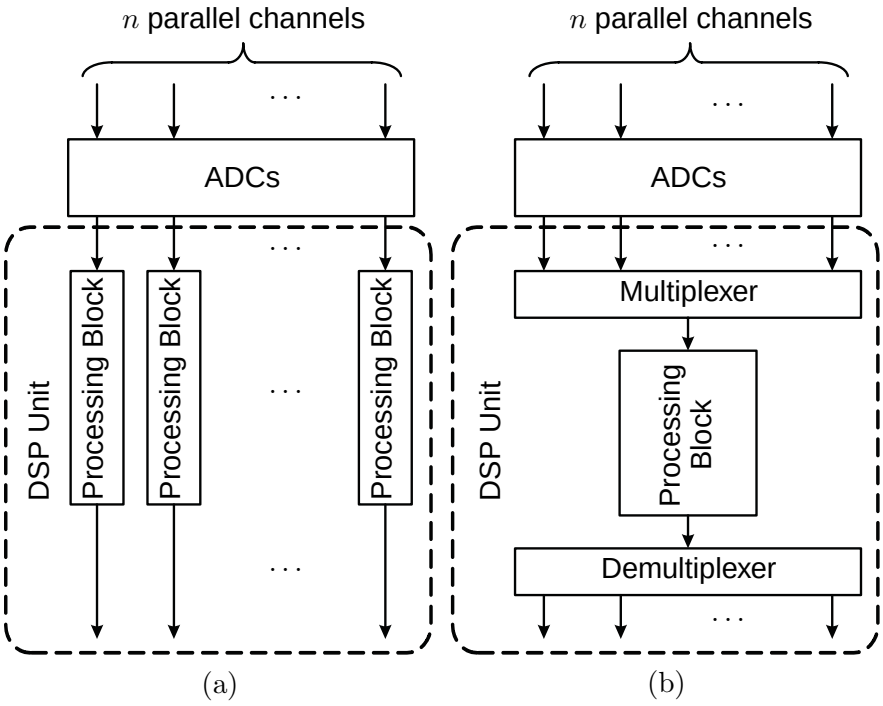

Figure 5.17: Block diagram of the DSP unit in the case of no interaction between the tributaries (a) and in the case the interaction cannot be ignored (b)

6

System Simulations

In this chapter we are going to present and analyze the Matlab® simulations performed with our model and we are going to discuss the findings related to the trends shown.

We will treat only systems with coherent receiver both with and without OTDM. For sake of simplicity and for time issues the modulation formats used will be restricted to NRZ-DQPSK-PolMux and NRZ-16QAM-PolMux in the case of single channel systems and RZ-DQPSK-PolMux and RZ-16QAM-PolMux in the case of 4-channels OTDM systems.

First, a description of the systems employed and of the specification utilized is give. All the parameter needed to repeat the simulations are going to be presented.

Afterwards, in the second section of this chapter, the system tolerances are going to be studied.

Finally, in the third section we are going to analyze the different components of the coherent receiver with DSP and we will show the functionalities and performance.

6.1 System Overview and Simulation Method

The systems studied in this chapter are a NRZ-DQPSK-PolMux, a NRZ-16QAM-PolMux, a 4-Channels OTDM DQPSK-PolMux and a 4-Channels OTDM 16QAM-PolMux with coherent receiver.

The simulations performed are monte carlo simulations (see Section 4.7) and the simulation parameters used are gathered in Table 6.1. The only difference between the OTDM and the single channel systems is the number of samples per symbol used. In

the case of OTDM systems the width of the pulses transmitted is very narrow and the resolution needed to correctly represent them is higher than the one needed for the representation of the NRZ signal used in the single channel simulations.

Table 6.1

Parameter	OTDM	Single Channel
Seed Length	9	9
Samples per Symbol	128	32
Error Threshold	100	100

The transmitter employed for our study (Figure 6.1) is a PolMux transmitter that utilizes a ML laser with pulses with a duty cycle of 10% of T_S in the case of OTDM transmission and a CW laser in the case of single channel transmission. During the simulations for systems tolerances to nonlinearities, the transmitter used is not PolMux. This is due to the fact that the implementation of the modeling for nonlinear effects in the fiber does not allow for the use of double polarization.

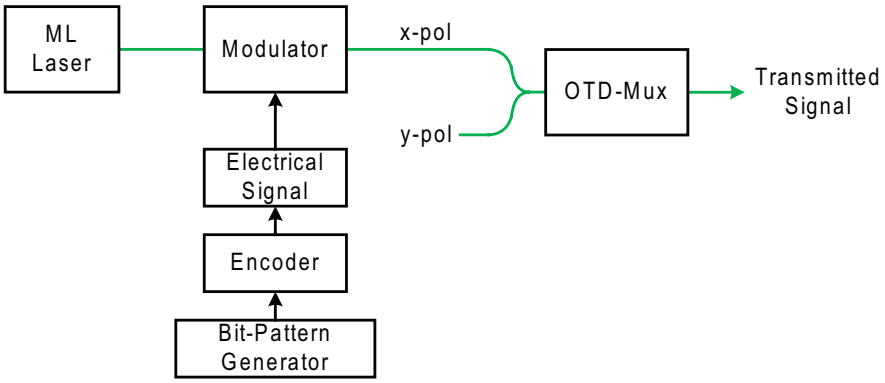

Figure 6.1: Block diagram of the transmitter utilized for the simulations of this section.

The OTD multiplexer employed is a PRBS preserving multiplexer as described in Section 4.2.2 that multiplexes the same signal on the four OTDM channels.

In Table 6.2, the main specification used for the transmitter are collected. We will suppose to use these values unless differently specified.

The optical link simulated (Figure 6.2) consists in single mode fiber followed by dispersion compensating fiber (DCF). The length of the two is set to 0 km by default and it is changed only for simulations regarding chromatic dispersion or nonlinearities

Table 6.2

Parameter	Symbol	Unit	Value
Transmitter Power (avg)	P_T	mW	1
Transmitter Frequency	f_{LO}	THz	193.1
Transmitter Linewidth	ν_T	Hz	0
Transmitter RIN	RIN_T	dB/Hz	-inf
Timing Jitter Standard Deviation (only ML)	$\sigma_t j$	s	0
Pulses Duty Cycle (only ML)	-	-	0.1
Electrical Signal Rise/Fall Time	$t_{r,f}$	s	$0.25 \cdot T_S$

tolerances. The DCF is used to compensate the chromatic dispersion and isolate only the nonlinear effect of the fiber. The specifications for the SMF and DCF used are gathered in Table 6.3. The OSNR imposition is done right after the fiber connection. Thus the noise is imposed on the OTDM signal before the optical filtering and the demultiplexing.

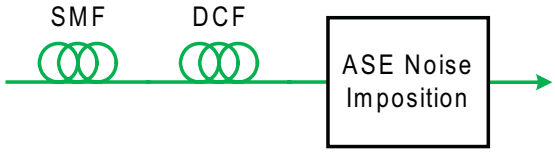

Figure 6.2: Optical channel as we set it for the simulations of this section.

The optical coherent receiver (Figure 6.3) consists in an initial optical filtering stage followed by the OTD demultiplexer. As explained in Section 5.4, the demultiplexing stage for a 4 channels OTDM signal consists in a set of 4 front-ends and a clock recovery. In the case of single channel transmission the OTD demultiplexer is substituted by a single front-end with clock recovery. The electrical signals output of the front-ends is then digitally converted by ADCs. In the case of OTDM systems this is done only on one channel. The digital signal is then processed by the DSP unit, converted into binary data and confronted with the sent data.

The LO used varies according to the type of system. In single channel simulations we used a CW laser with the same characteristic of the CW laser used in the transmitter (Table 6.2). In the case of OTDM with RZ signals the LO used is based on a phase modulation CW (PM-CW) pulse source. This is the same type of LO used in the

Table 6.3

Parameter	Symbol	Unit	Value
SMF Fiber Dispersion	D_{SMF}	Ps/(nm·km)	17
SMF Fiber Length	L_{SMF}	m	0
SMF Fiber Losses	α_{SMF}	dB/km	0
SMF Fiber Nonlinear parameter	γ_{SMF}	1/(W·m)	0.0013
DCF Fiber Dispersion	D_{DCF}	Ps/(nm·km)	-100
DCF Fiber Length	L_{DCF}	m	0
DCF Fiber Losses	α_{DCF}	dB/km	0
DCF Fiber Nonlinear parameter	γ_{DCF}	1/(W·m)	0
Polarization Rotation Frequency	ω_p	Hz·rad	0

laboratory experiment. The local oscillators characteristics are shown in Table 6.4.

Table 6.4

Parameter	Symbol	Unit	Value
LO Power	P_{LO}	mW	100
LO Frequency	f_{LO}	THz	193.1
LO linewidth	ν_{LO}	Hz	0
LO RIN	RIN_{LO}	dB/Hz	-inf
SMF Length	L_{LO}	m	210
Modulation Index	M	-	3
Electrical Oscillator Voltage (p-p)	V_{pp}	V	1
Electrical Oscillator Phase Noise	-	dBc/Hz	-inf

The DSP unit used consists in a CD compensation stage, a PMD and polarization rotation compensation stage, a frequency offset estimation, a digital phase estimation and a decision circuit. In Table 6.5 the specification used for the DSP block are show for the different modulation formats used.

6.2 System Tolerances

The system tolerances to the most important impairment factors are a good way to understand how the system is robust and susceptible to the degradation of the signal.

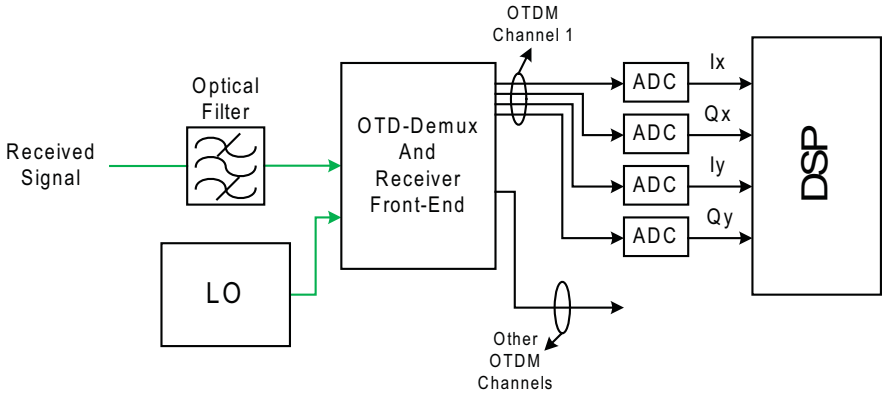

Figure 6.3: Block diagram of the receiver used for the simulations of this section.

Table 6.5

Parameter	DQPSK	16QAM
ADC Sampling Rate	$2/T_s$	$4/T_s$
CD compensation Equalization	TDE	TDE
taps PMD equalizer	1	1
Frequency Offset Estimation Delay	2	-
Frequency Offset Estimation Block Size	10	-
Phase Estimation Block Size	8	64

The single channel system and the OTDM one are going to be evaluated and confronted. First, the optimization of the optical and electrical filters is presented. Afterwards, with the optimal values for the filter bandwidths found, we are going to evaluate the OSNR requirements of the systems without impairments. At last, the chromatic dispersion tolerances, the linewidth requirements and the non-linearities tolerances are going to be analyzed.

The analysis has been carried out only for systems at 40 GBt/s and for the simulations regarding the system tolerances the DSP unit is limited to a digital phase estimation stage, the only necessary in a coherent receiver DSP unit.

6.2.1 Optimal Filter Bandwidths

The first step of our investigations was evaluating the optimal values for the optical and electrical filter bandwidths. The analysis has been performed by a series of MC simulations for different values of the optical filter bandwidth B_o and the electrical filter bandwidth B_e with constant OSNR. In the case of NRZ-DQPSK-PolMux the OSNR has been kept at 15 dB, for the NRZ-16QAM-PolMux at 22 dB, for the 4 channels OTDM RZ-DQPSK-PolMux at 21 dB and for the 4 channels OTDM RZ-16QAM-PolMux at 28 dB. As optical filter we used a Gaussian filter of the first order and as electrical filter a Bessel of the third order. The value of B_e has been varied between $0.4/T_S$ and $1.6/T_S$ in the case of single channel transmission and between $0.4/T_S$ and $5/T_S$ in the case of OTDM transmission, conversely B_o has been swapped between $1/T_S$ and $3.6/T_S$ in the case of single channel systems and between $3/T_S$ and $14/T_S$ in the case of OTDM. In Figure 6.4 the results of the two simulations are shown. The optimal points are marked by a star and they are $B_e = 0.6/T_S,\ B_o = 2.2/T_S$ for the NRZ-DQPSK-PolMux and $B_e = 0.7/T_S,\ B_o = 2.2/T_S$ for the NRZ-16QAM-PolMux for the single channel system, instead for the OTDM transmission we obtained $B_e = 3.7/T_S,\ B_o = 4/T_S$ for the RZ-DQPSK-PolMux and $B_e = 3.4/T_S,\ B_o = 5/T_S$ for the RZ-16QAM-PolMux.

For all the other simulations performed in this section we will use the optimal values for the filters bandwidth.

6.2.2 OSNR requirements

Once obtained the optimal values for the optical and electrical filters bandwidth we determined the back-to-back OSNR requirements of the systems. As described in section

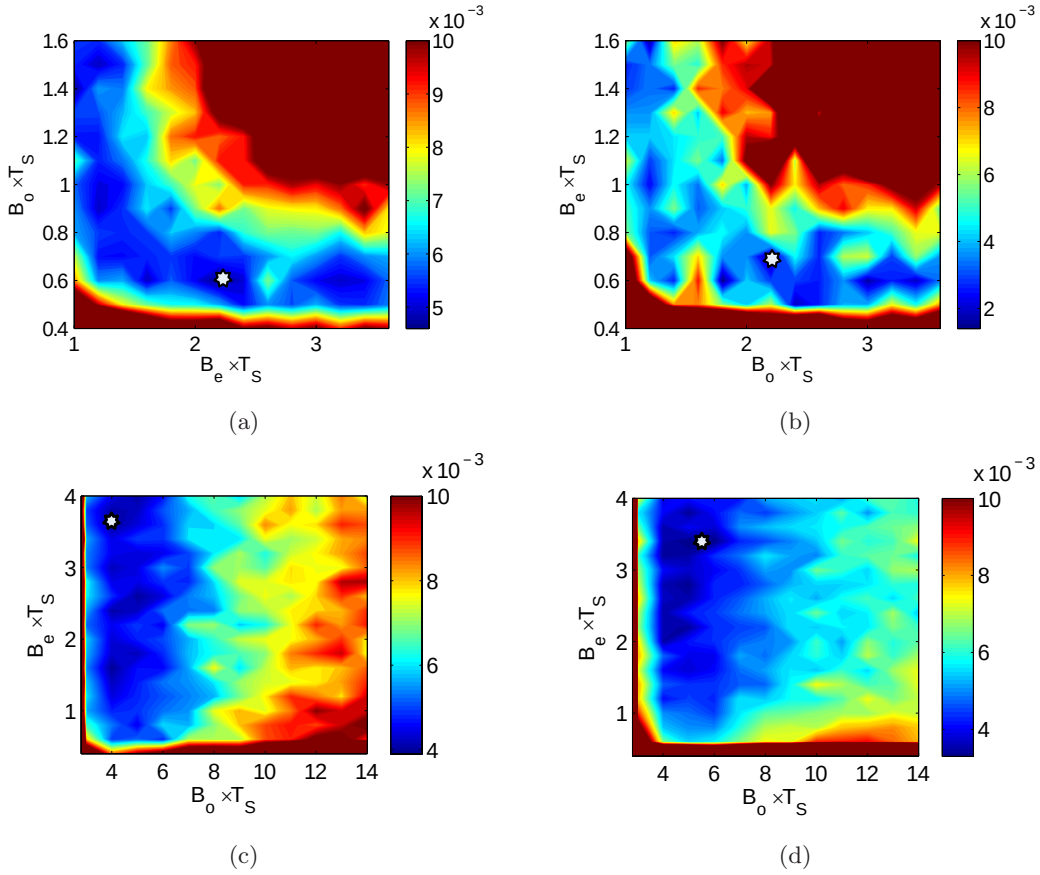

Figure 6.4: Optimal receiver filter bandwidth for (a) NRZ-DQPSK-PolMux, (b) NRZ-16QAM-PolMux, (c) 4 Channels OTDM DQPSK-PolMux and (d) 4 Channels OTDM 16QAM-PolMux. The optical filters used are Gaussian of 1st order and the electrical Bessel of 3rd order. The *stars* indicate the optimal value of BER obtained with the OSNR of (a) 15 dB, (b) 22 dB, (c) 21 dB and (d) 28 dB.

4.6, the OSNR value is imposed before the optical receiver filter, in order to simulate the ASE noise introduced by optical amplifiers.

The back-to-back OSNR requirements are important to have a unit of reference to confront the performance of the system affected by impairments.

In Figure 6.5 the BER versus OSNR curves for the DQPSK and 16-QAM in both a single channel and a 4-channels OTDM system are presented.

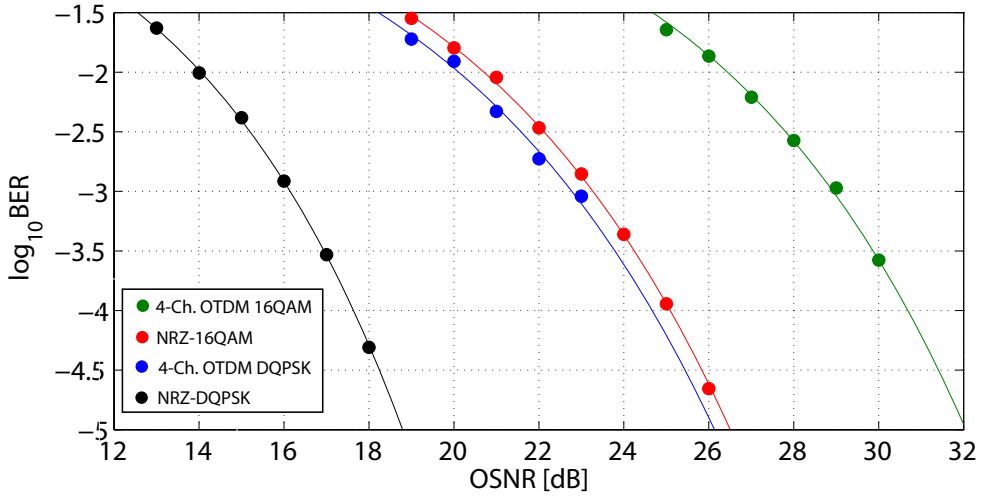

Figure 6.5: Back-to-back BER versus OSNR curves for NRZ-DQPSK-PolMux, NRZ-16QAM-PolMux, 4-Channels OTDM DQPSK-PolMux, and 4-Channels OTDM 16QAM-PolMux at 40 GBt/s.

6.2.3 Linewidth Requirements

The linewidth of the signal laser and of the local oscillator can strongly modify the performance of the system. In the case of coherent detection, the system is affected by both the linewidth of the transmitter laser and the LO one. Thus, in this case we should consider the beat-linewidth, given by the sum of the transmitter laser linewidth and the LO linewidth.

The receiver sensitivity penalty at BER = 10^{-3} versus the beat-linewidth for the two modulation formats is shown in Figure 6.6. The results obtained for the single channel NRZ systems are in line with those shown in [10]. As it can be seen, the linewidth tolerance is very high in the case of DQPSK systems both single channel and

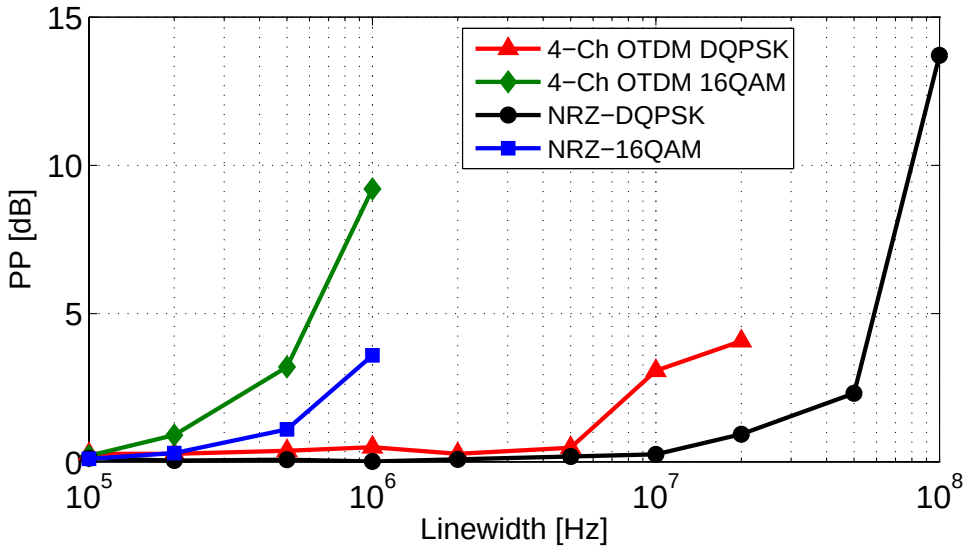

Figure 6.6: OSNR penalties at a BER of 10^{-3} with respect to the beat-linewidth for different modulation formats and systems.

OTDM. A beat-linewidth of 10 MHz does not introduce penalty in the first case and introduces only 3dB of penalty in the second one.

Conversely, the linewidth tolerance of 16QAM systems is much lower. In our simulation we did not manage to estimate the carrier phase with beat-linewidth higher than 1-2 MHz both in the OTDM systems and in the single channel ones. The problem of Square 16-QAM systems is related to the not-equally spaced phases of the signal constellation. This does not allow for the use of a pure M-th power block algorithm. Other solutions, like the use of a DPLL [11], showed better results with Square 16QAM formats, even if the improvement is not significant.

6.2.4 Chromatic Dispersion Tolerances

Here, the chromatic dispersion tolerances for systems with coherent detection and digital signal processing without CD compensation are discussed. In the results shown in Figure 6.7, the power penalty introduced by the transmission over a SMF of different length is shown for the four systems studied. As expected the OTDM systems present a very high penalty already after some hundreds of meters. As a matter of fact, the very narrow pulses of each OTDM channel broaden very rapidly, resulting in a high inter-

symbol-interference (ISI) and relative penalty. Moreover, the CD compensation in the DSP block would be possible only if the information of all the channels was processed together, making a parallelization of the OTDM channels not feasible and the required speed for the DSP unit very high (see Section 5.4). All this makes the OTDM systems very susceptible to CD and the digital compensation extremely difficult in practice.

On the other hand, the tolerance of the single channel systems is much higher. On top of this, the possibility of CD compensation on the DSP unit opens up the possibility of canceling almost all the penalty introduced by the chromatic dispersion.

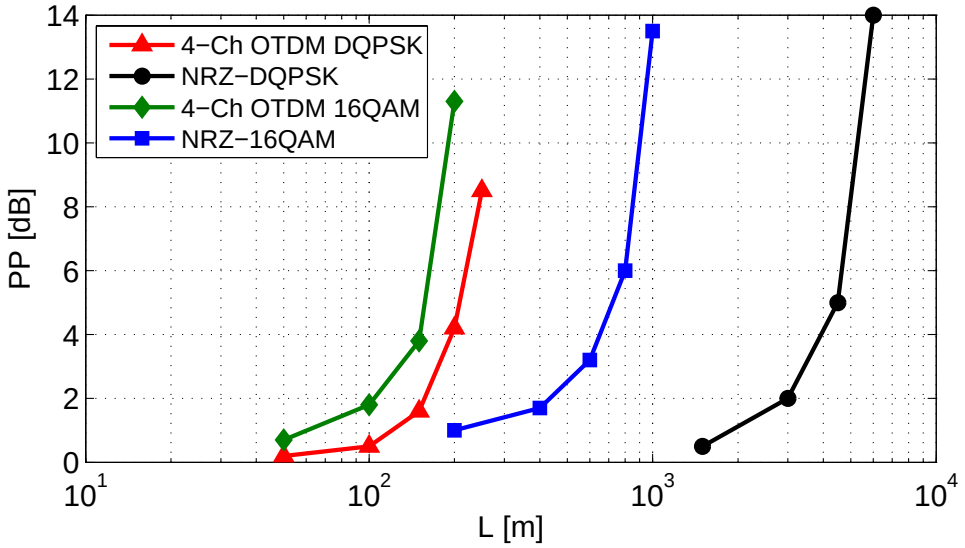

Figure 6.7: OSNR penalties at a BER of 10^{-3} with respect to SMF length for different modulation formats and systems.

6.2.5 Nonlinearities Tolerances

In order to understand the effects of fiber nonlinearities we simulated the transmission over 40 km of standard SMF (with the specification shown in Table 6.3) followed by 6.8 km of DCF for the compensation of the chromatic dispersion. The nonlinear propagation coefficient γ is set to 0 in the DCF connection so that the nonlinearities affect the signal only during the propagation along the SMF. The average fiber input power is varied and the OSNR penalties at 10^{-3} are shown in Figure 6.8. The systems simulated are a 40 GBt/s NRZ-DQPSK, a 40 GBt/s NRZ-16QAM, and a 40 GBt/s

4-channels OTDM 16QAM. The simulations for nonlinearities tolerances has been done with only one polarization since the implementation of the Kerr effect carried out in [22] is not realistic when two polarizations are used. This, because the two polarizations are processed separately.

It can be noticed how the NRZ-16QAM presents lower tolerances to nonlinearities than the NRZ-DQPSK. As a matter of fact, the 16QAM modulation is a multi modulus modulation and thus symbols with different amplitudes experience a different rotation due to self phase modulation (SPM). The 4-channels OTDM 16QAM system shows very similar tolerances with respect to the NRZ-16QAM if we consider the penalty with respect to the average power per channel.

Unfortunately we encountered problems with the simulation of the 4-channels OTDM DQPSK. This made the results of the simulations performed unrealistic and so we will not present them here. We did not manage to find the problem in our model but we will dedicate more time even after the delivery in order to solve it.

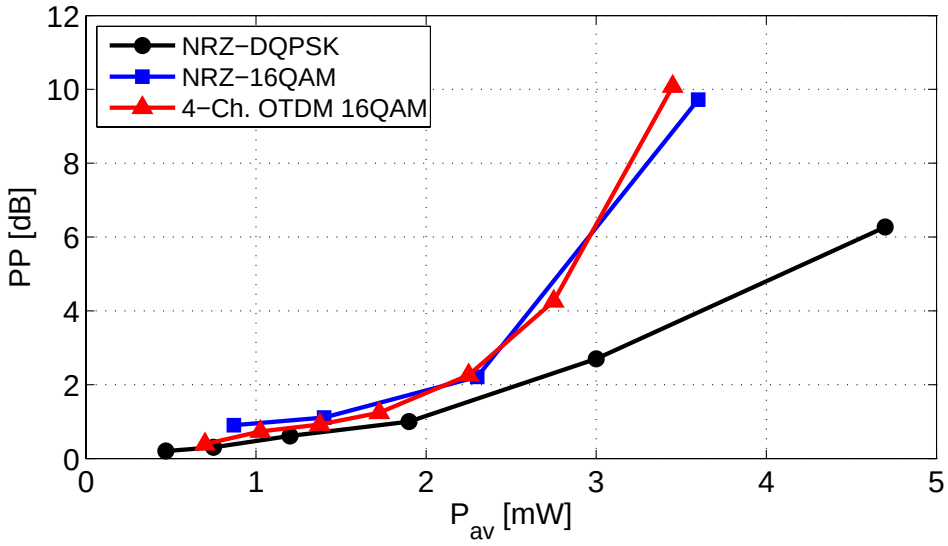

Figure 6.8: OSNR penalties at a BER of 10^{-3} with respect to the average signal power at the input of 40 km of SMF. Chromatic dispersion is fully compensated in a DCF which does not feature nonlinearities. The power for the OTDM system is the average power per channel.

6.2.6 IQ modulator bandwidth tolerances

The normalized bandwidth of the IQ modulators utilized to modulate the signal can affect the performance of the system. In Figure 6.9 the OSNR penalty at a BER of 10^{-3} with respect to the IQ normalized bandwidth is shown. The study of the IQ band requirements has not been carried out in this thesis, but is easy to understand the curves trends. The minimum normalized bandwidth necessary to reach the desired value of modulation in the signal at half of the symbol slot is 0.5. However, for B= 0.5, the modulation is fully reached only in one point of the symbol slot. This means that low penalties can be already present with normalized bandwidth higher than B= 0.5 (in Figure 6.9 this is particularly evident for 16QAM modulations). For lower bandwidth, the degradation of the signal is very fast and this is due to the fact that the desired modulation is not fully reached within the symbol slot duration.

The penalty plot shows slightly negative penalty for the OTDM DQPSK system with normalized bandwidth between 0.6 and 0.9. We did not manage to give a physical reason to this behavior and we are trying to find possible errors made in the simulation process.

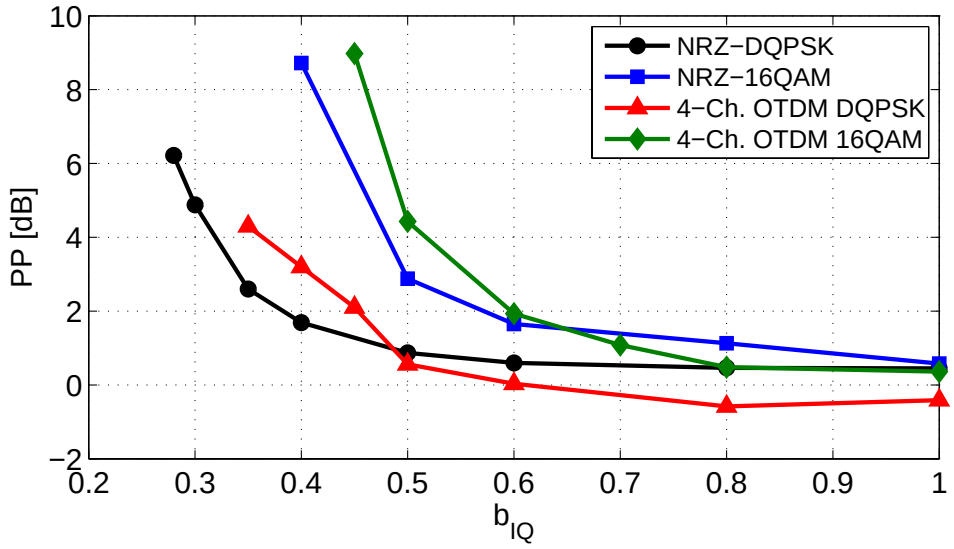

Figure 6.9: OSNR penalties at a BER of 10^{-3} with respect to the PM normalized bandwidth.

6.3 Digital Signal Processing Performance

After all the theory and the modeling description given in Chapter 5, in this section we are going to present the behavior of the DSP block and the different aspects that are important to be known. Each block of the DSP unit is analyzed separately. In order we are going to present the performance of the CD compensating block, PMD compensating block, digital phase estimation and frequency offset estimation.

The two systems used to perform the different analysis are a NRZ-DQPSK-PolMux and NRZ-16QAM-PolMux at 40 GBt/s and at 10 GBt/s.

6.3.1 CD Compensating Block

As described in 5.3.1, the chromatic dispersion can be compensated in the DSP unit. In this section, the improvement given by the use of TDE is shown. The 40 GBt/s NRZ-DQPSK-PolMux and NRZ-16QAM-PolMux are both transmitter through a standard SMF with a length of 300 km. The non-linearities have been neglected and thus the signal is affected only by the chromatic dispersion. The sampling rate of the AD converter is two times the symbol rate in the case of DQPSK and four times the symbol rate in the case of 16QAM. This gives a number of taps for the FIR filter of 264 and 1050 for the DQPSK and 16QAM system respectively.

In Figure 6.10, the complex field constellation of the signal before and after compensation, without ASE noise on the signal, is shown. The OSNR used is the back-to-back 10^{-3} limit, this is 16 dB for the DQPSK and 23 dB for the 16QAM system. It is evident how the TDE compensated almost perfectly the chromatic dispersion.

The penalty after the compensation is almost negligible (less than 0.25 dB) for the DQPSK system as shown in Figure 6.11. The MC simulation for the 16QAM system at 300 km has not been performed due to the fact that with an adaptive filter with 1050 taps a PRBS sequence of at least 2056 bits should be used. This would drastically increase the computation time making a MC simulation not feasible.

The samples per symbol with which the ADC samples are very important for the precision of the chromatic dispersion compensation. This improves the performance in two ways. First, the higher is the amount of samples per symbol used the better is the accuracy with which the signal is reproduced in the digital domain. Second the number of taps used by the TDE increases with the number of samples per symbol and

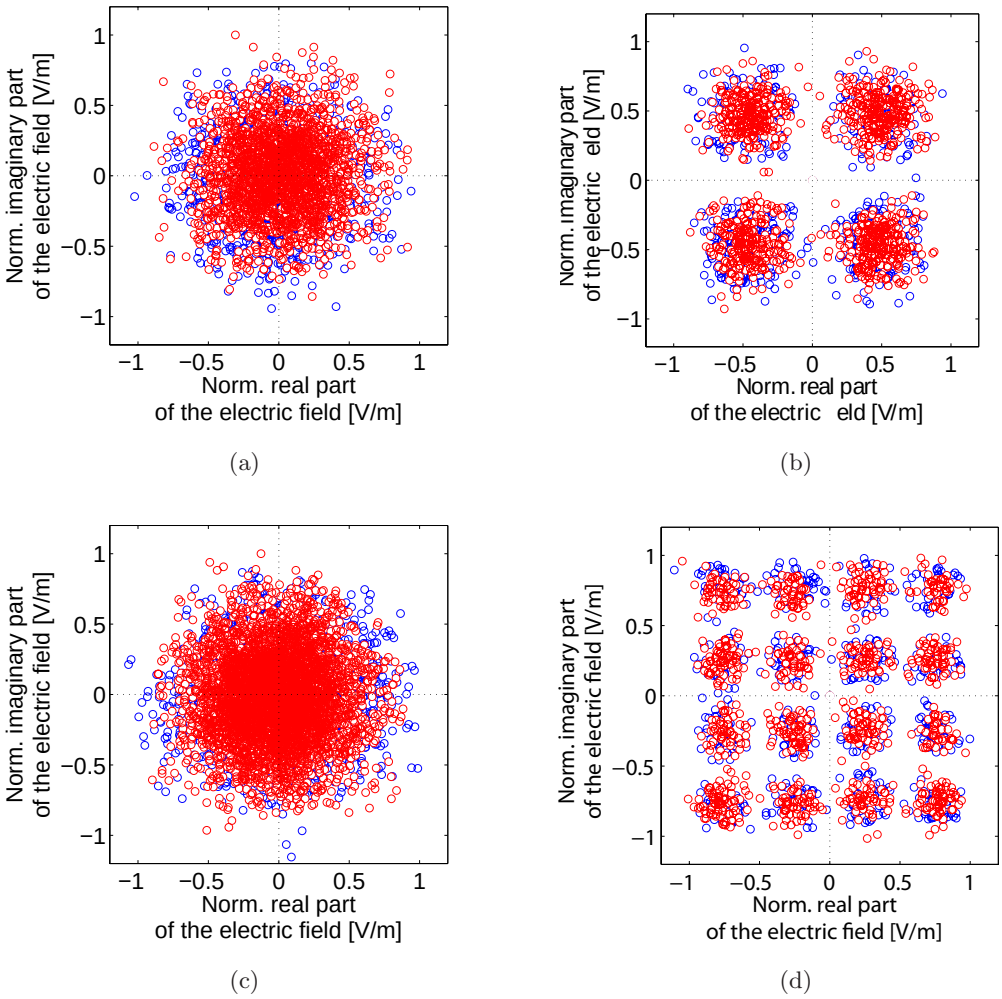

Figure 6.10: Constellation of the received signal before (a)(c) and after (b)(d) the CD compensation with a TDE for a 40 GBt/s NRZ-DQPSK-PolMux (a)(b) and 40 GBt/s NRZ-16QAM-PolMux signal (c)(d). The SMF length used is 300 km and the OSNR is 18 dB in the DQPSK system and 23 dB in the 16QAM one.

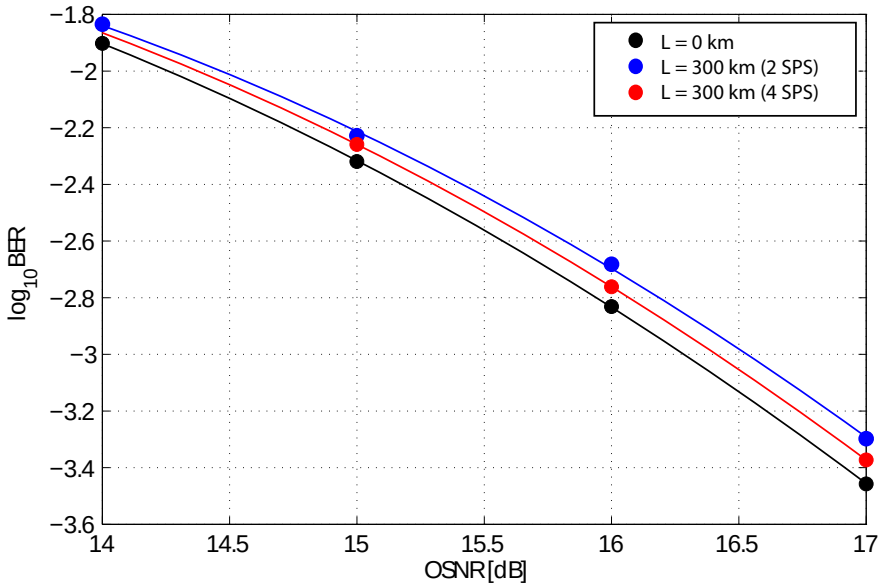

Figure 6.11: BER versus OSNR curves for 0 and 300 km of SMF and different sampling rates of the ADCs in a 40 GBt/s NRZ-DQPSK-PolMux.

therefore the correction made by the equalizer is higher. We tried to investigate this simulating the TDE compensation for the chromatic dispersion accumulated after 300 km of SMF with a sampling rate of the ADCs of 2 and 4 times the symbol rate. As it can be seen in Figure 6.11, the penalty of 0.25 dB present with 2 samples per symbol is halved with 4.

It must be underlined how this CD compensation technique is not "blind", but it relies on information about the fiber length and dispersion. The precision of the latter can be considered high, but sometimes, in real systems, the length of the fiber used cannot be know with extreme precision. Thus, it might be interesting knowing the penalty introduced by an error in the estimation of the fiber length. In Figure 6.12 the BER versus OSNR curves are presented for a NRZ-DQPSK-PolMux at 40 GBt/s with a 300 km of standard SMF with CD compensation performed with an error of 0.1%, 0.5% and 1% on the fiber length information. It can be noticed how an error of only 1% on the total length (in this case 300km) gives a penalty of 2.25 dB.

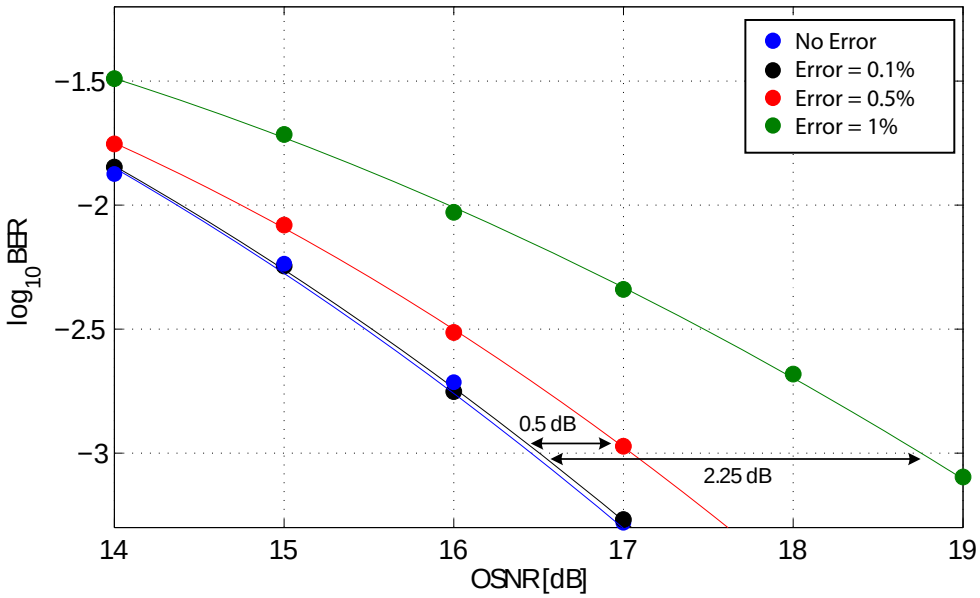

Figure 6.12: BER versus OSNR curves for a CD compensation with different errors on the estimated fiber length in a 40 GBt/s NRZ-DQPSK-PolMux.

6.3.2 Polarization Rotation Control and PMD compensation

The signal filtered by the FIR TDE is then processed by the adaptive filter responsible for the polarization rotation control and PMD compensation. In this section we are going to show the resilience of the filter to the polarization rotation and the dependence on the convergence parameter μ. The system used to test this block is a NRZ-DQPSK-PolMux at 10 GBt/s. As explained before the polarization rotation presents both an initial random rotation and a constant rotation of angular frequency ω_r. Firstly we tested the dynamic response of the adaptive filter. In order to do this we performed different MC simulations with equal OSNR and varying the polarization rotation frequency ω_r. The adaptive filter used presented one tap and a convergence parameter $\mu = 0.05$. The result is shown in Figure 6.14 where the BER versus the rotation frequency ω_r is shown.

The results obtained are in good agreement with those obtained in [9] and show a flat response up to more than 1 MHz.

An analysis of the equalizer performance with different convergence parameter values followed. In order to do this we calculated the error between the ideal signal and

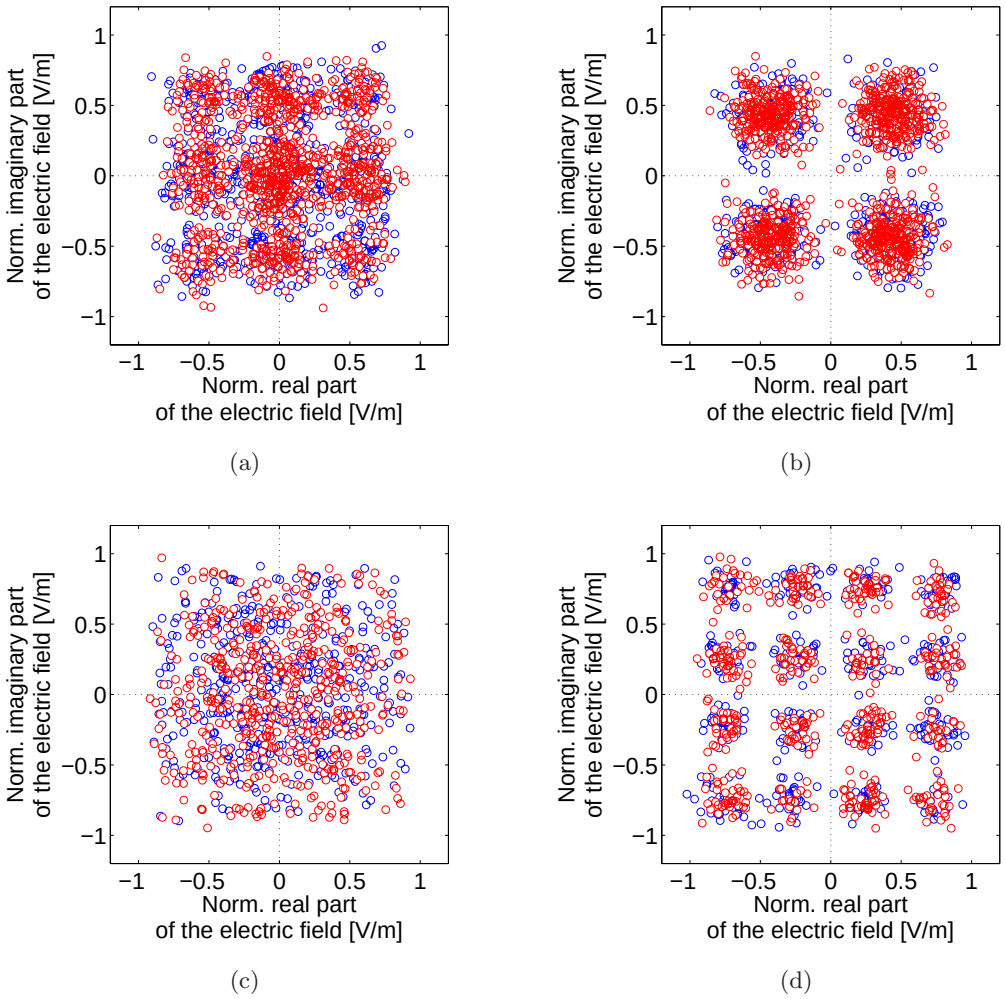

Figure 6.13: Constellation of the received signal before (a)(c) and after (b)(d) the PMD and polarization rotation compensation in a 40 GBt/s NRZ-DQPSK-PolMux (a)(b) and 40 GBt/s NRZ-16QAM-PolMux system (c)(d). The OSNR is 18 dB in the DQPSK system and 23 dB in the 16QAM one.

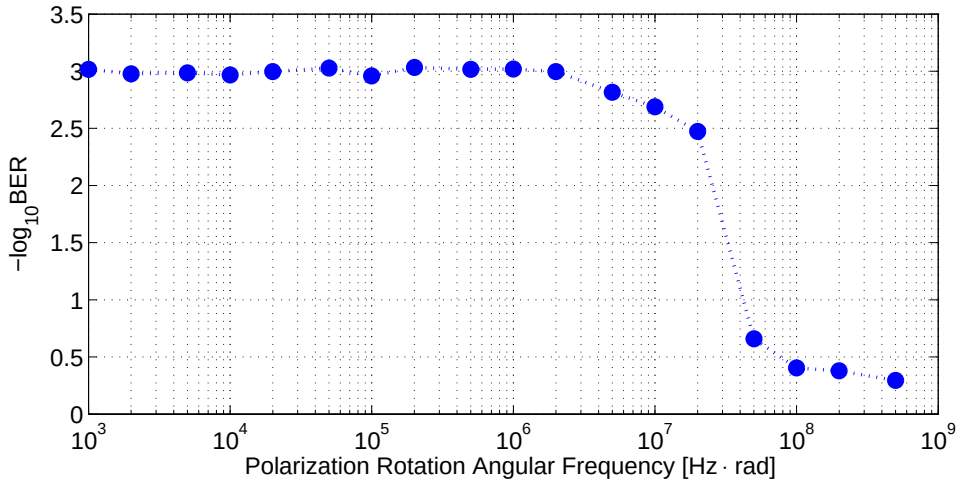

Figure 6.14: BER versus polarization rotation frequency for a 10 GBt/s NRZ-DQPSK-PolMux with adaptive equalization with one tap.

the equalized one after the adaptive filter. This error has been monitored in time to see both the speed of the response and the accuracy of the equalization. The results are shown in Figure 6.15. It is evident how decreasing the value of μ we slow the response of the equalizer. However, as shown in Figure 6.15(b), the accuracy of the equalizer increases for smaller μ worsening the performance of the system. A good compromise between speed and accuracy is give, for adaptive equalizers with one tap, with μ comprised between 0.05 and 0.01.

6.3.3 Digital Phase Estimation

The phase estimation can be performed, as explained in Chapter 5, exploiting the Viterbi-Viterbi algorithm. In this section we will investigate on the algorithm performance employing the *M-th power block scheme*. In the end of the section we will also show a comparison between the performance of the M-th power block scheme and the Sliding window scheme.

Firstly, we carried out an analysis to identify the optimal values for the dimensions of the averaging blocks. Different MC simulations have been run with different averaging block sizes and increasing linewidth. The results are shown in Figure 6.16 for the DQPSK and 16QAM system.

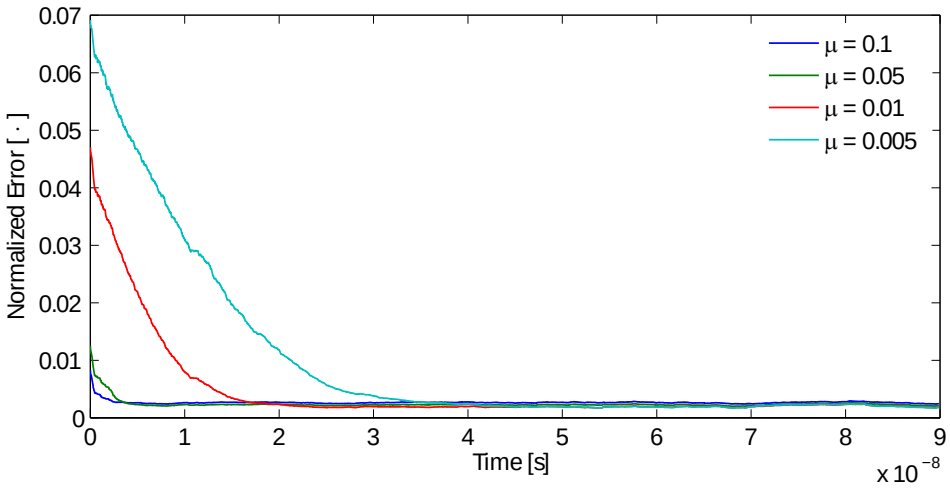

(a)

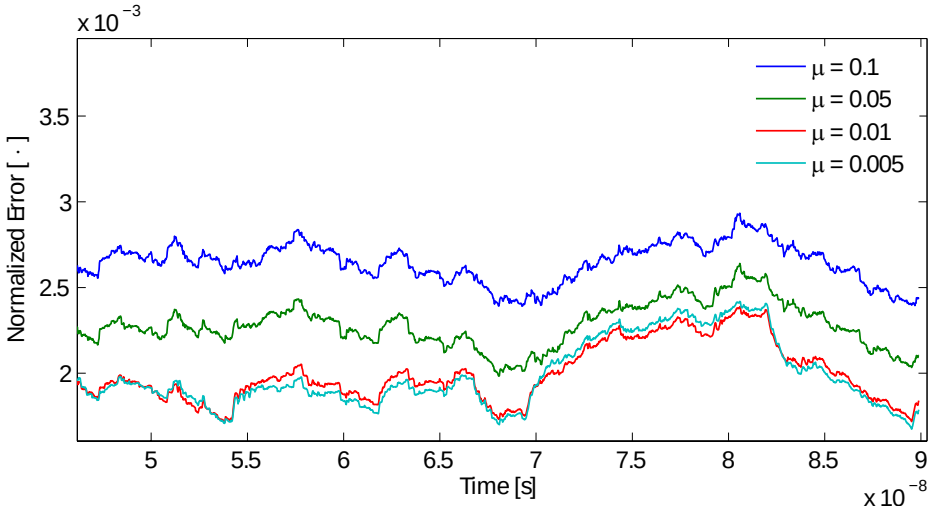

(b)

Figure 6.15: Error of the corrected signal as a function of time after the adaptive equalization for the correction of the PMD and polarization rotation with different convergence parameters μ (a) and detail of the residual error after the equalization has converged (b).

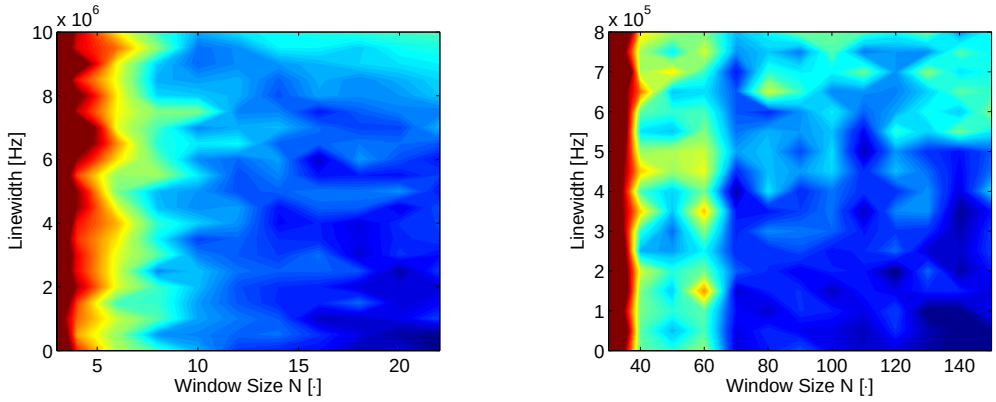

(a) (b)

Figure 6.16: Optimal block length for different beat-linewidth in a 40 GBt/s NRZ-DQPSK-PolMux (a) and 40 GBt/s NRZ-16QAM-PolMux (b) system.

It can be noticed that with no linewidth the performance increases with an increase in the window size. This because the wider the window is the better the averaging of the ASE noise becomes. However, for higher values of laser linewidth, the window size presents an optimal point. This is due to the fact that the increase in the laser linewidth means an increase in the signal phase noise. Thus, the optimal value of the averaging block size is a trade off between a good averaging of the ASE noise and a low phase walk in the time window of the block.

The tolerances to laser linewidth of an optical system with coherent receiver and DSP have been already presented in Section 6.2.3. In Figure 6.17, the constellation before and after the digital phase estimation are shown. In the case of NRZ-DQPSK-PolMux, the beat-linewidth is 20MHz and for a NRZ-16QAM it is 1 MHz.

Finally, a comparison for the two techniques used to estimate the phase of the carrier has been done. As it can be seen in Figure 6.18, the sliding window scheme shows a consistent improvement in the performance only for very high beat-linewidth. In 16QAM systems this difference is more marked because the optimal averaging window used is generally bigger (e.g. in these simulations the 16QAM averaging window used is 64 symbols and the DQPSK one is only 10) and this accentuates the lower accuracy given by the M-th power block scheme. It must be again underlined how the better performance of the sliding window technique are not given for free. In fact, the implementation of this algorithm in a real DSP system would require much higher speed

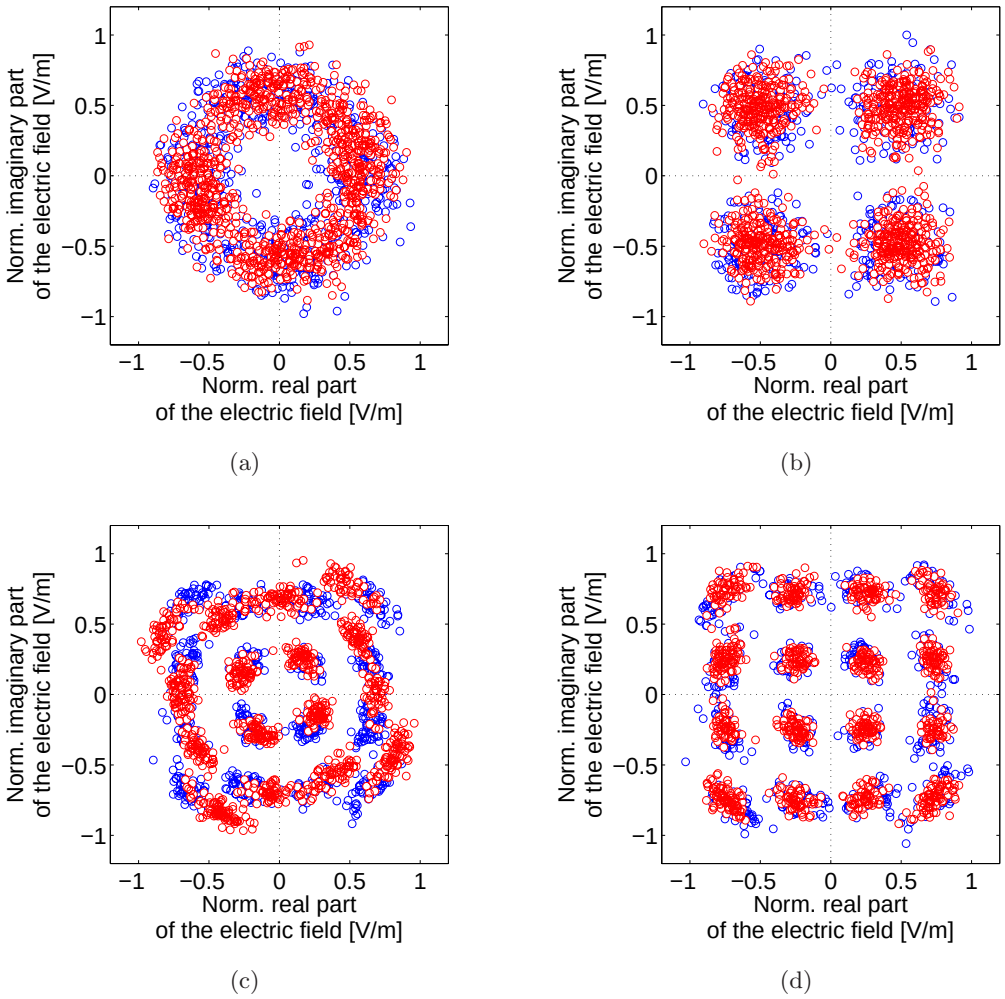

Figure 6.17: Constellation of the received signal before (a)(c) and after (b)(d) the digital phase estimation in a 40 GBt/s NRZ-DQPSK-PolMux (a)(b) and 40 GBt/s NRZ-16QAM-PolMux system (c)(d). The OSNR is 18 dB in the DQPSK system and 23 dB in the 16QAM one.

in the electronic component since the phase estimation must be done for each symbol. Thus, in our opinion, the choice of M-th power block scheme is generally preferable.

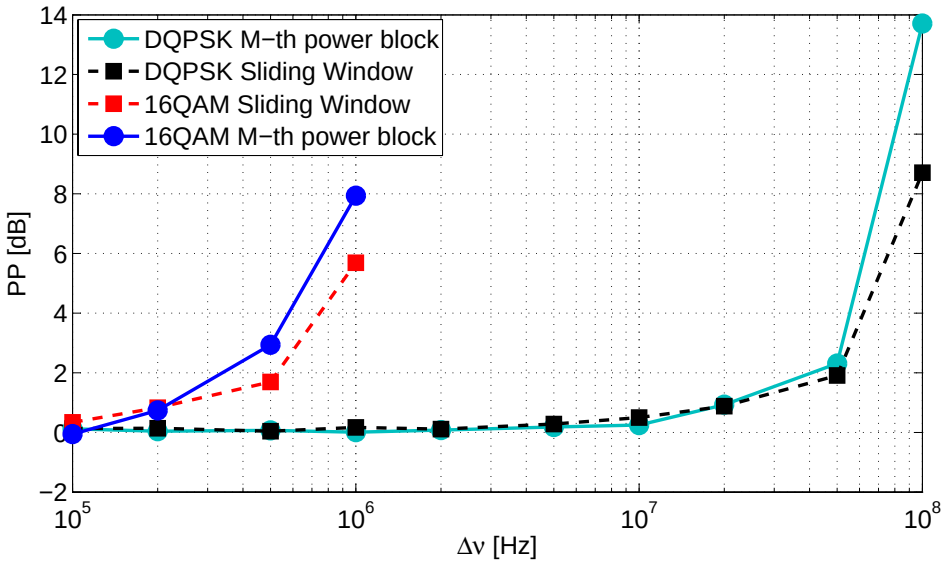

Figure 6.18: Comparison between the OSNR penalties at a BER of 10^{-3} with respect to the beat-linewidth with different digital phase estimation techniques.

6.3.4 Frequency Offset Compensation

As already explained in Section 5.3.4, the frequency offset between the transmitter laser and the LO is a very important parameter. Algorithms for the phase estimation, like the Viterbi-Viterbi algorithm, can isolate the phase walk $\Delta\omega t$ from the phase modulation of the signal and compensate for the frequency offset. However, in the case of high values of $\Delta\omega$ the phase walk is too fast and the phase estimation algorithm cannot keep track of it. In Figure 6.19, the penalty introduced by the frequency offset between the transmitter laser and the LO is shown for a NRZ-DQPSK-PolMux at 10 GBt/s. As it can be seen the 2 dB penalty is obtained for approximately 50 MHz of offset and the algorithm is able to partially correct the offset up till 400 MHz (with a penalty of almost 15 dB).

A method to further improve the performance of a system that presents equally spaced phase states (e.g. a DPSK or DQPSK system) is to employ the *frequency offset estimation algorithm*. This allows for a compensation of the frequency offset up

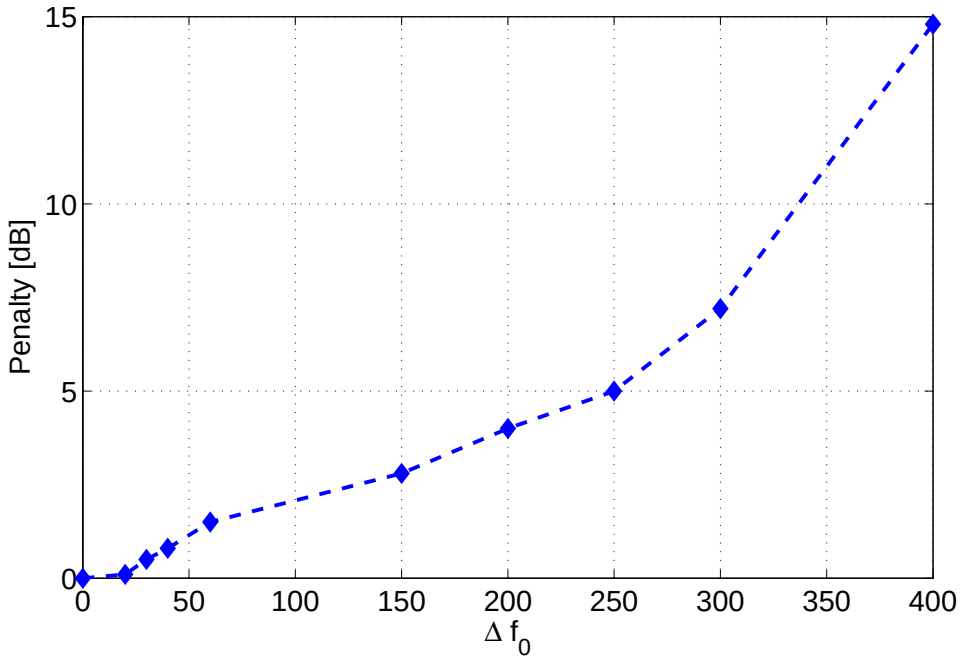

Figure 6.19: OSNR penalties at a BER of 10^{-3} with respect to the frequency offset between the signal and LO lasers for a 10 GBt/s NRZ-DQPSK-PolMux system.

to $\Delta\omega_{max} = 1/(2MdT_S)$ with very low penalty. In Figure 6.20 the residual penalty obtained utilizing the frequency offset estimation on a NRZ-DQPSK-PolMux at 10 GBt/s is shown. Unlike the system with only phase estimation, that presented a penalty of almost 15 dB, in this case the penalty is only 0.8 dB. As we will see in Chapter 7, this improvement is very important when it is not possible to lock the frequency of the local oscillator at exactly the same frequency of the signal laser.

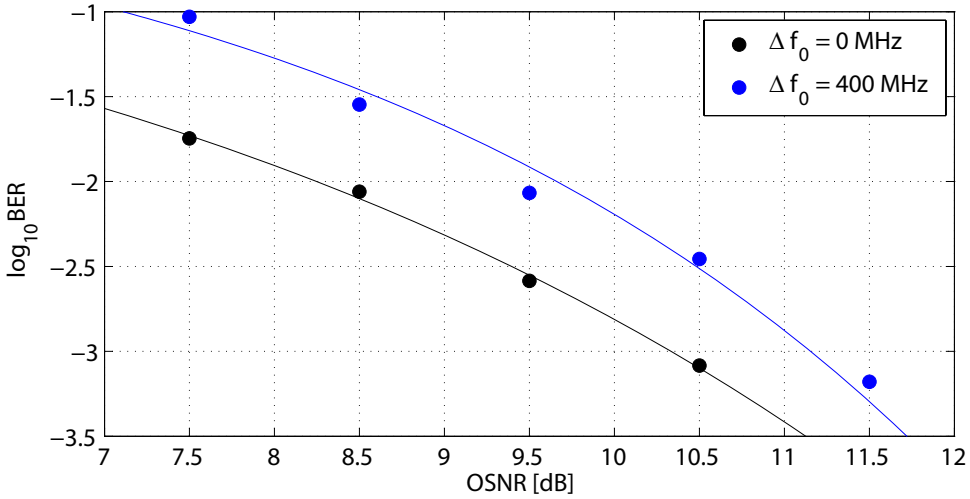

Figure 6.20: BER versus OSNR curver for a 10 GBt/s NRZ-DQPSK-PolMux system with frequency offset estimation. The confront is made between no offset and $\Delta f_0 = 400MHz$.

7

Laboratory Experience

After several month of modeling, we had the great opportunity of testing in the laboratory what we have thoroughly studied in the theory. In this section we are going to present the experiment we have carried out. All the work has been done with Luca Ferrari and with the help of Christophe Peucheret, Michael Galili and Darko Zibar. I want to thank all of them for the help and support they provided us with. It has been a great experience, that allowed us to learn a lot even if we had only few days at our disposal.

Due to time limitation, in this chapter we will report only the final experiment on the OTDM system with coherent detection. However, more time has been spent on measuring both several lasers linewidth and the timing jitter of pulsed sources present in the DTU Fotonik laboratory.

7.1 Experiment Overview

The objective of the experiment was to implement an optical communication system with QPSK modulation at 10 GBt/s and 8 OTDM channels (160 Gbit/s) that exploits a coherent receiver with DSP unit to process the received signal.

In Figure 7.1 an overview of the whole system is presented. A 8 channels OTDM QPSK signal at 160 Gbit/s is generated and sent to a coherent receiver that exploits a pulsed LO at 10 GHz to demultiplex and receive one of the eight channels. The LO is done utilizing a phase modulated CW (PM-CW) pulsed source. The LO is made pulse with the same frequency of the sent signal by means of a clock recovery stage.

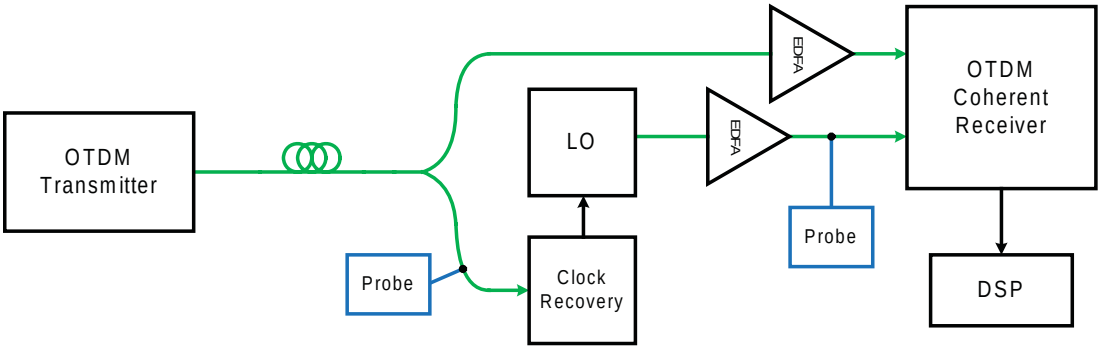

Figure 7.1: Block diagram of the system used in the experiment.

In order, we are going to present the implementation of the four elements: the OTDM transmitter, the pulsed source used as LO, the clock recovery stage, and the coherent receiver for an OTDM signal detection.

To our knowledge, this experiment has been performed only other three times [18], [16], [17], and just two using a separate pulse source as LO [1] [16] [17]. Moreover, this is the first time that the technique of PM-CW pulse source is employed in such an experiment.

As it will be shown later in this section, even if, for lack of time, the error counting at the received signal has not been performed, the experiment can be considered successful.

7.2 Transmitter

Firstly, the transmitter implementation is going to be studied. The final setup used for the experiment is shown in Figure 7.2. The optical signal source used for the OTDM signal is a ML external cavity (ERGO) laser pulsed at 9.953 GHz and emission centered at 1542 nm.

This pulsed source generates pulses with a width of around 2.5 ps (see Figure 7.4(a)). The output signal of the pulsed source is sent to both the external modulator and a path that allows for obtaining an electrical clock at 9.953 GHz used to drive the bit pattern generators. For generating the clock, the signal is first detected by a photodiode (with bandwidth of 12.5 GHz) and then filtered by a narrowband amplifier centered at 10 GHz. The output is an electrical clock at 9.953 GHz.

[1] Generally, the optical source used for the transmitter is also used as LO

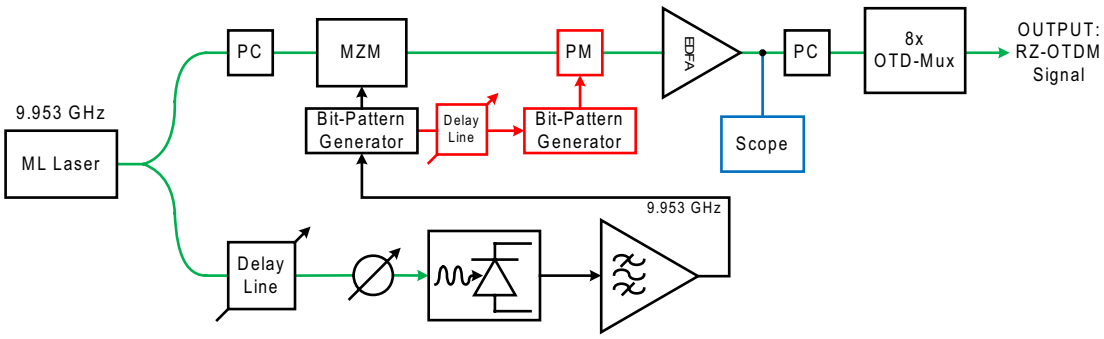

Figure 7.2: Block diagram of the transmitter utilized in the experiment.

The signal passes through a polarization controller (PC) before being modulated. This permits to optimally regulate the polarization. The modulator used is a MZ modulator followed by a phase modulator (PM). This allows both for a QPSK and BPSK modulation (in case the PM is not modulated). However, the performance of this modulator is worse than that of an IQ modulator for a QPSK modulation (see Section 3.1.5), but unfortunately IQ modulators were not available for our experiment.

The bit pattern generators used are two, one for the MZ modulator responsible for the BPSK modulation and another one for the PM used to generate the QPSK signal. The first is driven by the 9.953 GHz clock generated from the non-modulated pulsed optical signal. The second bit pattern generator is fed with an output clock coming from the first bit pattern generator. In between the two we inserted a delay line in order to guarantee that the second stage of modulation (with the PM for obtaining the QPSK signal) is correctly synchronized with the first one. The optimization of the delay and of the bias voltages for both the MZ and PM has been done monitoring the signal through a DD receiver that allows for a direct monitoring of the demodulated QPSK signal.

Both bit pattern generators use a PRBS bit sequence of $2^7 - 1$ bits. The modulation is done directly by the bit pattern generation and there is no encoding stage. Thus, differential encoding is not employed.

The signal, after the modulation is amplified from -12.7 dBm to 13.9 dBm by an Erbium Doped Fiber Amplifier (EDFA) and then multiplexed by the 8-channels OTDM multiplexer shown in Figure 7.3

The OTDM multiplexer allows for the multiplexing of the same signal in 8 different

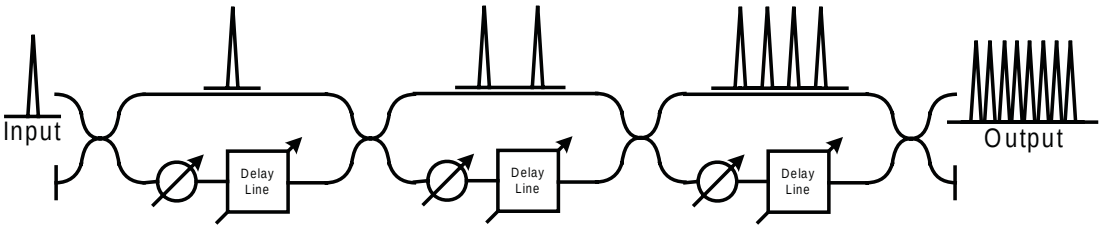

Figure 7.3: Block diagram of the 8-channels OTDM multiplexer.

time channels. The technique utilized by this device is similar to a normal OTDM multiplexer describer in Section 3.1.9, but in this case one signal is multiplexed with itself. The multiplexing operation is done by splitting the signal in two arms, delaying one of the two and then recombining the signal with its delayed version. The result is shown in Figure 7.4. The operation of multiplexing reduces the average power of only 3 dB but the power of one single pulse is reduced of further 8 times since the average power is now distributed over 8 channels.

7.3 Local Oscillator Pulse Source

The pulse source used for the LO is obtained by exploiting the dispersion effect on a sinusoidally phase modulated signal (from now on we will refer to it as PM-CW pulsed source).

The CW laser used for the LO pulse source is an external cavity tunable laser. As it will be explained later the wavelength has been tuned to match with the one of the signal source.

The phase modulation introduces chirp on the CW signal that is afterwards sent through a dispersive fiber (e.g. a standard SMF). The different frequency components of the chirped signal will thus propagate with different velocities altering the intensity of the CW signal. This phenomenon generates pulses with a shape that depends on the accumulated dispersion, on the frequency of the driving sinusoidal signal and on the peak-to-peak voltage applied to the phase modulator (that determines the amount of chirp induced on the CW signal).

As shown in Figure 7.5, in our setup, the CW signal is firstly sent through a MZ modulator driven by the same sinusoidal signal that drives the PM. The MZ modulator

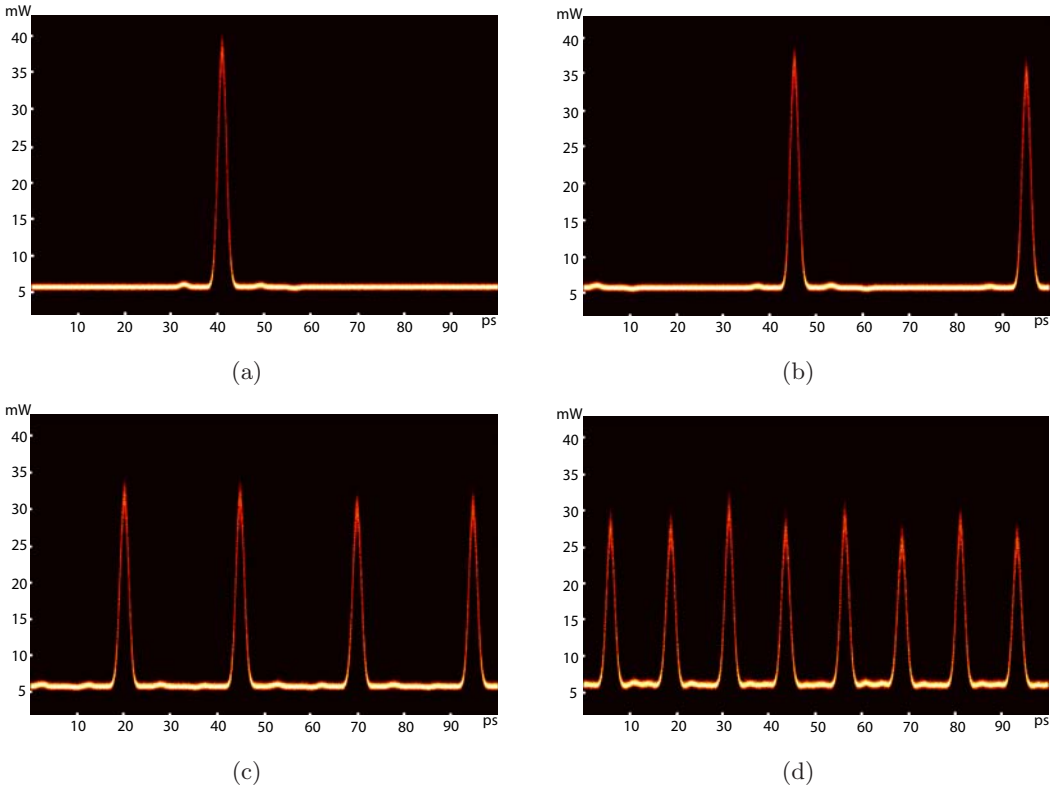

Figure 7.4: RZ signal for a QPSK modulation and (a) no multiplexing, (b) 2x multiplexing, (c) 4x multiplexing, and (d) 8x multiplexing.

is used to improve the extinction ratio of the pulses. Nevertheless, the driving sinusoidal signal must have different amplitude for the PM and the MZ modulator.

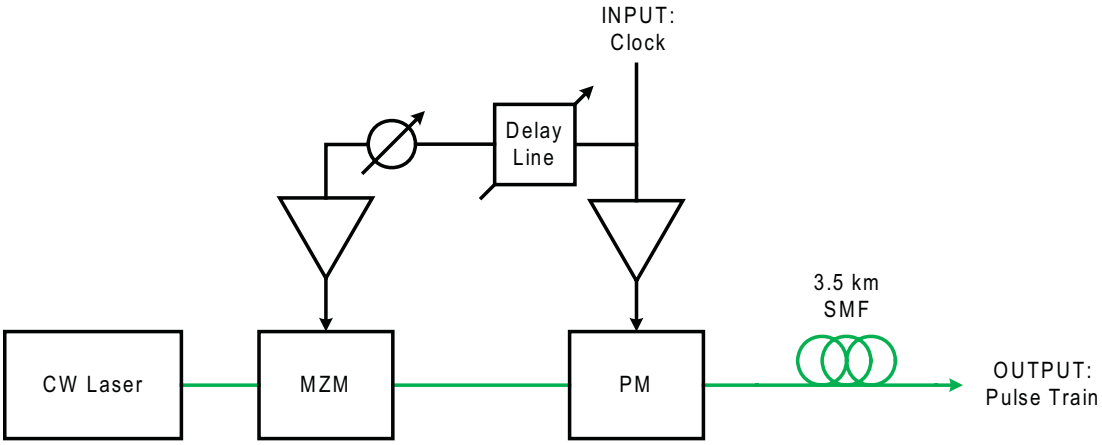

Figure 7.5: Block diagram of the setup used for the PM-CW pulsed source utilized in the experiment.

The ratio between the peak-to-peak voltage and V_π of the PM is called modulation index. In Figure 7.6(a) we can see the dependence of the FWHM of 10 GHz pulses according to the length of standard SMF and the modulation index used in the setup. It is possible to see that the narrowest pulses (i.e. with FWHM of around 5 ps) are obtained with very high modulation indexes (higher than 3.5). For this reason the driving voltage of the PM must be kept very high in order to obtain the best modulation index and consequently increase the effect of dispersion through the fiber.

Thus, the output of the amplifier that provides the driving signal to the PM has been characterized to know the optimal values of peak-to-peak voltages that could have been used to drive the PM. The PM used in the experiment presented a V_π of around 6 V. This means that, in order to obtain the optimal modulation index, the driving signal must be more than 21 V_{pp}. The measured values are shown in Figure 7.6(b). It can be noticed how the amplifier starts saturating when V_{in} is around 800 mV_{pp}. We decided to operate right before the saturation of the amplifier (at 19 dBm) obtaining, at the output of the amplifier, around 16 V_{pp}. This guarantees a modulation index close to 2.6, not in the optimal area but still enough to obtain 10 ps pulses with 3.5 km of standard SMF.

The sinusoidal signal used to drive the PM is also used to drive the MZ modulator

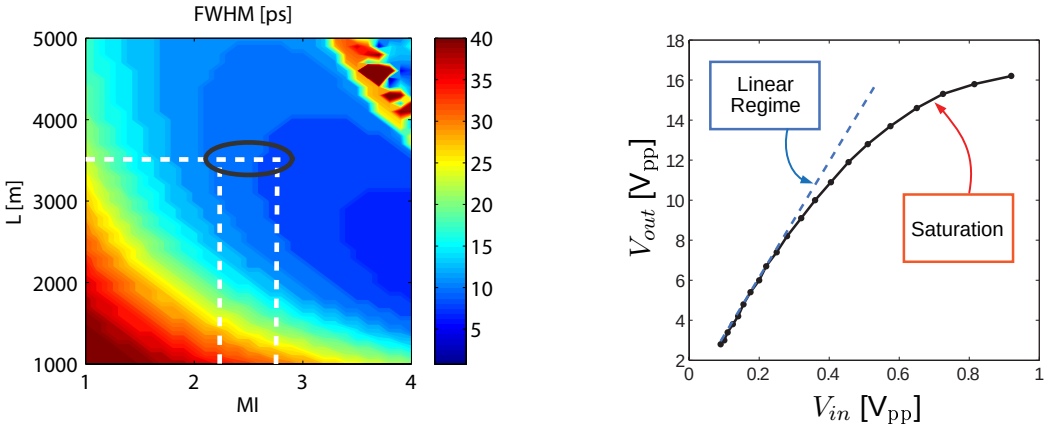

(a) (b)

Figure 7.6: FWHM of the pulses generated with different SMF lengths and modulation indexes (a) and transfer characteristic of the amplifier used to drive the PM for the PM-CW pulsed source.

for the pulse carving, and it must be adjusted to guarantee the optimal modulation. The optimal configuration allowed us to obtain the curving showed in Figure 7.7.

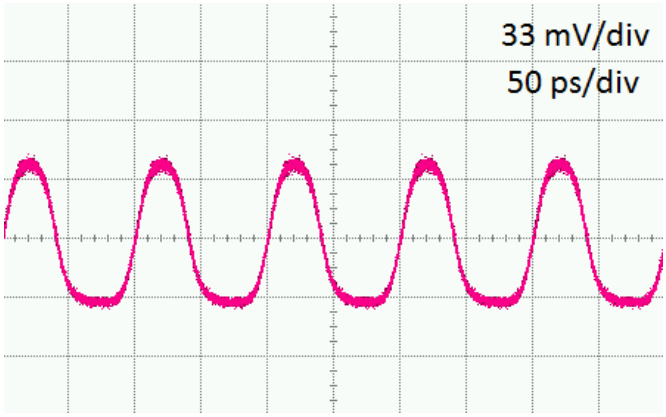

Figure 7.7: Output of the pulse carver.

The last parameter we have to play with is the delay between the signal that drives the MZ modulator and the one that drives the PM. The delay has been varied monitoring the signal until we obtained the best pulsed (see Figure 7.8)

The output of the LO pulse source (shown in Figure 7.9) presents an average power of -17.1 dBm and is thus amplified to 19.3 dBm by and EDFA before being sent to the coherent receiver front end.

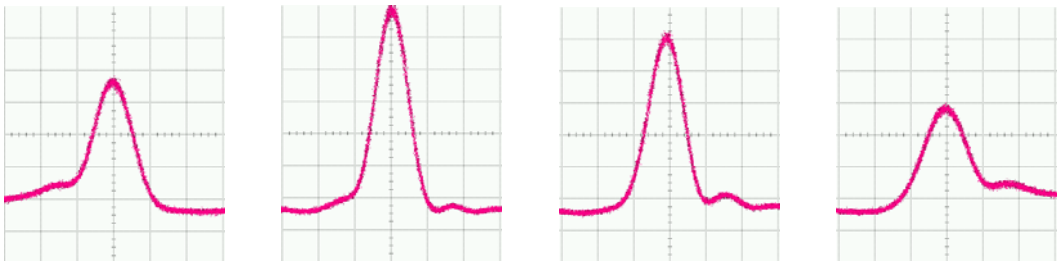

(a) (b) (c) (d)

Figure 7.8: Optimization of the delay between the drive of the MZ modulator and the PM in the PM-CW pulsed source setup.

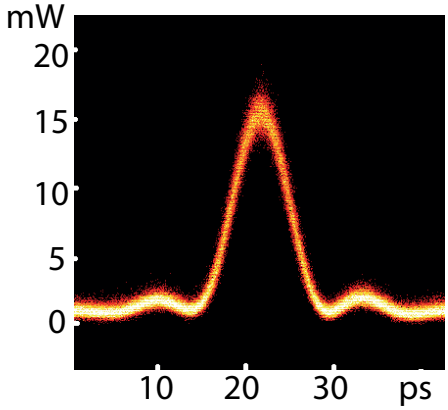

Figure 7.9: Pulse generated with the PM-CW pulsed source.

7.4 Clock Recovery

The clock recovery utilized in our system is an EAM-Based clock recovery. Particularly for the installation and the use of this part of the setup, we were helped by Michael Galili. It is definitely not trivial understanding the way this stage works and in this section we will only try to give a brief overview to the different parts of the clock recovery.

The received optical signal is firstly attenuated and then it is fed into an electro-absorber modulator (EAM). This presents an absorption that is dependent on the applied voltage. The EAM output is received by a photodiode characterized by a bandwidth of around 100 MHz. The photocurrent output of the photodiode is filtered by a low-pass filter with tunable DC driving voltage to extract the offset frequency between the data signal and the VCO driving the EAM. The current output of the photodiode, after the low-pass filtering, represents the error signal between the two clock and it drives the VCO. In fact, The output of the VCO clock and the received signal are mixed into the EAM and if the clock is locked, the output of the photodiode is DC. The low-pass filter presents a tunable DC component that can be used to lock the clock. This VCO output is then multiplied by a factor five and amplified, giving the recovered clock at 10 GHz. Other two stages of multiplication and amplification give other two versions of the recovered clock at 20 and 40 GHz. The 40 GHz clock is attenuated to have a peak-to-peak voltage of around 5 V and is fed into the EAM to close the loop.

The locking of the clock is performed through both a tuning of the DC bias of the low-pass filter of the photocurrent and the attenuation of the optical signal received by the EAM. A spectrum analyzer has been used to monitor the recovered clock. This allowed us to have a mean for understanding when the clocks were locked.

7.5 Coherent Receiver

The reception of the modulated signal is done by means of a coherent receiver. As it can be seen in Figure 7.11 the RZ-OTDM signal and the pulsed LO are both fed into a 90° optical hybrid. The LO is delayed through a variable optical delay line. This is done to be able to make the signal pulses of one of the channels and the LO ones overlap and thus correctly demultiplex that channel (see Section 5.4.1).

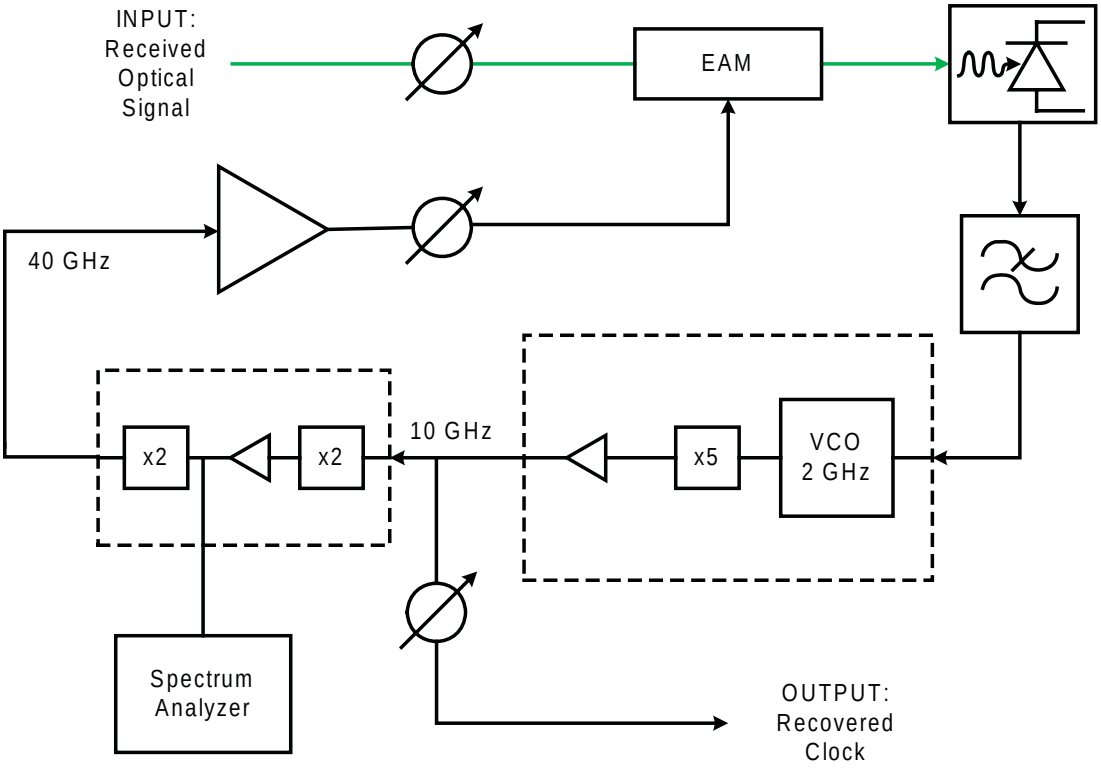

Figure 7.10: Block diagram of the EAM based clock recovery.

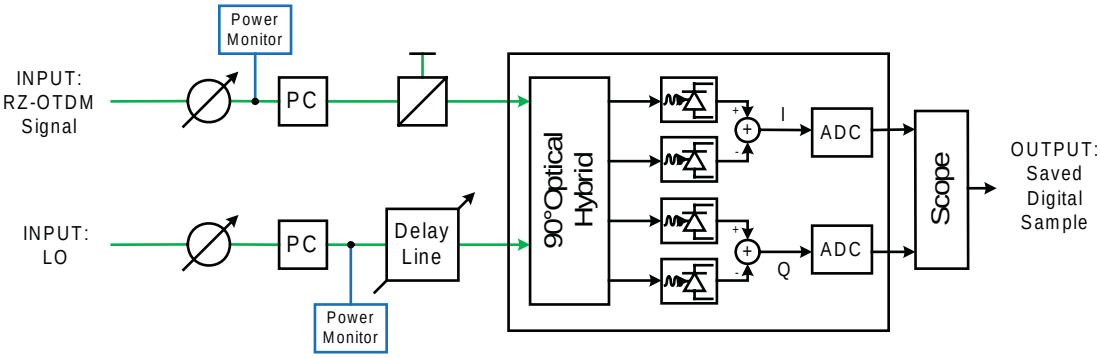

Figure 7.11: Block diagram of the coherent receiver used in the experiment.

Both signal and LO pass through a polarization controller and the signal is fed into a polarization beam splitter to select only one of the two polarizations. The polarization control is used in order to make sure that the signal and the local oscillator have the same polarization when they are made beat together in the 90° optical hybrid.

As explained in Section 5.2, the 90° optical hybrid allows for obtaining the in-phase and quadrature component of the beating between the signal and the LO. Before understanding how we can retrieve the signal from this information, let us see how we optimize the coherent receiver front-end to obtain the best reception.

First of all, the optical signal received by the coherent receiver stage is analyzed by an optical spectrum analyzer in order to select the central frequency around which the LO tunable laser must be tuned. In Figure 7.12, the spectrum of both the signal and the LO pulse source is shown. As we can see the signal spectrum is centered around 1542 nm and the tunable laser of the local oscillator has been tuned accordingly in order to be centered at the same frequency of the signal.

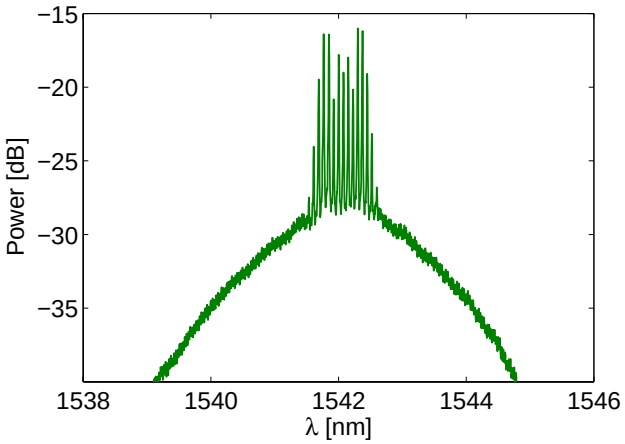

Figure 7.12: Spectrum of signal and LO coupled together in the same fiber.

Then, the beating between the LO and the signal in monitored in frequency in order to finely tune the LO frequency and obtain a good lock with the lowest frequency offset. Third, the optical delay is tuned to obtain a good overlap between the pulses of the local oscillator and those of the signal. Finally, the balance between the input powers of the two optical hybrid inputs are adjusted.

The in-phase and quadrature component are then balanced detected by four photodiodes with 7.5 GHz of bandwidth, and the two photocurrents digitally converted by

two ADCs sampling at 40 GHz (i.e. with an oversampling of a factor 4). The ADCs are not directly clocked with the recovered clock, but the oversampling of a factor 4 is enough to have a one of the four samples very close to the optimal sampling point. Moreover, the low bandwidth of the photodiodes broadens the signal pulses making the penalty given by a suboptimal sampling lower.

The digital signal output of the ADCs is stored and processed offline by the DSP unit. In our experiment we used only the frequency offset estimation and the carrier phase estimation blocks. In the DSP unit the signal is firstly decimated and the optimal of the fours samples is selected. The decimating algorithm confronts the sum of the powers of the four sequences of samples (e.g. the sequence $1, 5, 9, 13, \ldots$, the sequence $2, 6, 10, 14, \ldots$, the sequence $3, 7, 11, 15, \ldots$ and the sequence $4, 8, 12, 16, \ldots$) and keep the one with the highest sum. Then, the decimated signal is processed by the frequency offset estimator and the frequency offset corrected. Finally, the phase of the local oscillator is corrected using a "M-th power block scheme" algorithm (see Section 5.3.3) in the phase estimation block and signal is ready to be demodulated.

7.6 Experiment Results

After having optimized all the setup, we firstly tried to make the system work with a single BPSK channel with the pulsed local oscillator. After a fine tuning of the coherent receiver stage we performed the digital signal processing of the acquired data, but the obtained signal was not encouraging. Several other attempts have been done with a CW LO instead of a pulsed source and this allowed us to correctly demodulate the BPSK signal. After a deeper study of the differences between the two systems we localized the problem in the mismatch between the frequency of the signal (9.953 GHz) and the sampling frequency of the ADCs (40 GHz). The latter is not a multiple of the former and therefore this creates an offset that does not allow for a correct sampling of the signal. Unfortunately, we could not change neither the signal frequency nor the sampling frequency of the ADCs. The solution has been found in a digital processing of the signal in order to move from the 40 GHz sampling to a 39.812 GHz sampling (i.e. a multiple of the signal frequency). This has been done by an interpolation of the original sampled data by a factor $10/(10-9.953) \approx 213$ and a subsequent resampling the interpolated signal every 214 samples. This corresponds to having the signal sampled

at 38.812, a multiple of the signal data rate. This gave use the hoped results and we managed to demodulate the single channel BPSK signal using the pulsed LO. In Figure 7.13, the difference between the sampling at 40 GHz and at 39.812 GHz is shown. The separation between the two points of the BPSK constellation is completely absent in the Figure 7.13(a), but after the digital resampling the signal can be perfectly recovered, as shown in Figure 7.13(b).

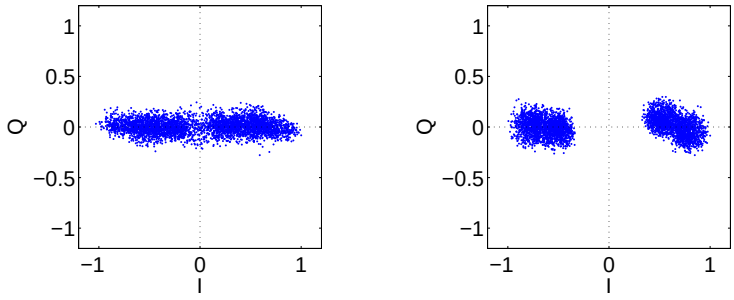

Figure 7.13: BPSK constellation before the use of the interpolation-decimation technique (a) and after (b).

After the demodulation of a single channel BPSK, we tried to use an OTDM signal. Several attempt has been made with both BPSK and QPSK. At last, both a 8 channels OTDM BPSK signal at 80 Gbit/s and a 8 channels OTDM QPSK at 160 Gbit/s have been successfully recovered. The eight channels of the two systems are shown in Figure 7.14 and 7.15. If the BPSK signals shows a very good constellation in all eight channels, the QPSK is more impaired and in channels 3 and 5 the constellations present a very marked spread of the points. Due to lack of time, the error counting at the demodulated signal has not been performed, but from the 4000 symbols recovered and shown in Figure 7.14 and 7.15, the BER can be considered lower than 10^{-3} in most of the channels.

It is interesting to show how the frequency offset estimation allows for a major improvement in the signal recovery, particularly for the QPSK signal. In Figure 7.16 the received signal constellation with and without the use of frequency offset estimation are shown. It is clear how for the QPSK signal the signal recovery was not possible without frequency offset estimation. This is due to the fact that the residual frequency offset

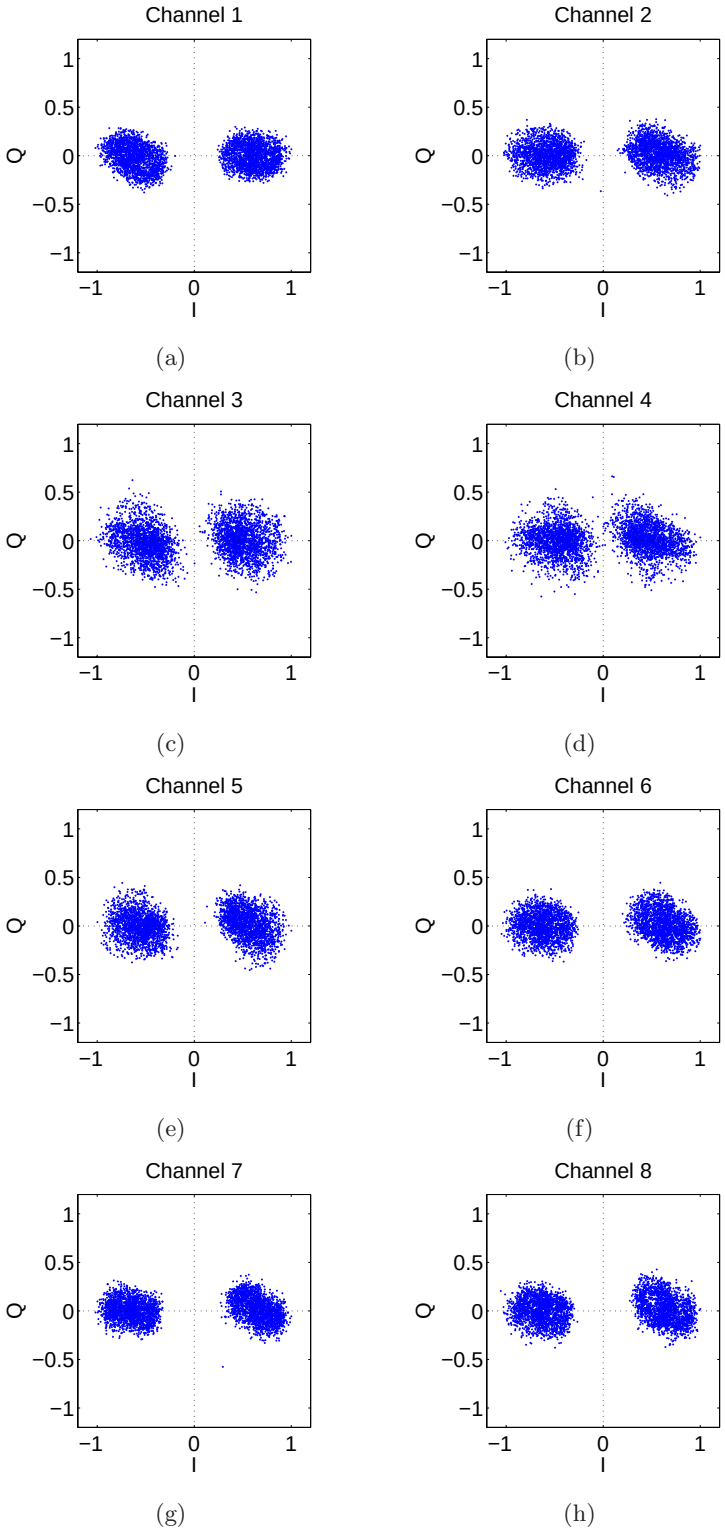

(a) (b) (c) (d) (e) (f) (g) (h)

Figure 7.14: BPSK constellation for the 8 channels of the OTDM system.

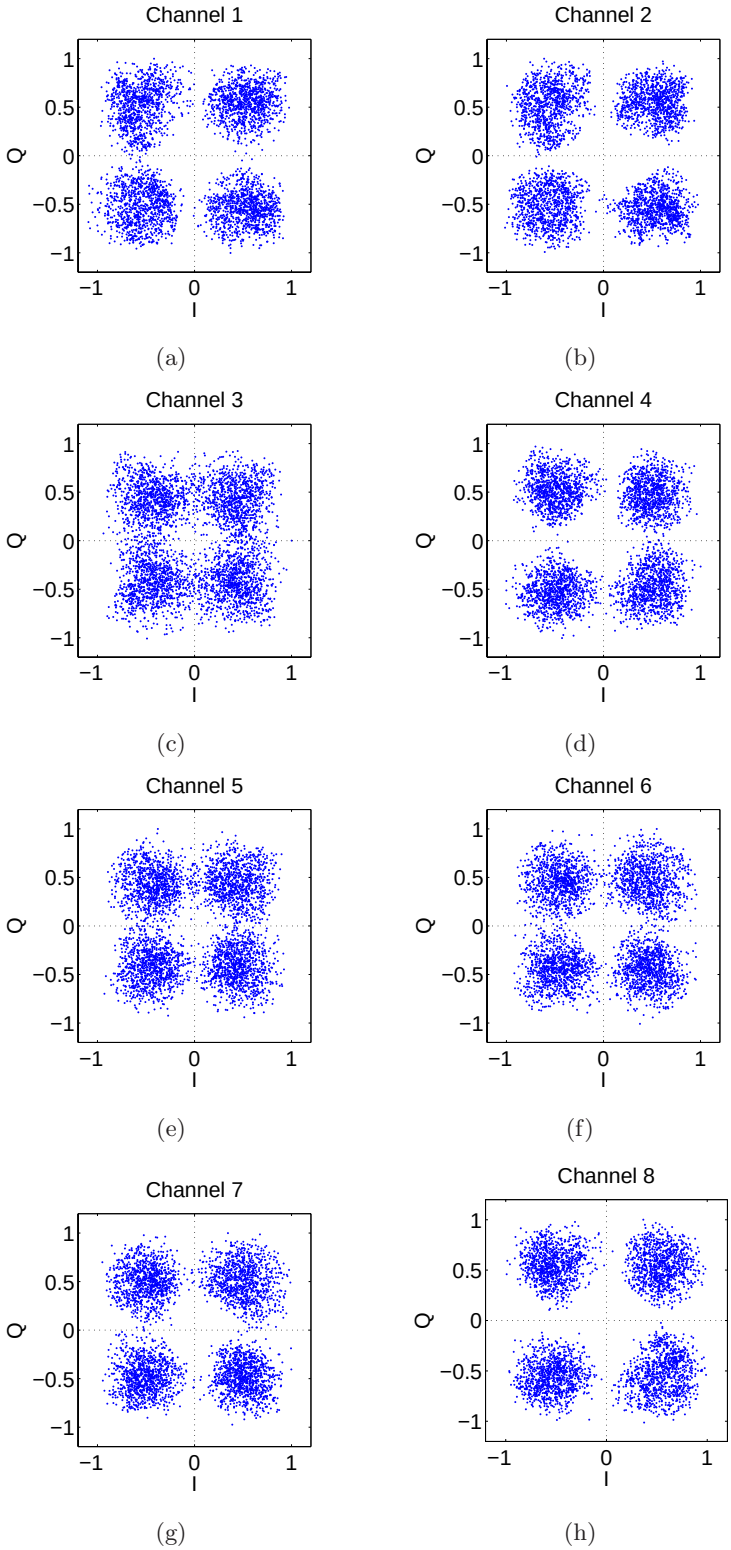

(a) (b) (c) (d) (e) (f) (g) (h)

Figure 7.15: QPSK constellation for the 8 channels of the OTDM system.

after the LO tuning is still several hundreds of MHz (in some simulations we measured 600-700 MHz of offset). This, as the study presented in Section 6.3.4 has underlined, makes a frequency offset estimation almost necessary, especially for a QPSK signal.

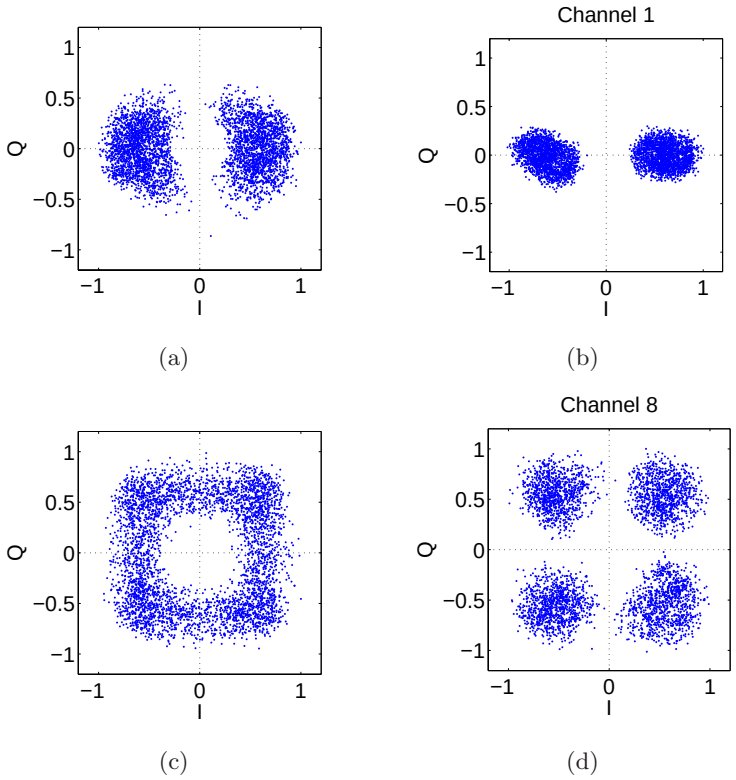

Figure 7.16: BPSK and QPSK constellations with and without frequency offset estimation.

The experiment can be considered successful. However, there are several details that can be improved and would probably allow for an increase in the performance of the system.

First of all, an IQ modulator for the QPSK system would allow for a major improvement in the quality of the QPSK signal, as already explained in Section 3.9.

Second, the LO pulsed source could be refined, using a different phase modulator with lower V_π, thus reducing the modulation index of the PM-CW. This would make us able to obtain pulses with FWHM of around 5 ps. This does not just improve the selection of one of the 8 channels of the OTDM system, but would probably allow to upgrade this to 16 channels.

Moreover, other smaller details could also be fixed. For example, the ASE noise that affects the signal can be reduced regulating the signal power that arrives to the coherent receiver reducing the optical amplification instead of keeping it at the maximum level and attenuating the signal afterwards at the receiver side.

Unfortunately, we had only two weeks to spend in the lab, but it would be really interesting to devolve more time and resources in order to perfect such a system and obtain even better results.

8

Conclusions

The main objective of this thesis was to model and study an optical communication system that employs high order modulations and optical time division multiplexing with coherent detection and digital signal processing.

The numerical model developed in Matlab® for the simulation of optical communication systems has been successfully validated in Section 4, giving a strong basis on the results later found with such a model

In our work, particular attention, was given to the analysis of the DSP algorithms for the processing of the received signal in the digital domain. Throughout the numerical simulations and the laboratory experiment we demonstrated how the digital phase estimation performed with FF algorithms (e.g. the M-th power block implementation of the Viterbi-Viterbi algorithm) allows for very high beat-linewidth. The results are in line with the literature [10] and underline how the digital phase estimation is of very easy implementation and it is much less stringent in the requirement for the linewidth with respect to OPLL. In Square QAM modulations the M-th block scheme algorithm showed much lower performance with respect to the DQPSK.

An extension of the "M-th power block scheme" used for the compensation of the frequency offset between LO and signal laser has been also studied. This showed particularly good results both in the numerical simulations and in the laboratory experiment.

The chromatic dispersion compensation with TDE has also been deeply analyzed. The results obtained by applying this technique show a very good recovery of the signal even if it has been impaired by hundreds of kilometers of fiber transmission. The CD is not the only fiber impairment that can be corrected by means of digital signal

processing. The PMD and polarization rotation can be corrected with an adaptive equalizer. This, has been implemented and tested and show pretty good performance, similar to that found in [9].

Finally, the laboratory experiment allowed us to put hands on what we have been simulating for month. During these two week we tried to transmit a back-to-back 8-Channels OTDM QPSK at 160 Gbit/s with coherent detection and digital signal processing. The success of the experiment did not only underlined the great potential of these techniques, but made us appreciate even more all the time spent on this project.

References

[1] G. P. Agrawal, *Fiber-Optic Communication Systems*. Wiley Series in Microwave and Optical Engineering, John Wiley and Sons, third ed., 2000. viii, 2, 7, 27, 30, 31, 32, 34, 35, 48, 61

[2] E. Forestieri, "Evaluating the error probability in lightwave systems with chromatic dispersion, arbitrary pulse shape and pre- and postdetection filtering," *Journal of Lightwave Technology*, vol. 18, November 2000. viii, 54, 55

[3] J. Wang and J. M. Kahn, "Impact of chromatic and polarization-mode dispersions on dpsk systems using interferometric demodulation and direct detection," *Journal of Lightwave Technology*, vol. 22, February 2004. viii, 49, 56

[4] M. Serbay, *Multilevel Modulation Formats for Optical Communication Systems Based on Direct Detection*. PhD thesis, Christian-Albrechts-Universitat zu Kiel, 2007. viii, 56, 57

[5] Y. Han and G. Li, "Theoretical sensitivity of direct-detection multilevel modulation formats for high spectral efficiency optical communications," *IEEE Journal of Selected Topics in Quantum Electronics*, vol. 12, July-August 2006. 2, 38, 40

[6] K. Kikuchi, "Phase-diversity homodyne detection of multilevel optical modulation with digital carrier phase estimation," *IEEE Journal of Selected Topics in Quantum Electrinics*, July-August 2006. 2, 75

[7] S. Tsukamoto, K. Katoh, and K. Kikuchi, "Coherent demodulation of optical multilevel phase-shift-keying signals using homodyne detection and digital signal processing," *IEEE Photonics Technology Letters*, vol. 18, May 2006. 2, 80

[8] M. Kuschnerov, F. N. Hauske, K. Piyawanno, B. Spinnler, M. S. Alfiad, A. Napoli, and B. Lankl, "Dsp for coherent single-carrier receivers," *Journal of Lightwave Technology*, vol. 27, no. 16, pp. 3614–3622, 15 August 2009. 2, 69, 73

[9] S. J. Savory, "Digital filters for coherent optical receivers," *Optics Express*, vol. 15, no. 2, pp. 804–817, 2008. 2, 70, 71, 73, 108, 136

[10] M. Seimetz, *High-Order Modulation for Optical Fiber Transmission - Transmitters, Receivers, System Performance*. Springer Series in Optical Sciences 143, John Wiley and Sons, 2009. 2, 15, 16, 27, 30, 32, 44, 49, 53, 63, 75, 76, 88, 100, 135

[11] P. J. Winzer, A. H. Gnauck, C. R. Doerr, M. Magarini, and L. L. Buhl, "Spectrally efficient long-haul optical networking using 112-gb/s polarization-multiplexed 16-qam," *Journal of Lightwave Technology*, vol. 28, February 2010. 2, 75, 101

[12] X. Zhou, J. Yu, M.-F. Huang, Y. Shao, T. Wang, P. Magill, M. Cvijetic, L. Nelson, M. Birk, G. Zhang, S. Ten, H. B. Matthew, and S. K. Mishra, "Transmission of 32-tb/s capacity over 580 km using rz-shaped pdm-8qam modulation format and cascaded multimodulus blind equalization algorithm," *Journal of Lightwave Technology*, vol. 28, February 2010. 2

[13] M. Seimetz, "Performance of coherent optical square-16-qam-systems based on iq-transmitters and homodyne receivers with digital phase estimation," *Journal of Lightwave Technology*, vol. 24, September 2006. 2

[14] E. M. Ip and J. M. Kahn, "Fiber impairment compensation using coherent detection and digital signal processing," *Journal of Lightwave Technology*, vol. 28, no. 4, pp. 502–519. 2, 71

[15] K. Kikuchi, "Polarization-demultiplexing algorithm in the digital coherent receiver," *IEEE/LEOS Summer Topical Meetings*, 21-23 July 2008. 2, 73, 74

[16] C. Schmidt-Langhorst, R. Ludwig, L. Molle, D.-D. Groß, R. Freund, and C. Schubert, "Terabit/s single-carrier transmission systems based on coherent time-division demultiplexing," in *OSA/OFC/NFOEC*, 2010. 3, 118

[17] J. K. Fischer, R. Ludwig, L. Molle, C. Schmidt-Langhorst, A. Galperin, T. Richter, C. C. Leonhardt, A. Matiss, and C. Schubert in *High-Speed Digital Coherent Receiver with Parallel Optical Sampling*, 2010. 3, 118

[18] C. Zhang, Y. Mori, M. Usui, K. Igarashi, K. Katoh, and K. Kikuchi, "Straight-line 1,073-km transmission of 640-gbit/s dual-polarization qpsk signals on a single carrier," in *35th European Conference on Optical Communication*, 2009. 3, 118

[19] R. J. Essiambre, G. Kramer, G. J. Foschini, and P. J. Winzer, "High spectral efficiency modulation for high capacity transmission," in *Digest of the IEEE/LEOS Summer Topical Meetings*, pp. 113–114, 2008. 8

[20] T. Mizuochi, "Recent progress in forward error correction and its interplay with transmission impairments," *IEEE Journal of Selected Topics in Quantum Electronics*, vol. 12, July/August 2006. 8

[21] J. T. Verdeyen, *Laser Electronics.* Prentice Hall, third ed., 1995. 14

[22] L. Ferrari, "Ultra-high speed signal generation combining otdm and high-order modulation," Master's thesis, Danmarks Tekniske Universitet, August 2010. 17, 28, 30, 47, 103

[23] N. Kikuchi, "Intersymbol interference suppression technique for optical binary and multilevel signal generation," *Journal of Lightwave Technology*, vol. 25, no. 8, pp. 2060–2068. 21

[24] T. Tokle, *Optimized Dispersion Management and Modulation Formats for High Speed Optical Communication Systems*. PhD thesis, Danmarks Tekniske Universitet, September 2004. 24, 88

[25] M. H. Frosz, *Experimental Investigations of Gigabit Electronic Switching Circuits*. PhD thesis, Danmarks Tekniske Universitet, August 1978. 44

[26] van Wangenheim, *Aktive Filter in RC- and SC- Technik*. Huthig Buch Verlag Heidelberg, 1991. 50

[27] L. G. Kazovsky, G. Kalogerakis, and W.-T. Shaw, "Homodyne phase-shift-keying systems: Past challenges and future opportunities," *IEEE Journal of Lightwave Technology*, vol. 24, December 2006. 62

[28] Y. Painchaud, M. Poulin, M. Morin, and M. Tetu, "Performance of balanced detection in a coherent receiver," *Optics Express*, vol. 17, March 2009. 66

[29] C. Johnson, P. Schniter, T. Endres, J. Behm, D. Brown, and R. Casas, "Blind equalization using the constant modulus criterion: A review," *Proc. IEEE*, vol. 86, 1998. 73

Declaration

I herewith declare that I have produced this paper without the prohibited assistance of third parties and without making use of aids other than those specified; notions taken over directly or indirectly from other sources have been identified as such. This paper has not previously been presented in identical or similar form to any other Danish or foreign examination board.

The thesis work was conducted from August 2009 to July 2010 under the supervision of Christophe Peucheret, Leif Oxenløwe, and Darko Zibar at DTU Fotonik.

Kønenhavn,

Francesco Patarnello